RADIATIVE PASSIVE COOLING FOR CONCENTRATED PHOTOVOLTAICS

A Thesis

Submitted to the Faculty

of

Purdue University

by

Ze Wang

In Partial Fulfillment of the

Requirements for the Degree

of

Master of Science in Electrical Engineering

December 2019

Purdue University

West Lafayette, Indiana

THE PURDUE UNIVERSITY GRADUATE SCHOOL
STATEMENT OF THESIS APPROVAL

Dr. Peter Bermel, Chair

School of Electrical and Computer Engineering

Dr. Peide Ye

School of Electrical and Computer Engineering

Dr. Haiyan Wang

School of Materials Engineering

Approved by:

Dr. Dimitrios Peroulis

Head of the School of Electrical and Computer Engineering

ACKNOWLEDGMENTS

I would like to thank Professor Peter Bermel. As my advisor, he has provided me valuable guidance and support. I look forward to continuing working in his group in the next years. I would also like to thank professor Peide Ye and Haiyan Wang, for giving me insightful suggestions when I first came to Purdue University.

Thank you to Zhiguang Zhou, for his help and advice on my research. The discussions with him has always been very helpful. He also contributed a lot to the design of radiative cooling setup and optical data measuring.

I thank the staff from Birck Nanotechnology Center and Department of Chemistry for the training, assistance and advice they gave me. Especially, I want to thank Jeremiah Shepard, Randy Replogle and Jordan Smith for their help on setup design and fabrication.

Many other generous individuals also helped me with the research and contributed their time. Jie Zhu, Boyi Qian, Hans Torsina and Changkyun Lee assisted me many times for outdoor field test. If without their help, I could not have carried out the experiments by myself.

Finally, thank you to my parents for their support and love. The encouragements from them have always motivated me.

TABLE OF CONTENTS

Page

LIST OF TABLES

Table Page

LIST OF FIGURES

Figure Page

Figure Page

Figure Page

SYMBOLS

V	voltage
V_{OC}	open-circuit voltage
T	temperature
k	boltzmann constant
q	unit charge
C	concentration factor
η	solar cell efficiency
I_{SC}	short-circuit current
I_0	reverse saturation current
I_{BB}	spectral radiance of the blackbody emitter
h	Planck's constant
ν	frequency of light
c	speed of light
E_{BB}	spectral exitance of blackbody
P_{BB}	radiant exitance of blackbody
P_{cool}	net cooling power
P_{sky}	absorbed sky irradiance flux
P_{sun}	absorbed solar irradiance flux
$P_{cond+conv}$	convection and conduction heat transfer
P_s	surface absorbed irradiance
P_{sensor}	sensor measured irradiance
σ	Stefan–Boltzmann constant
ε	emissivity
α	absorptance

Φ	spectral irradiance flux
Ω	solid angle
θ	angle
A_s	surface area
I_{sun}	solar spectrum
$I_{AM1.5}$	AM1.5 solar spectrum
F_s	view factor to sky
F_g	view factor to ground
τ_{lens}	Fresnel lens transmittance
τ_{LDPE}	LDPE film transmittance
$\bar{\tau}_{LDPE}$	effective LDPE film transmittance
τ_{tot}	total transmittance of the light path
ρ_{albedo}	surface albedo
ρ_{mirror}	Al mirror reflectance
ρ_{tot}	total reflectance of the light path
α	angle of incident sunlgiht
DNI	direct normal solar irradiance
DHI	diffused horizontal solar irradiance
T_{sky}	effective sky temperature for surfaces outside the chamber
$T_{sky(LDPE)}$	effective sky temperature for surfaces inside the chamber
ε_{sky}	sky emittance
$\bar{\varepsilon}_{sky}$	averaged sky emittance over hemisphere
ε_{eff}	effective surface emittance
ε_{cooler}	cooler emittance

ABBREVIATIONS

CPV	concentrating photovoltaic
DC	direct current
DHI	diffused horizontal solar irradiance
DNI	direct normal solar irradiance
FTIR	Fourier-transform infrared spectroscopy
IR	infrared
IRENA	International Renewable Energy Agency
ISE	Fraunhofer Institute for Solar Energy System
LCOE	levelized cost of energ
LDPE	Low-density polyethylene
NSRDB	National Solar Radiation Database
PDMS	polydimethylsiloxane
PE	polyethylene
PMMA	acrylic
PV	photovoltaic
TPX	polymethylpentene

ABSTRACT

M.S., Purdue University, December 2019. Radiative Passive Cooling for Concentrated Photovoltaics. Major Professor: Peter Bermel.

Photovoltaic (PV) cells have become an increasingly ubiquitous technology; however, concentrating photovoltaics (CPV), despite their higher theoretical efficiencies and lower costs, have seen much more limited adoption. Recent literature indicates that thermal management is a key challenge in CPV systems. If not addressed, it can negatively impact efficiency and reliability (lifetime). Traditional cooling methods for CPV use heat sinks, forced air convection or liquid cooling, which can induce an extremely large convection area, or parasite electric consumption. In addition, the moving parts in cooling system usually result in a shorter life time and higher expense for maintenance. Therefore, there is a need for an improved cooling technology that enables significant improvement in CPV systems.

As a passive and compact cooling mechanism, radiative cooling utilizes the transparency window of the atmosphere in the long wavelength infrared. It enables direct heat exchange between objects on earth's surface with outer space. Since radiated power is proportional to the difference of the fourth powers of the temperatures of PV and ambient, significantly greater cooling powers can be realized at high temperatures, compared with convection and conduction. These qualities make radiative cooling a promising method for thermal management of CPV. In this work, experiments show that a temperature drop of 36 °C have been achieved by radiative cooling, which results in an increase of 0.8 V for open-circuit voltage of GaSb solar cell. The corresponding simulations also reveal the physics behind radiative cooling and give a thorough analysis of the cooling performance.

1. INTRODUCTION

The rapid growth of power consumption has resulted in power outages and pollution, driving a search for alternative energy sources as substitutes for fossil fuels. Renewable energy, as a group of clean, sustainable and economic energy sources, has significant potential to replace a great deal of current fossil fuel use. Photovoltaics (PV), as one of the most important renewable energy technologies, has shown great potential, developing at a very fast pace during the past ten years. According to the 2018's report from International Renewable Energy Agency (IRENA) [1], 55% of total capacity growth for renewable energy is contributed by PV (see Fig.1.1), with a volume of 94 GW. Not as complicated as other renewable energy, photovoltaics can directly convert solar energy to DC (direct current) at a considerable efficiency, and can be customized to various sizes for different applications with a wide range of freedom. It can be used for grid electric power system or off-grid for individuals. With all the merits, the dominating growth of PV market is inevitable, which further led the price decrease to a point close to traditional fossil fuels. As shown in Fig.1.2, Fraunhofer Institute for Solar Energy Systems (ISE) predicts that the levelized cost of energy (LCOE) for PV in Germany will become one of the cheapest energy in the near future [2], making PV a very competitive energy source.

1.1 Limitation of PV and CPV

As one of the most promising renewable energy, PV has attracted numerous studies. People have shown great interest of improving its performance in order to better utilize solar energy and lower the cost of PV. The easiest way to do this is to improve the efficiency and reliability of PV. Ideally, the ultimate efficiency for a heat engine at room temperature (300K) to convert solar energy into useful work is followed by

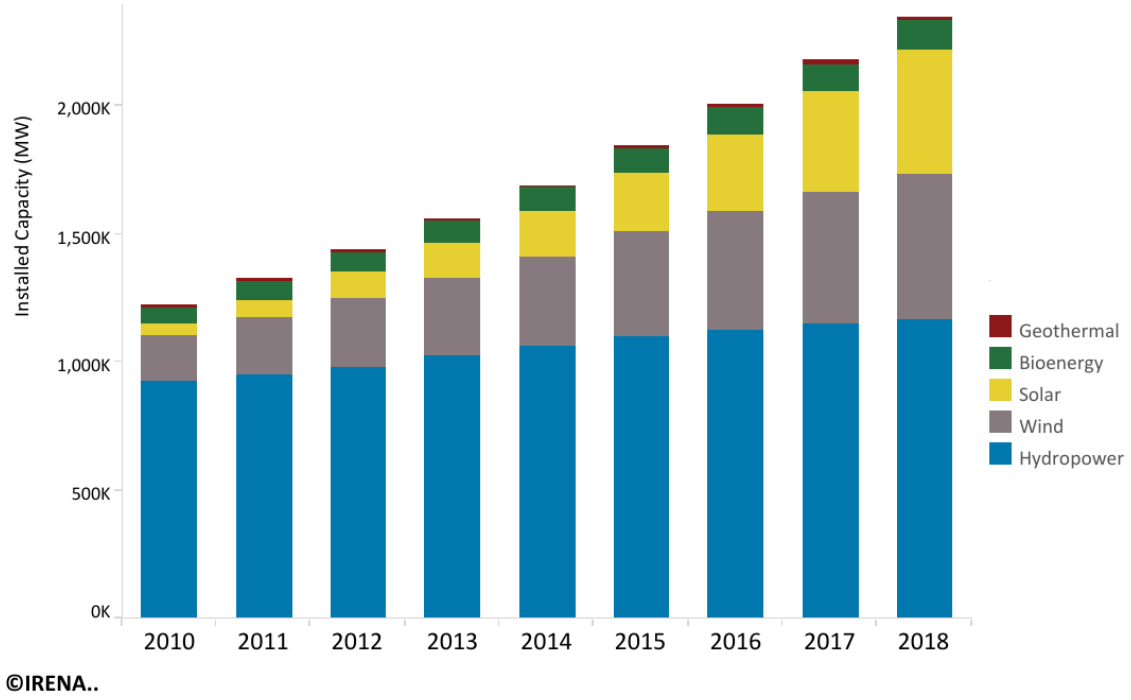

Fig. 1.1. Global renewable energy capacity trend [1]. The total power from renewable energy increases at a fast speed each year. Picture is generated with IRENA's online tool.

Landsberg's efficiency [3], which is around 93%. However, the maximum efficiency for a single-junction solar cell under one sun (unconcentrated sunlight) is predicted only to be 31% at 1.1 eV [4], whereas the reported highest efficiency for fabricated solar cell is around 27% ,achieved by crystalline silicon solar cell [5, 6]. Most of the energy loss in single-junction solar cell is caused by PV bandgap and solar spectrum mismatch, namely, the photons with energy lower than PV bandgap do not have enough energy to excite electron-hole pairs, thus cannot be absorbed; while the photons with energy higher than bandgap can be absorbed, but the generated electrons and holes will thermalize back to the bottom of conduction band and top of valence band, respectively, releasing the energy as waste heat. To solve this problem, multi-junction solar cells were proposed. By stacking up multiple materials together with different bandgaps, photons from solar radiation can be absorbed much more efficiently. The theoreti-

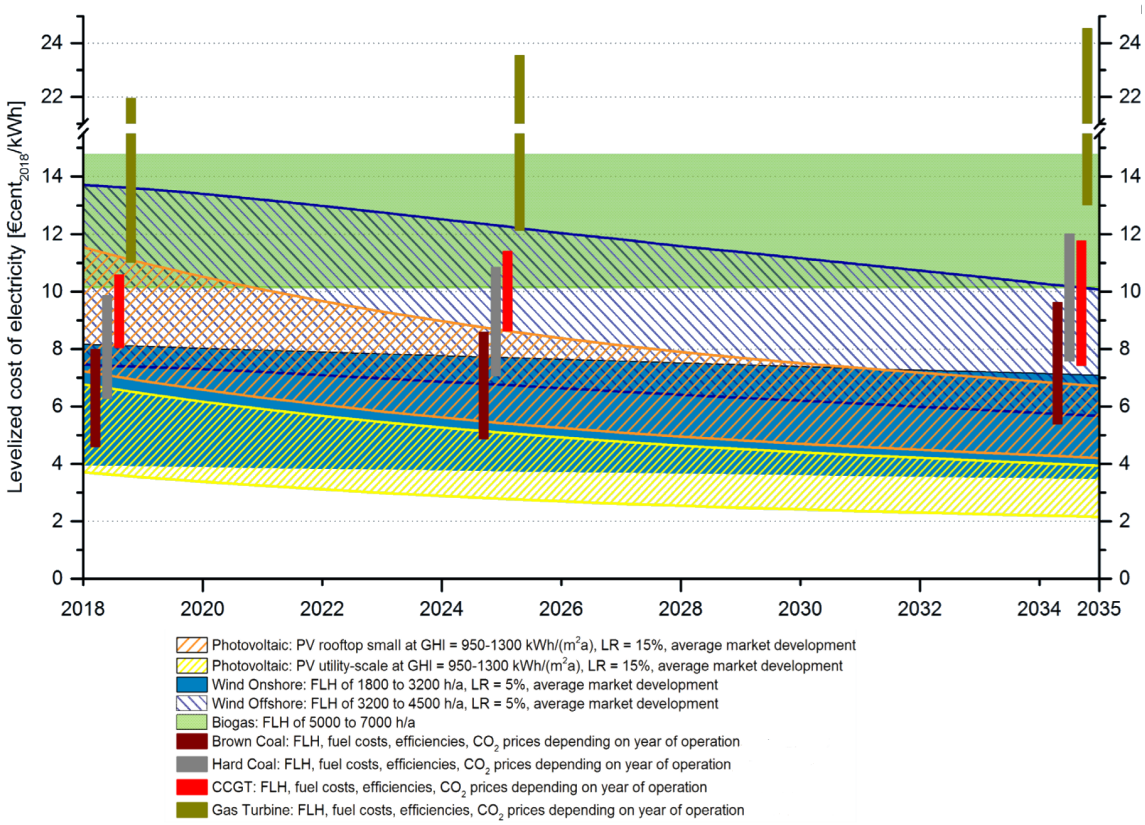

Fig. 1.2. Prediction for the levelized cost of energy in Germany from today through 2035. Picture is reprinted and modified based on ISE's report [2].

cal highest efficiency for multi-junction solar cell under one sun is around 68% with infinite junctions [7]. In real case, the reported efficiency record for multi-junction cell under one sun is around 39%, with 6 junctions accomplished by advanced III-V multijunction techniques [5, 6].

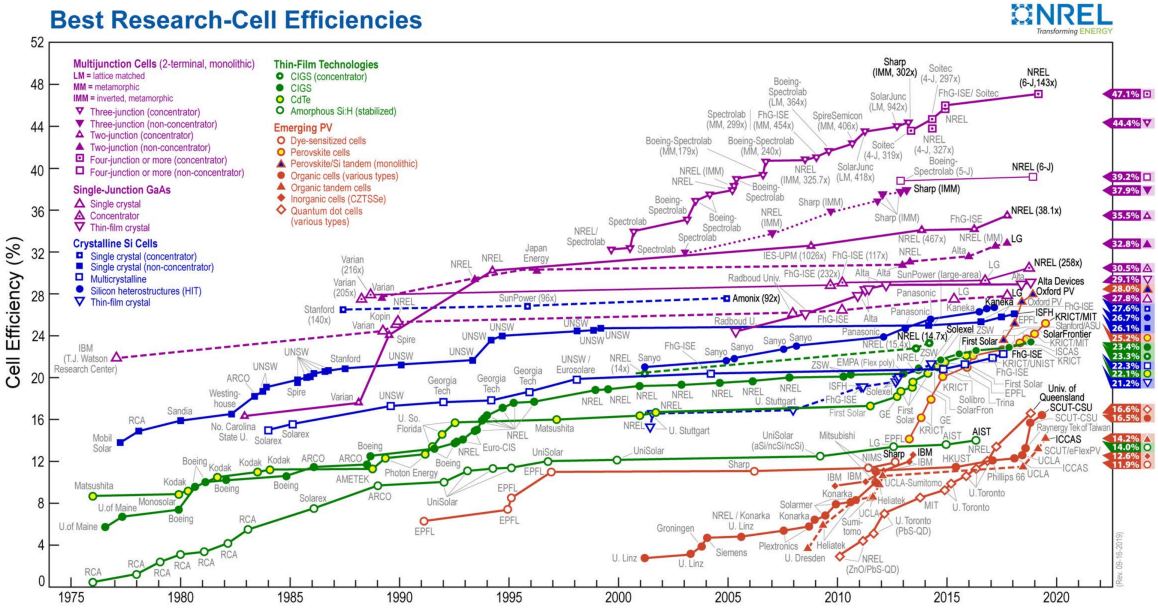

Fig. 1.3. Highest reported efficiencies for solar cells over the last several decades. Picture is reprinted from National Renewable Energy Laboratory (NREL) [6].

To further improve the energy converting efficiency, concentrating photovoltaics (CPV) were developed and has become one of the most efficient PV systems. In a CPV system, concentrators, such as mirrors and Fresnel lenses are used to increase the solar illumination. Since the short-circuit current increases linearly with incident light intensity, concentrator can provide solar cells a much larger current output. As a result, the open-circuit voltage increases logarithmically with short-circuit current [8–10] following Eq. 1.1

$$V'_{OC} = V_{OC} + \frac{kT}{q} \ln(C)\,, \tag{1.1}$$

where V'_{OC} is the open-circuit voltage of the solar cell under concentration, V_{OC} is the open-circuit voltage at one sun, k is the Boltzmann constant, T is operating temperature, q is unit charge, C is concentration ratio. This further gives the efficiency of CPV as Eq.1.2

$$\eta' = \eta \left(1 + \frac{kT}{q} \frac{\ln C}{V_{OC}}\right) \tag{1.2}$$

where η' and η are the efficiency of CPV and PV, respectively.

For a 10× solar concentration factor, the open-circuit voltage of Si solar cell can increase by 0.06 V, the improvement of efficiency can also be derived from Eq.1.2, depending on the different types of solar cells. The theoretical efficiency limit for concentrated multijunction PV also jumps up, from previously introduced 68% for one sun to 86% for 45,900 suns [7]. A summary of highest solar cell efficiency records is shown in Fig.1.3. It is clear that CPV with multi-junction solar cells dominates the highest efficiency solar cells.

The benefits brought by concentrators are not only limited to higher efficiency. Due to the employment of concentrators, the active area of solar cell reduces drastically. Only a small piece of solar cell which can cover the focused beam will be enough for a CPV system. This can significantly cut the cost of materials, which usually accounts for the highest portion of the total cost. As a result, more expensive PV, such as multi-junction solar cells, can be used in CPV to further push the limit of performance. The efficiency of the leading edge CPV is nearly doubled compared with flat-plate PVs.

However, CPV systems have several limitations. One significant drawback is that the higher solar power input gives rise to a steep increase of temperature. Studies have shown that higher operating temperature can reduce the efficiency of PV to a large extent [11, 12]. Briefly, increasing temperature creates more carriers inside the solar cell, leads to a higher reverse saturation current I_0, which is strongly dependent with the carrier density. According to Shockley diode equation, as shown in Eq. 1.3, the V_{OC} drops as I_0 increases, while the short-circuit current I_{SC} is not affected by temperature too much. The efficiency is thus degraded by higher temperature. In other words, the higher carrier concentration in PV greatly increases the rate of recombination process, diminishing the collected electrons on both sides of the cell, the open-circuit voltage is decreased consequently.

$$V_{OC} = \frac{kT}{q} \ln\left(\frac{I_{SC}}{I_0} + 1\right) \tag{1.3}$$

Moreover, the heat dissipation caused by resistance in CPV systems goes up quadratically with increased I_{SC}, this will in turn generate more heat, reducing the efficiency. Furthermore, the reliability of PV deteriorates at higher temperatures. Many failure modes are directly related with temperature; therefore, without a good thermal management approach, CPV systems can degrade very quickly [13–15]. Depending on the design, material, and fabrication quality, the rate can vary to some degree. For CPV, a recent research has shown that at a 820× concentration factor, the lifetime of the multi-junction cell working under 100 °C can shrink to 1/17 of which works at 80 °C [15]. The extreme reduction of lifetime and efficiency makes thermal management for CPV a necessity.

1.2 Basic principles of radiative cooling

Thermal management is an important factor to consider when designing a system which may generate excess heat. Not limited to PV systems, cooler operation environment can usually improve reliability and efficiency of any system. There are three ways of transferring heat from an object to another, namely, conduction, convection and radiation [16]. Most of the cooling mechanisms are based on at least one of the three ways, while some others are combined. The most common methodologies for thermal management are heat sinks, convective or forced air cooling, liquid cooling, heat pipes, etc. [17–20], which only utilizes conduction and convection. This is partly because heat transfer by radiation is limited for most of the indoor applications, as the ambient environment is usually not low enough to fully exploit its potential. However, for outdoor applications such as PV or CPV, radiative cooling can be an excellent method to dump waste heat, due to the open access to clear sky.

Radiative cooling is a cooling mechanism using thermal radiation to dissipate heat. Any object in our universe with a temperature above 0K radiates electromagnet

waves to ambient and releases internal energy, as a result of the thermal motion of particles in matter, such as charge acceleration or dipole oscillation [21]. Thermal radiation is not only a fundamental way to transfer heat, but also a very unique one. It does not need any medium to transfer energy as conduction and convection, which makes it the only way to exchange heat for objects in free space like stars, planets or spacecraft. This property allows us to calculate the effective temperature of the universe. From a thermodynamic perspective, the universe behaves like a blackbody with a temperature around 3 K [22]. This extremely low temperature makes it the ultimate heat sink for any systems having direct access to outer space.

The nature of radiative cooling brings several special advantages compared with other cooling methods. First, the heat dissipating rate through radiation is proportional to the fourth power of the temperature difference of the two objects, namely, $T_1^4 - T_2^4$, where T_1 and T_2 are the surface temperatures of the two objects [16]. In the contrary, for conduction and convection, the heat transfer rate is only a function of $T_1 - T_2$. Obviously, radiation can significantly contribute to the total cooling power for a system, especially when under a high temperature. Plus, radiation only happens at surfaces, thereby it does not need any bulky heat sinks or moving parts as air or liquid cooling and can thus improve compactness and reliability of the cooling system. More importantly, unlike forced air or liquid cooling, no extra energy consumption is needed to power a radiative cooler [20]. The simple, compact and passive nature of radiative cooling makes it an outstanding cooling mechanism for CPV.

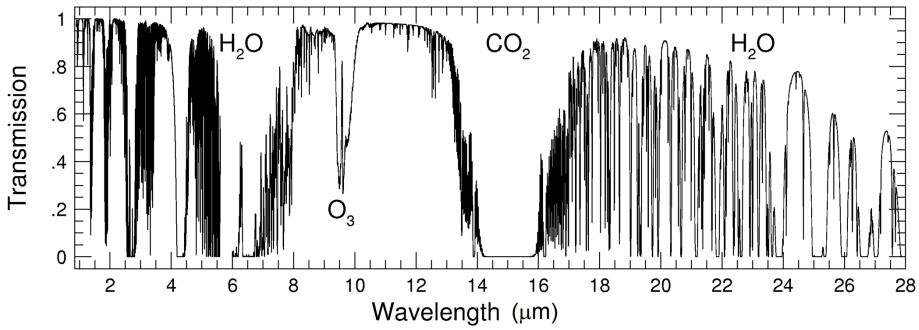

Fig. 1.4. Atmospheric transmittance for near infrared. The transparency window occurs from 8 μm to 13 μm. The atmosphere absorption caused by water vapor, ozone and carbon dioxide are also noted in the figure.

To understand outdoor radiative cooling, the optical property of atmosphere must be studied. The earth's atmosphere is consist of several different gases, mostly are N_2, O_2, CO_2 and water vapor. Each of them has a wavelength dependent absorption rate, which makes atmosphere mostly opaque but transparent at certain windows. The radiative cooling is enabled by the existence of atmosphere transparency window from 8 to 13 μm [23], as shown in Fig.1.4. On the surface of earth, electromagnetic waves with wavelength in this range can go through the atmosphere and exchange heat directly with outer space. For an object with ambient temperature around 300 K, the wavelength of peak thermal radiation coincides with the transparency window, as seen in Fig.1.5, giving a possibility to dump waste at a considerable rate. From another point of view, radiative cooling is caused by the imbalanced incoming and outgoing thermal radiation power flux. As the result of transparency window, the emitted thermal radiation from the atmosphere is low. For a terrestrial object at ambient temperature with high emissivity from 8 to 13 μm, the emitted radiation always exceeds the absorbed radiation from the atmosphere. If heat transfer mechanisms such as the radiation from sunlight less parasitic losses such as conduction and convection are not considered, the incoming energy will not make up for the outgoing energy, leading the temperature to drop below ambient.

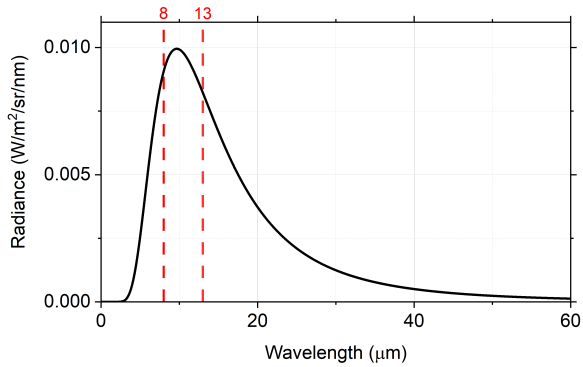

Fig. 1.5. Blackbody radiation of a surface at 300 K. The peak power density is around 8 to 13 μm. This allows radiative cooling transfer heat to outer space at a large rate.

The radiation profile of a blackbody emitter follows Planck's law, which is shown in Eq.1.4.

$$I_{BB}(\nu, T) = \frac{2h\nu^3}{c^2} \frac{1}{e^{\frac{h\nu}{kT}} - 1} \tag{1.4}$$

where $I_{BB}(\nu, T)$, with unit of $[W \cdot m^{-2} \cdot HZ^{-1}]$, is the spectral radiance of the blackbody emitter; h, ν, c, k and T are Planck's constant, frequency of light, speed of light, Boltzmann constant, and the surface temperature, respectively. The plot shown in Fig.1.5 previously is an example of spectral radiance of a blackbody at 300 K. Integrating Eq.1.4 over 2π solid angle will give the E_{BB} spectral emittance as shown in Eq.1.5 , with unit of $[W \cdot m^{-2} \cdot HZ^{-1}]$.

$$\begin{aligned} E_{BB}(\nu, T) &= \int_0^{2\pi} d\Omega \cdot \cos\theta \cdot I_{BB}(\nu, T) \\ &= I_{BB}(\nu, T) \int_0^{2\pi} d\varphi \int_0^{\frac{\pi}{2}} d\theta \cdot \sin\theta \cdot \cos\theta \\ &= \pi I_{BB}(\nu, T) = \frac{2\pi h\nu^3}{c^2} \frac{1}{e^{\frac{h\nu}{kT}} - 1} \end{aligned} \tag{1.5}$$

It can be seen from Eq.1.5 that by multiplying a factor of π to spectral radiance $[W \cdot m^{-2} \cdot HZ^{-1}]$, one can derive the spectral exitance $[W \cdot m^{-2} \cdot HZ^{-1}]$ as the hemisphere radiation from the emitter. In order to calculate the total emitted power, the

spectral exitance has to be integrated over the whole frequency, which is given by Stefan–Boltzmann law as shown in Eq.1.6.

$$P_{BB}(T) = \int_0^\infty E_{BB}(\nu, T)\, d\nu = \frac{2\pi^5}{15}\frac{k^4 T^4}{c^2 h^3} = \sigma T^4 \tag{1.6}$$

where $P_{BB}(T)$ is the total radiance per unit area of the blackbody, with unit of $[W \cdot m^{-2}]$, $\sigma = \frac{2\pi^5}{15}\frac{k^4}{c^2h^3} = 5.67037 \times 10^{-8}$ $[W \cdot m^{-2} \cdot K^{-4}]$, is the Stefan–Boltzmann constant.

Like above-mentioned, the emitted power by thermal radiation increases to the fourth power of the surface temperature, making radiative cooling a very competitive thermal management for high temperature systems such as CPV.

For non-blackbody surfaces, the radiation is reduced depending on the material and structure of the emitters. Emissivity is defined in such case to describe the ability of the emitter to radiate electromagnetic waves, it tells the effectiveness of a surface in emitting thermal radiation as comparing to a blackbody at the same temperature. The definition of emissivity $\varepsilon(\nu, T)$ is given by Eq.1.7.

$$\varepsilon(\nu, T) = \frac{E(\nu, T)}{E_{BB}(\nu, T)} \tag{1.7}$$

where $E(\nu, T)$ is the emitted spectral exitance from the surface at temperature T , $E_{BB}(\nu, T)$ is the spectral exitance of a blackbody at the same temperature. Usually, the emissivity for any material always varies from 0 to 1.

Similarly, the absorptance, $\alpha(\nu, T)$, of a material is defined as the effectiveness of a surface in absorbing radiation as comparing to a blackbody at the same temperature, as shown by Eq.1.8

$$\alpha(\nu, T) = \frac{\Phi_a(\nu, T)}{\Phi_r(\nu, T)} \tag{1.8}$$

where $\Phi_a(\nu, T)$ is the spectral irradiance flux absorbed by the surface, $\Phi_r(\nu, T)$ is the spectral irradiance flux received by the surface.

According to Kirchhoff's law, at local thermal equilibrium, the spectral-directional emissivity of the structure equals its spectral-directional absorptance [24], which leads

to $\varepsilon(\nu, T) = \alpha(\nu, T)$. In other words, for a material at thermal equilibrium, whatever it absorbs will be emitted back to the environment. Thus, the absorptivity and emissivity are essentially the same thing. This means that, if a body is a good absorber of radiation at a particular wavelength, it will also be a good emitter of this wavelength. The terms absorber and emitter are therefore equivalent.

It should be noted that the above equations can also be written in the form of frequency dependent, wavenumber dependent, angular frequency dependent, etc. Depending on the discussion of different subjects, usually a best suitable form is used for simplicity.

As the stronger emission also indicates a stronger absorption, the emissivity profile of radiative cooler needs to be carefully designed and optimized to fit different applications. Generally speaking, the emitters for radiative cooling can usually be classified as below and above ambient cooling, or nighttime and daytime cooling. For below ambient cooling, the cooler should have a unity emissivity in the transparency window and zero elsewhere. An object with selective emissivity like this is called selective emitter. In this way, the thermal radiation can be strictly restricted in 8 to 13 μm, in order to achieve a very low steady-state temperature in both day and night. However, due to the limited radiation spectrum range, below ambient cooler does not give a very large radiation power. The above-ambient cooler can provide a better performance in this case. Above ambient radiative cooling requires the emitter to have a strong emittance in the entire wavelength range to maximize the thermal radiation, which means the emissivity of the emitter appears like an ideal blackbody. This is true for nighttime above-ambient radiative cooling, however, if the emitter is used during the day under sunlight, the emitted thermal radiation is not comparable to the absorbed solar irradiance, resulting a temperature even higher than other surfaces. Hence, for daytime above-ambient cooling, the ideal cooler should have a zero absorption in solar spectrum to eliminate the heating from sun, but a unity emittance elsewhere to yield a high outgoing power. A summary of ideal emissivity for different types of radiative cooling is shown in Tab.1.1 and Fig.1.6 .Previous works have shown

that if the emissivity is well engineered to restrict radiation within transparency window and the object is insulated with ambient to eliminate parasitic heat transfer, the experimentally demonstrated temperature decreasing can be greater than 40 K below ambient [25]. Meanwhile, for an ideal emitter for below-ambient cooling, which has a unity emissivity within transparency window and zero elsewhere, the predicted temperature drop can be as great as 60 to 100 K below ambient depending on the atmosphere conditions and ambient temperature, theoretically [25–28].

Table 1.1. Ideal emissivity profile for different types of radiative cooler, numbers indicate the emissivity in the corresponding spectrum range. Solar spectrum: $0 \sim 4$ μm; transparency window: $8 \sim 13$ μm

Type	Solar Spectrum	Transparency Window	Other Range
Below-ambient	0	1	0
Above-ambient, daytime	0	1	1
Above-ambient, nighttime	1	1	1

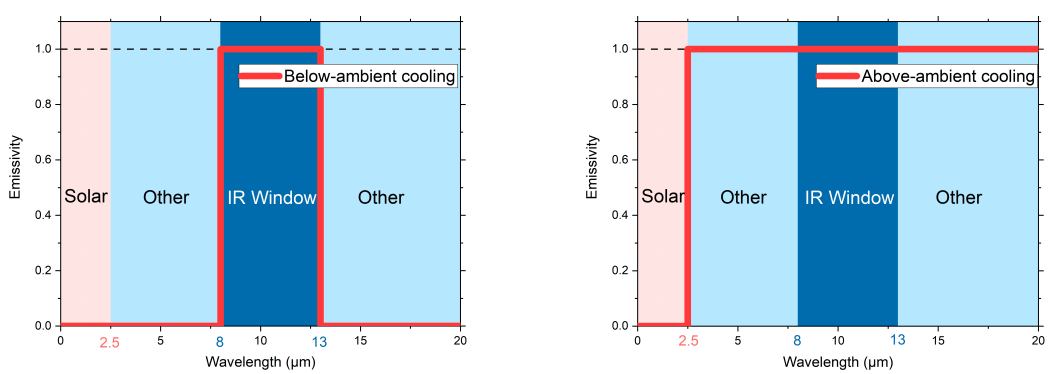

(a) Below-ambient cooler

(b) Above-ambient cooler

Fig. 1.6. Emissivity of ideal above-ambient and below-ambient cooler

The cooling power of a selective emitter is defined as Eq.1.9

$$P_{cool}(T) = P_{rad}(T) - P_{sky}(T_a) - P_{sun} - P_{cond+conv} \tag{1.9}$$

where T is the temperature of the emitter, respectively, $P_{cool}(T)$ is the total net cooling power, $P_{rad}(T)$ is the power of emitted thermal radiation from the emitter, $P_{sky}(T_a)$ is the absorbed power from sky, P_{sun} is the absorbed solar irradiance, the last term $P_{cond+conv}$ is the total absorb parasitic heat transfer, including convection and conduction. The definition of $P_{rad}(T)$, $P_{sky}(T_a)$ and P_{sun} are given in Eq.1.10 to 1.12

$$P_{rad}(T) = A_s \int_0^{2\pi} d\Omega \cdot \cos(\theta) \int_0^{\infty} d\lambda \cdot I_{BB}(\lambda, T)\, \varepsilon(\lambda, \theta) \tag{1.10}$$

where A_s is the surface area of the emitter $\varepsilon(\lambda, \theta)$ is the angular dependent emissivity of the emitter, λ is the wavelength of the light. The equation can be also written as frequency-dependent like above, but wavelength-dependent equation is more widely used for radiative cooling as it more intuitive.

$$P_{sky}(T_a) = A_s \int_0^{2\pi} d\Omega \cdot \cos(\theta) \int_0^{\infty} d\lambda \cdot I_{BB}(\lambda, T) \cdot \varepsilon(\lambda, \theta) \cdot \varepsilon_{sky}(\lambda, \theta) \tag{1.11}$$

where $\varepsilon_{sky}(\lambda, \theta)$ is the angular dependent emittance of sky.

$$P_{sun} = A_s \int_0^{\infty} d\lambda \cdot \varepsilon(\lambda, \varepsilon_{sky}(\lambda, \theta)) \cdot I_{sun}(\lambda) \tag{1.12}$$

where $\varepsilon_{sky}(\lambda, \theta)$ is the incident angle of sunlight, $I_{sun}(\lambda)$ is the total solar irradiance, including direct solar irradiance and diffused solar irradiance. Usually, the AM1.5 solar spectrum $I_{AM1.5}(\lambda)$ is used for most of radiative cooling discussion.

A comparison of stead-state temperature for ideal below-ambient and above-ambient radiative cooler is shown in Fig.1.7. Obviously, due to the minimized absorbed thermal radiation from sky, the steady-state temperature for below-ambient cooler is much lower than above-ambient cooler. The steady-state temperatures for both can be calculated by letting the outgoing thermal radiation equal to the absorbed thermal radiation. For below-ambient cooler, the steady-state temperature is

as low as 259K, for above-ambient cooler, the steady-state temperature is 285K. The temperature can change due to the atmosphere conditions, especially the humidity. For high-humidity region, the atmosphere emittance can increase due to the stronger absorption from water molecules, leading to a higher thermal radiation flux, which will heat up the cooler.

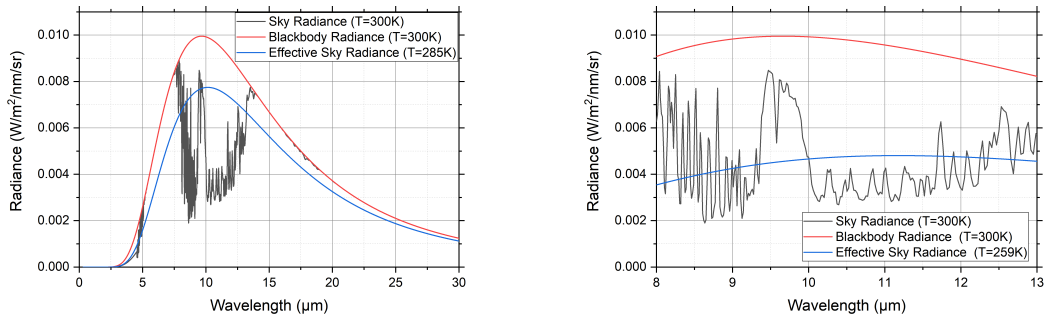

(a) Below-ambient cooler (b) Above-ambient cooler

Fig. 1.7. Steady-state temperature comparison of an ideal below-ambient and above-ambient radiative cooler. The thermal radiation of the coolers under steady-state temperature is equal to the absorbed thermal radiation from sky, which is noted by blue curves. If parasitic heat transfer is not considered, the steady-state temperature for both below-ambient and above-ambient radiative cooler can reach to a below-ambient temperature.

The cooling power of ideal below-ambient and above-ambient radiative cooler is shown in Fig.1.8. The net going cooling power is noted as the blue shaded area in both figures. It can be seen that for above-ambient cooler, the cooling power is much higher than below-ambient cooler. Therefore, depending on the applications, different types of coolers are required in order to achieve an optimal effect.

Usually, for building roof cooling, below-ambient cooling is more suitable as it can provide a lower steady-state temperature. On the other hand, for PV or CPV systems, due to the above-ambient operating temperature and high cooling power requirement, above-ambient cooler is obviously a better choice.

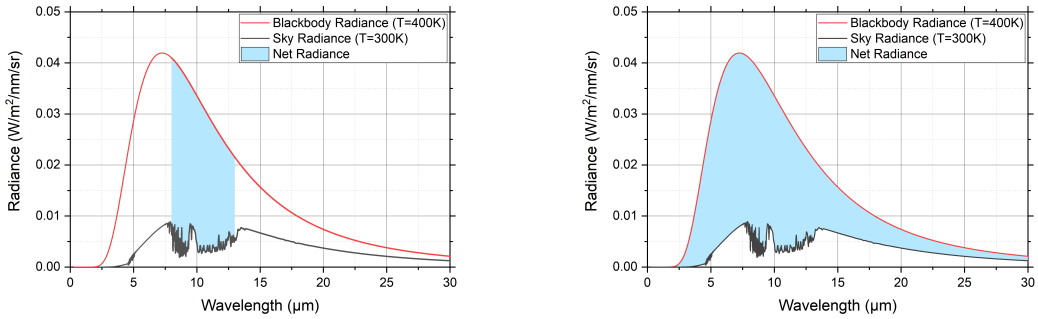

(a) Below-ambient cooling power

(b) Above-ambient cooling power

Fig. 1.8. Cooling power comparison of an ideal below-ambient and above-ambient radiative cooler under 400K, the net cooling power is noted as the blue areas. Obviously, for above-ambient cooler, the cooling power is significantly higher than below-ambient cooler at 400K

1.3 Previous work and development of radiative cooling

The application and study of radiative cooling can date back to centuries ago. At ancient time, people had been able to use radiative cooling for buildings or producing and storing ice, while the ambient temperature was still above freezing point [29–31]. The earliest documentation of radiative cooling as a physical phenomenon was written by Arago in 1828, according to the publication by Eriksson and Granqvist [31, 32]. Arago mentioned that during a serene night, small masses of grass, cotton, quilt, or any other filamentous substance having open access to sky can be 6 to 8 °C below the ambient temperature. This is well-known to farmers, because plants can get damaged by frost even if the ambient temperature is above freezing.

In more recent work, many experiments and simulations have been demonstrated to explore the potential of radiative cooling. Various materials and structures were used to build the emitter with desired emissivity profile [27, 32, 33]. The early modern work started in the 1970s, where nighttime cooling was studied most, as it is easier to achieve than daytime cooling. TEDLAR plastic films coated with aluminum back reflector were first reported to have the ability to reach more than 10 °C below

ambient during the night, with good encapsulation to reduce parasitic heat transfer [34, 35]. From 1980s to 1990s, more materials were investigated for the potentials of radiative cooling, among which the most popular materials were silicon monoxide (SiO), silicon dioxide (SiO_2) and silicon nitride (Si_3N_4), due to their strong absorption within atmospheric window. The coolers share an almost same structure, consisting the bulk material on top as the emitter and an aluminum layer coated at back as a reflector. The emissivities of each material and their compounds were studied for estimating the potential cooling power and steady-state temperature [26, 36–39]. Granqvist et al. have shown that the optical properties of silicon oxynitride depend on the mixing ratio of Si_3N_4 and SiO_2, the $SiO_{0.6}N_{0.2}$ was proposed to have a very strong cooling performance surpassing other compounds [38, 39]. If heat transfer was limited to radiation, the temperature drop during the night was predicted to be as great as 50 to 60 °C, with a cooling power around 100 to 120 W/m^2 [39–42].

Besides solid materials, certain gases were also found to exhibit relatively strong emission matching the atmospheric window [40–42]. Hjortsberg et al. demonstrated in their work that ethylene (C_2H_2) was capable to cool to 10 °C below ambient under diffused sunlight during daytime. Similarly, ammonia (NH_3) had also been tested under diffused sunlight and reached 9 °C below ambient. However, the gaseous emitter can be tricky to encapsulate and control, therefore their applications are very limited compared with solid emitters.

Pigment is another type of material which has been proved capable of radiative cooling applications [43–46]. Common white pigment with high solar reflectance such as titanium dioxide (TiO_2), Zinc sulfide (ZnS), Zinc selenide (ZnSe), Zinc oxide (ZnO), Barium sulfate ($BaSO_4$), Zirconium dioxide (ZrO_2), etc. was doped into polymer thin films and covered on a black emitter to test its cooling ability. The pigment reflects solar irradiance while keeping thermal radiation from back emitter almost unaffected, as a result of the high solar spectrum reflectance and infrared (IR) transmittance. The polymer used was usually polyethylene thin film which has a high transmission through entire solar and IR spectrum. Among these pigments, ZnS was found to

slightly outperform others and showed a 12 °C below ambient cooling capability during nighttime, while at daytime under direct sunlight, the temperature was 1.5 °C higher than ambient.

Although nighttime radiative cooling has been extensively studied and demonstrated, the daytime below-ambient cooling was not achieved until very recently. Traditional material and structure for radiative cooling is limited when producing both a strong IR emittance and a low solar absorption. Because of the intense solar irradiance, only 10% of solar absorption can cancel out the cooling power and lead to an above-ambient steady-state temperature [32]. The emergence and development of nanophotonics and metamaterials makes it possible to customize the emittance profile of a surface with a great flexibility [25, 28, 47–53]. This advantage has been taken to the research of radiative cooling for designing and fabricating top-performance selective emitters. Numerous materials and structures were demonstrated to have much stronger and flatter emittance in atmospheric window while still keep the solar absorption suppressed, resulting to a practical cooling power even under direct sunlight. A radiative cooler made up by two photonic crystal layers of quartz and silicon carbide (SiC) was reported by Rephaeli et al [28]. A multilayer broadband solar reflector comprised of magnesium fluoride (MgF_2), titanium oxide (TiO_2) and silver was sitting back at the emitter served as reflector. They have shown a theoretical cooling power of 100 W/m^2, and a 55 °C below ambient temperature can be reached if assuming 3% solar absorption and no parasitic heat transfer. Another experiment conducted by Raman et al. exhibited a 4.9 °C below-ambient cooling performance under direct sunlight, with a cooling power of 40.1 W/m^2 [48]. The cooler is 1D structured nanophotonic consists of seven layers of silicon dioxide (SiO_2) and hafnium dioxide (HfO_2), which was encapsulated in an apparatus with an estimated effective heat transfer coefficient of 6.9 $W/m^2/K$. Similar to this work, a simpler cooler structure was proposed using polydimethylsiloxane (PDMS) front-coated silica wafer, and the back side of wafer was coated with silver as reflector [53]. The structure shows a strong and flat broadband emittance from 5 to 20 μm, yet a very low

absorption in solar spectrum. The cooler was sealed in a Petri dish and covered by polyethylene film, with an aerogel blanket at bottom to block the conduction heat transfer. Even exposed to direct sunlight, a 8.2 °C below-ambient temperature was achieved, yielding a cooling power of 127 W/m^2. In order to get a maximum temperature drop from the cooler, the conduction and convection heat transfer have to be eliminated. To achieve this goal, Chen et al. [25] used a vacuum chamber in their work to store the cooler and tested the daytime cooling temperature. An aluminum shield was also used to block the direct sunlight. The cooler was made of Si_3N_4, Si and an aluminum reflector. The lowest temperature reached was -22 °C, or 42 °C below ambient, providing a sub-freezing cooling capability.

Nanophotonics based emitters have shown a promising future for high performance daytime radiative cooling. However, the complicated structure and manufacture process makes it very difficult for large scale fabrication. Fortunately, a new type of low-cost radiative cooler using nanoparticles doped thin film was reported to have the ability for daytime below-ambient cooling, in addition to that, the flexibility brought by thin film structure giving the cooler a wide range of applications [52, 54–56]. Similar as pigment based radiative coolers, nanoparticles are doped into a thin film made of optical transparent material, such as polyethylene (PE), TPX family of polymethylpentenes, or acrylic resin to fabricate radiative cooler. The nanoparticles reflect more than 90% of sunlight, while transmit most of the IR radiation. The thin film cooler can be placed on any surface under the sky, such as roofs of buildings, to cool down the target area. SiC, SiO_2, and TiO_2 were the most popular material for nanoparticles. A TPX film embedded with SiO_2 microspheres with radius of $\sim 4\ \mu m$ was reported to have a cooling power of 97 W/m^2 under direct sunlight at noon, and a 110 W/m^2 average cooling power during a 24 hours experiment [52]. The thin film was placed in open air during the experiment without blocking any parasitic heat transfer. The cooling power was measured by a feedback-controlled electric heater, which keeps the temperature of cooler surface almost the same as ambient. The heating power is thus the same as cooling power of the cooler. A similar work from Huang

[55] proposed a double-layer nanoparticles embedded acrylic resin and analyzed the performance for daytime and nighttime cooling. The emitter consists of a TiO_2 particles doped top layer and a carbon black particles doped bottom layer, serving as solar reflector layer and IR emitter, respectively. The predicted cooling power is 180 W/m^2 for nighttime and 100 W/m^2 for daytime. It can be seen that the nanoparticles based emitters have a comparable cooling performance than nanophotonic emitters, plus the lower fabrication cost, nanoparticles emitters have become an appealing option for radiative cooling.

1.4 Radiative Cooling for CPV

As discussed above, radiative cooling is one of the most suitable thermal management methodologies for CPV. The theoretical potential of radiative cooling on PV and CPV has been studied in several recent publications [13, 33, 57, 58], while experiments have also been demonstrated to investigate the real performance of radiative cooling in CPV [59]. In Zhou et al.'s work, a gallium antimonide (GaSb) cell was tested under 13 suns, 10 °C temperature drop of the cell was achieved by applying a soda-lime glass cooler coated with aluminum at back surface. The open-circuit voltage increased $20mV$, and the estimated increase of lifetime is 40%. Although the previous experiment has shown a good outcome, the cooling efficiency is predicted to have a much greater capability under higher concentration.

In this work, a novel structure of CPV system was designed and fabricated to achieve a higher concentrating factor and better cooling performance. Experiments were conducted under different weather conditions to test the temperature drop and open-circuit voltage of a GaSb solar cell. The concentration factor of the demonstration set up was around 39 suns. GaSb is picked as our subject is because its low-band gap. GaSb can be used in multi-junction or thermophotovoltaic cells as the absorbing layer for long-wavelength photons. However, low-band gap solar cells usually have a smaller open-circuit voltage, which makes it more sensitive to high

temperature. The drop of efficiency could be more serve compared with Si solar cells, thus limiting the overall efficiency. Fortunately, by applying a double-sided soda-lime radiative cooler, the measured temperature drop for GaSb cell at steady-state was as high as 36 °C, and the increase of open-circuit voltage was around 0.08V, which can be interpreted to a 4 to 13 times extension of lifetime (5 to 14 times in total) [60–64]. To better understand the physics of radiative cooling, detailed simulation which excellently reflected the experiment conditions was performed to study cooling performance quantitatively. According to the results, a total cooling power of around 250 W/m^2 produced by the cooler was estimated. The viability and capability of applying radiative cooling to CPV has been verified.

2. METHODOLOGY

To demonstrate the performance of radiative cooling, a concentrated photovoltaic setup must be designed and fabricated. The setup should be able to track the sun to focus the sunlight onto a solar cell and monitor the temperature and open circuit voltage. The field test should be conducted outside where has open access to clear sky in order to maximize the radiation power of the coolers. Due to the various weather conditions, keep every experiment at an identical environment is almost impossible. Sun position, temperature, wind speed, atmosphere condition, etc. can change every second. Therefore, each outdoor experiment has its only unique data and it is very hard to be repeated at a different time. To fix this issue, the setup must have two independent chambers with a same structure, but one installed cooler and the other one installed a low emissivity surface, such as a metal disk, as a contrast. The recorded data of two chambers can thus be compared because the experiments are conducted simultaneously, the variations caused by random weather conditions can be offset.

2.1 Setup Design

The basic considerations of each chamber are discussed in this paragraph. First question is how to concentrate sunlight. The most common ways for concentrated photovoltaics are using a Fresnel lens or parabolic mirror, among which the Fresnel lens is a better option due to its accessibility, compatibility, good optical property and low price. Next, the cooling assembly for both chambers should have a good thermal conductivity to uniformly transfer heat from solar cell to cooler, or the metal disk. The surface area of cooler and metal disk should be large enough to achieve a high cooling efficiency. To investigate the cooling power of thermal radiation, convection and conduction heat transfer of the chamber need to be suppressed by the chamber

walls. A sealed housing with low thermal conductivity, like a rigid foam, can be used to enclose the cooling assembly inside. This can not only reduce convection and conduction, but also protect the assembly from dust and keep it unaffected by wind, which can potentially bring noise to the temperature data. The sunlight needs to be guided and focused on the solar cell without being blocked by the chamber walls. Similarly, the thermal radiation from cooler also needs to have open access to the sky. Therefore, openings on chamber walls are needed to transmit radiation for both sunlight and thermal radiation, and a transparent thin film can be used to seal each opening.

The sketches of two most promising designs are shown in Fig.2.1 and Fig.2.2. The structures inside chamber for both designs are identical, the only difference is how sunlight is guided to the solar cell. Design 1 contains two mirrors tilted 45 °to reflect sunlight onto a Fresnel lens. The lens focuses the sunlight on the solar cell inside the chamber, through a layer of transparent thin film. The solar cell is connected to a large heat spreader to uniformly conduct heat to the other side, where the cooler is located. The cooler then absorbs heat from spreader and emits it out through the thin film. The cooler and solar cell are installed on different sides of the heat spreader so that the thermal radiation from cooler is not affected by the Fresnel lens, and can directly exchange heat with clear sky. Design 2 shares a same structure of chamber, however, only one mirror is used to reflect the sunlight. The entire chamber is tilted at a certain angle, and the mirror is placed on top of the base board horizontally.

Design 1 is straightforward and easy to fabricate. However, using a second mirror can cause additional optical loss and reduce the concentration factor, leading to a poorer performance. In addition, a high-reflectance first surface mirror is usually very expensive, the extra mirror can also significantly increase the cost of the setup. Design 2 was finally adopted as it can avoid these issues by only using one mirror for each chamber, but the structure must be well-designed to fix the chamber firmly and accurately at a desired tilt angle. Based on the discussion above, a finalized structure was designed and illustrated in the next chapter.

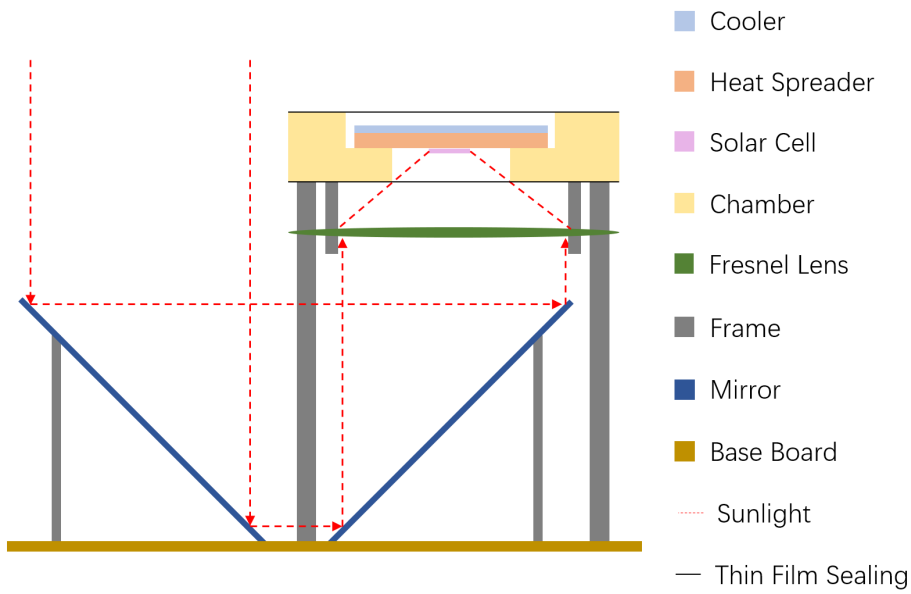

Fig. 2.1. Design 1, the sunlight is reflected twice by the two 45° tilted mirrors. The chamber is horizontally fixed on the base board.

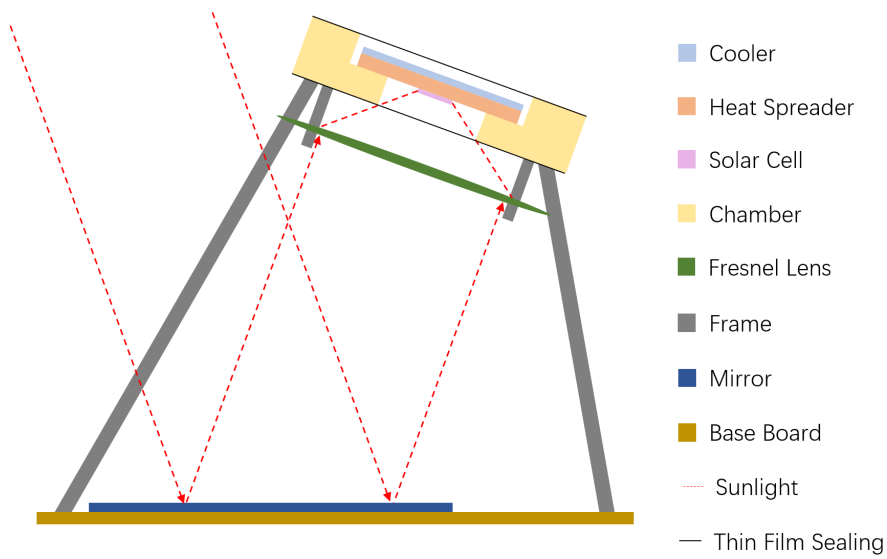

Fig. 2.2. Design 2, the sunlight is reflected once by the mirror. The chamber is tilted 20° and fixed on the base board.

2.2 Setup Structure

The setup for radiative cooling demonstration consists of three chambers. As illustrated in Fig.2.3, each chamber is designed for different functions. The one on the left (chamber 1) contains a solar cell and two radiative coolers, while the one on the right (chamber 2) shares a similar structure but does not have any cooler, which serves as a comparison. The chamber in the middle (chamber 3) only has a thermal power sensor which keeps tracking the incident solar power, the data is logged in a computer for the later use in simulation. All chambers are tilted 20 °and fixed on a wood board to maintain at a same level. The 20 °was used as the tilt angle is because the smallest zenith angle of West Lafayette is around 40 °in August and September, when experiments were conducted. By tilting the chambers, the top cooler can have a greatest view factor to the sky. The wood board is held by a tripod, which its tilt and azimuth angles can be adjusted to track the sun. Three first surface aluminum mirrors (#40-067, Edmund Optics) are placed on the board under each chamber, separately, to reflect sunlight normally to the acrylic (PMMA) Fresnel lens (#32-593, Edmund Optics). A PMMA rod is fixed in front and tilted 20 °as a solar tracker. The solar tracker is well aligned, therefore by adjusting the tilt and azimuth angle of the setup, one can eliminate the shadow of solar tracker to ensure the reflected sunlight is normally incident on the lenses. When operating, the entire setup is manually adjusted every 5 minutes to track the sun.

The detailed structures for each chamber are shown in Fig. 2.4 to Fig.2.8, with both rendered 3D images and 2D plots. For chamber 1, the outside enclosure is made of polystyrene(PS) foam, which can significantly suppress convection and conduction heat transfer. Two highly transparent Low-density polyethylene (LDPE) films (ET311115, Goodfellow Co.) are used to seal the openings on top and bottom of the chamber, respectively. This can reduce convection as well as temperature fluctuation caused by wind gusts, without affecting radiative cooling. Inside the chamber, the solar cell, aluminum nitride (AlN), copper heat sink and coolers on top and bottom

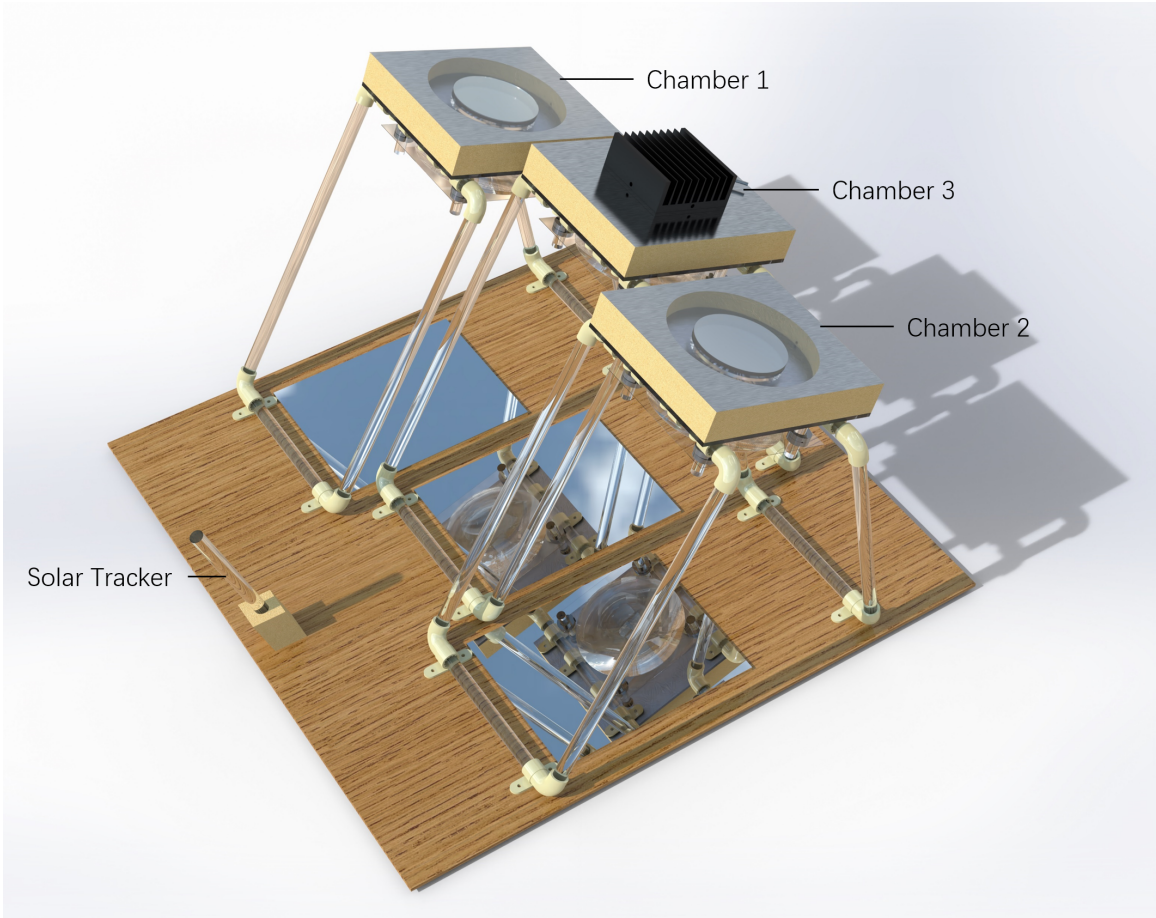

Fig. 2.3. A rendered picture of the demonstration setup. The cables and data collector are not shown in the picture.

are pasted together as a cooler assembly disk by thermally conductive silver adhesive (Pyro-Duct^{TM} 597-A). The inner side of the coolers are coated with 300 nm aluminum as reflection layer. The disk serves as a heat spreader which can uniformly conduct heat from solar cell to coolers. Next, the disk is held by four Teflon cubes and glued on top of a PMMA ring, the PMMA ring is then bonded on the chamber. The two layers of Teflon cubes and PMMA ring are heat resistance which limit the conductive heat transfer from disk to chamber walls, preventing the foam from melting due to high operating temperature. The top surfaces of the chamber are covered with aluminum sheets to reduce sunlight absorption. A set of probes are connected to the electrodes

of GaSb solar cell, a type-K thermocouple (TC, SCASS-020U-12-SHX, Omega) is mounted with silver adhesive (Pyro-Duct™ 597-A) on copper heat sink next to the solar cell to measure the temperature. The data is collected by a four-channel USB voltage and thermocouple DAQ (DI-245, DATAQ) to monitor the open circuit voltage and temperature of solar cell, with 2 Hz sampling rate. The resolutions are 0.096°C and 0.12 mV, respectively.

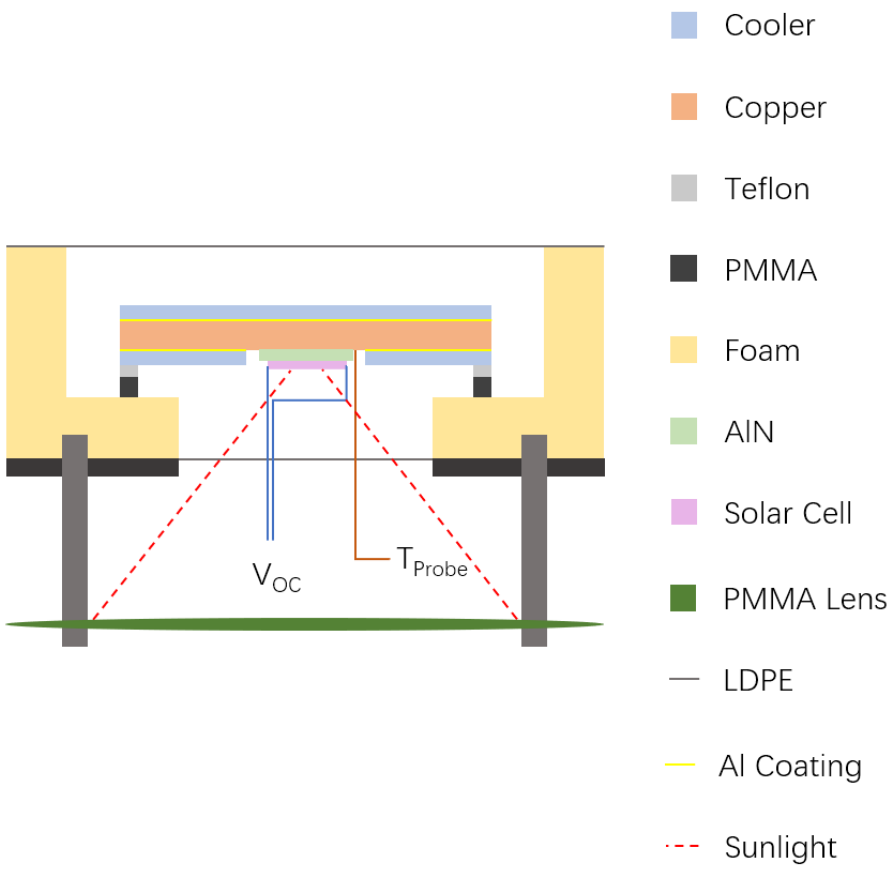

Fig. 2.4. The cross-section of chamber 1. Two soda-lime glass coolers are used to dissipate heat.

Chamber 2 has an almost identical structure as chamber 1, but does not have coolers. The copper heat sink is coated with 300 *nm* aluminum on both sides. An aluminum disk is pasted on top of the copper disk as a contrast to the cooler.

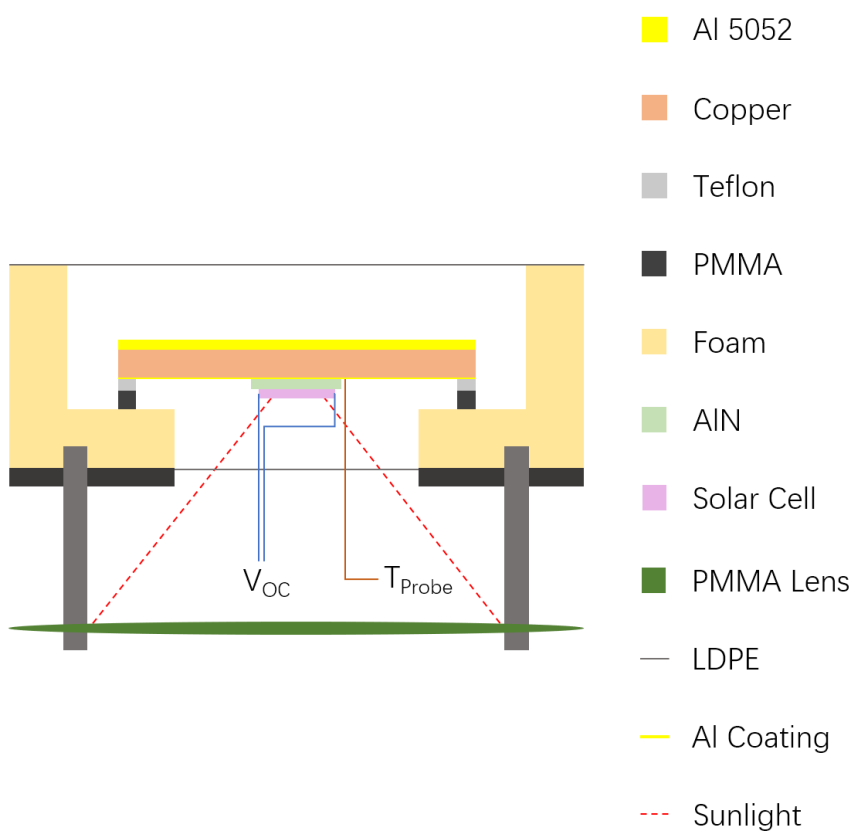

Fig. 2.5. The cross-section of chamber 2. An aluminum disk is pasted on top as a comparison to the cooler, the bottom is coated with 300 nm aluminum.

Chamber 3 has a same enclosure as chamber 1 and 2, while the inside assembly is replaced with a thermal power sensor (S314C, Thorlabs). A meter console (PM100D, Thorlabs) is connected to the sensor to monitor the power reading. The purpose of chamber 3 is to measure the focused solar power. Because of the same structure, the measured solar power in chamber 3 should be very close to the power incident on each solar cell in chamber 1 and 2 during experiment. The key sizes of each component are listed in Tab. 2.1

The thermocouple is pasted on the copper plate very close to the solar cell, to guarantee the measured temperature is as close to the temperature of solar cell. A set of photos in Fig.2.9 show the contact point of thermocouple and electrodes.

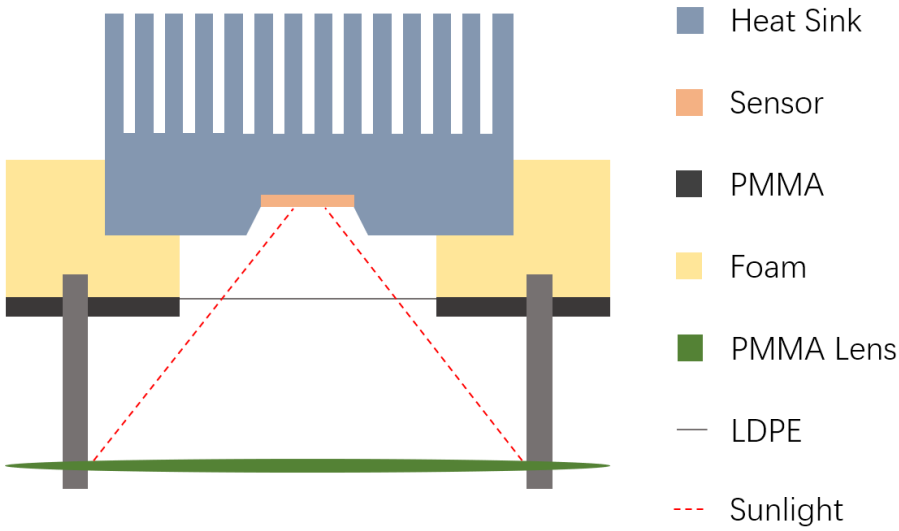

Fig. 2.6. The cross-section of chamber 3. A thermal power sensor is fixed inside the chamber to measure the focused sunlight.

Table 2.1. The key sizes of each component

Component	Size $[in]$	Thickness $[in]$	Area $[in^2]$
Copper Heat Sink	$\emptyset = 4$	0.13	12.57
Cooler	$\emptyset = 4$	0.02	12.57
Al Disk	$\emptyset = 4$	0.04	12.57
Solar Cell	0.6×0.4	0.02	0.024
Al Mirror	10×8.03	0.24	80.3
PMMA Lens	$\emptyset = 6$	0.06	28.27

The reflectance or transmittance of aluminum mirror, PMMA lens, LDPE film is shown in Fig.2.10. The spectrum direct normal irradiance (DNI) data of West Lafayette extracted from National Solar Radiation Database (NSRDB) is also shown in the same figure for reference. The optical loss of the system is minimized by using first surface aluminum mirror, PMMA Fresnel lens and LDPE film, due to the high reflectance and transmittance. All data from 0.3 to 2.5 μm is measured by

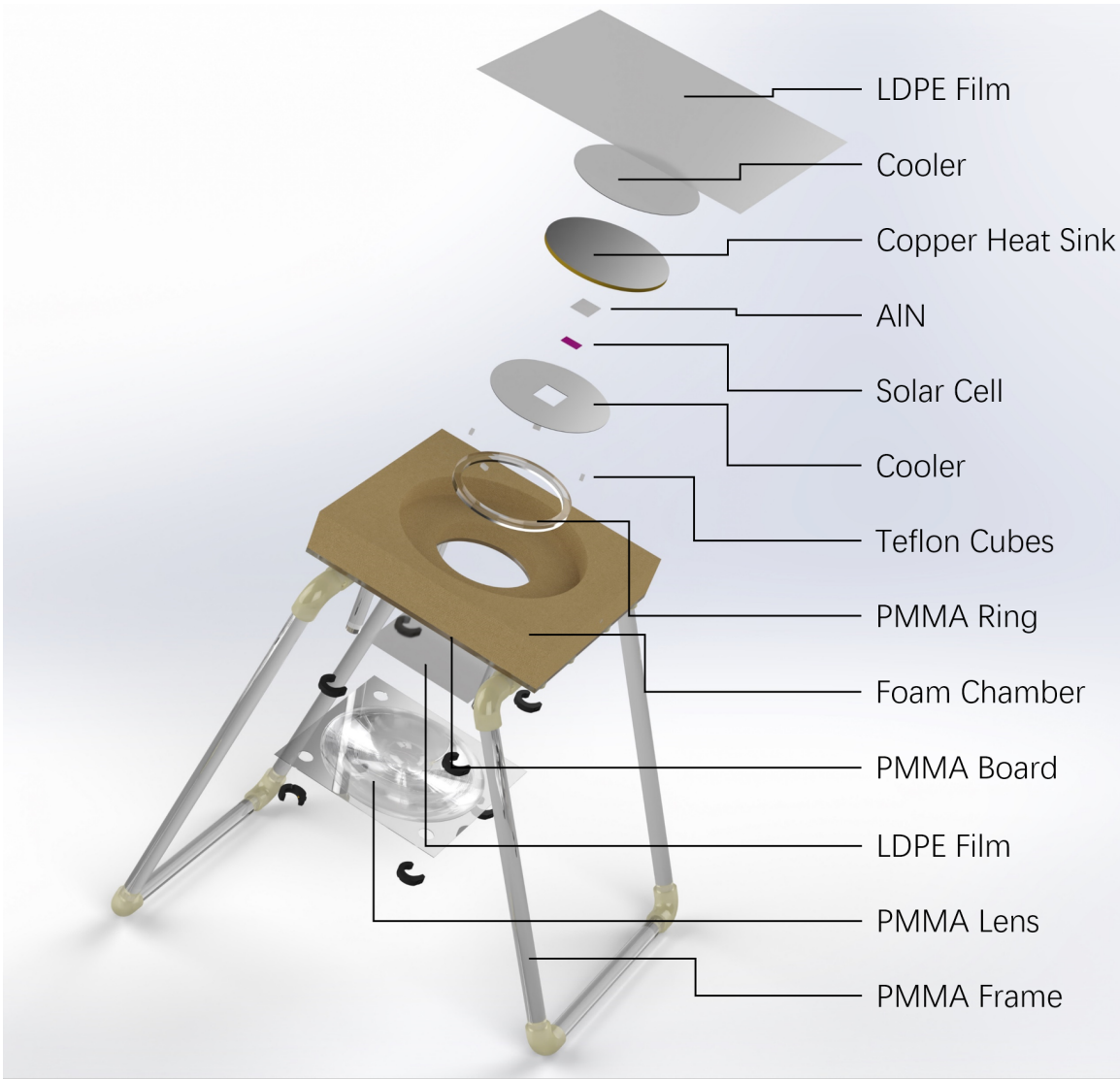

Fig. 2.7. A rendered picture of chamber 1.

spectrophotometer (Lambda 950, PerkinElmer), data above 2.5 μm is measured on an FTIR (Nexus 670).

The emittances of aluminum disk and cooler are shown in Fig.2.11. The emittance of clear sky in summer of West Lafayette is shown in same figure as reference. Both aluminum disk and cooler have a low emittance from 0.3 to 4 μm, minimizing the heating caused by sunlight. The emittance of cooler above 5 μm jumps up quickly, with an average value close to 0.8 *in* the atmosphere transparency window. This

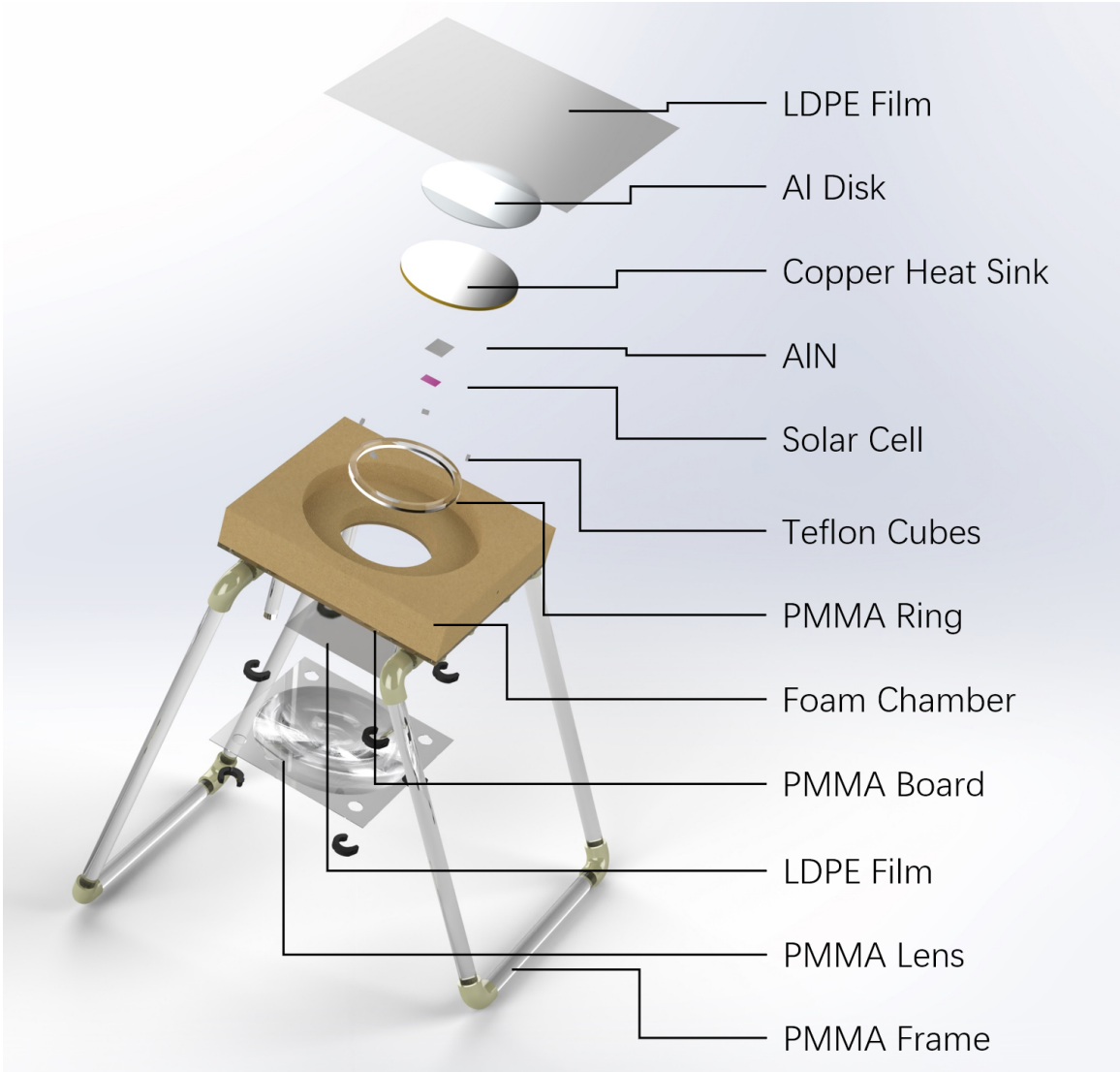

Fig. 2.8. A rendered picture of chamber 2.

leads to a high radiation power output which keeps the temperature of the cooler at a relatively low level. On the contrary, the aluminum disk only has an emittance around 0.05 above 5 μm and does not emit radiation as much as the cooler. This emittance difference is the reason of the significant temperature dropping brought by the coolers. The emittance data for both cooler and Al disk from 0.3 to 2.5 μm is measured by spectrophotometer (Lambda-950, PerkinElmer), data above 2.5 μm for cooler is measured on an FTIR (Nexus 670), data for Al disk above 2.5 μm is

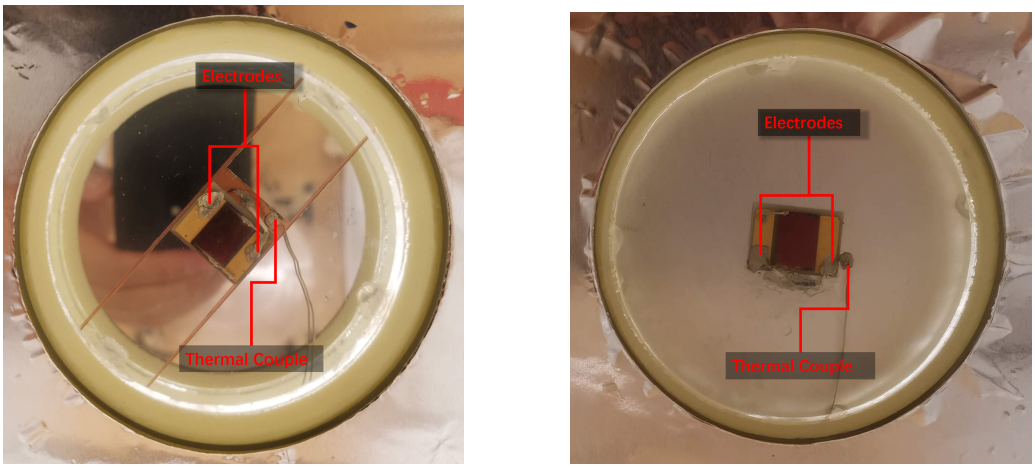

(a) Chamber 1 (b) Chamber 2

Fig. 2.9. Real photos showing the configuration of electrodes and thermocouples

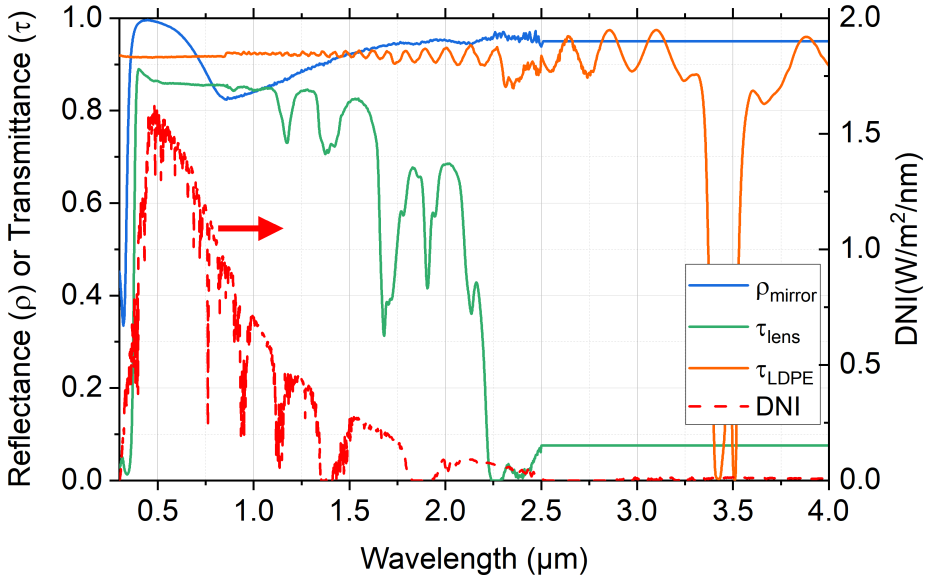

Fig. 2.10. Reflectance and Transmittance of Concentrating System. The direct normal irradiance (DNI) is also shown as the red dot line. The transmittance and reflectance of mirror, lens and LDPE film are relatively high within the solar spectrum, to reduce the optical loss.

interpolated as 0.05. The data was not measured on FITR due to the limitation of our equipment. The surfaces of Al disk is slightly diffusive, as a result, part of the reflection cannot be fully captured by FTIR. On the other hand, Lambda-950 uses integrating sphere to collect light, ensuring a reliable result.

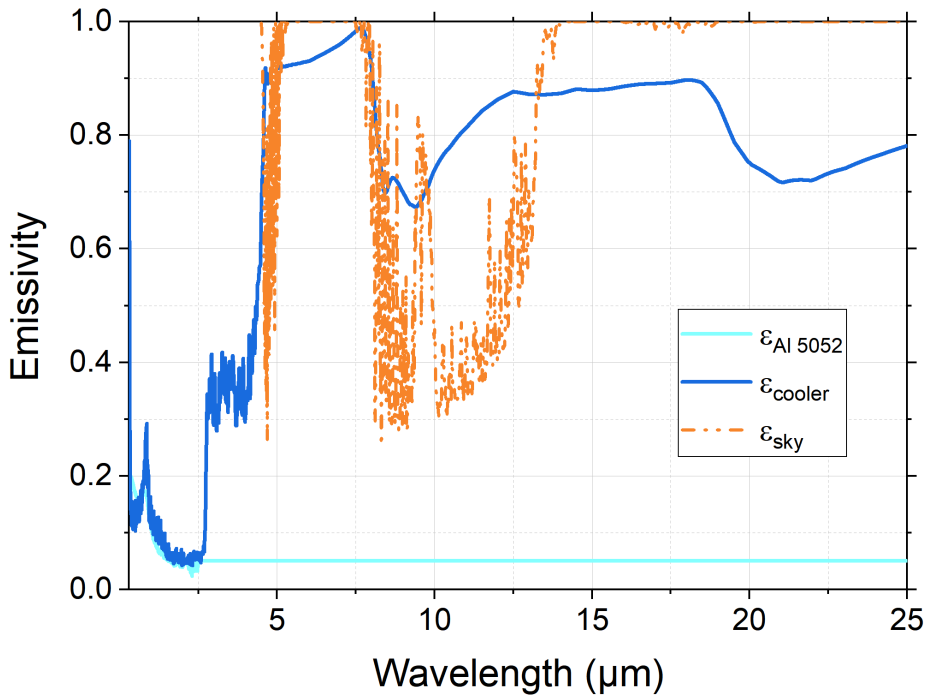

Fig. 2.11. Emissivity of Al coated soda-lime glass cooler, Al 5052 and sky. Data for cooler is measured on Lambda-950 and FTIR. The cooler has a high emissivity in the atmosphere transparency window. Data for Al 5052 from 0.3 to 2.5 μm is measured on Lambda-950, and data above 2.5 μm is extrapolated to an emissivity of 0.05.

The absorptance of GaSb solar cell is shown in Fig.2.12. This data will be used in simulation chapter. Not all focused sunlight will be absorbed by solar cell, therefore the measured incoming solar power by thermal sensor in chamber 3 needs to be adjusted based on the absorption spectrum of the solar cell.

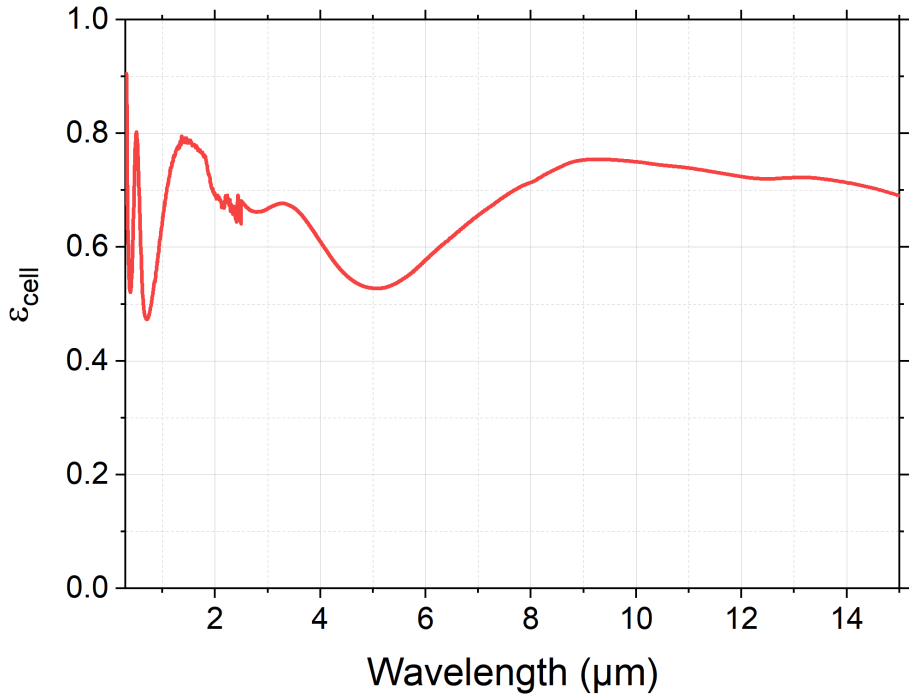

Fig. 2.12. Emissivity of GaSb solar cell. Data is measured on Lambda-950 and FTIR

3. EXPERIMENT

Four experiments were conducted at West Lafayette (coordinates 40.4221, -86.9318) under different conditions to study the performance of radiative cooling. This site was chosen because it has an open access to sky almost without any trees and buildings blocking the cooler, so that the view factor to sky is maximized to ensure the performance of radiative cooling. Fig.3.1 is photo taken during an outdoor experiment, the setup was aligned by adjusting the tilt and azimuth angles to let the sunlight focus on three chambers. A brief description of each experiment is listed in Tab.3.1. Purpose, date and time, weather conditions and key results of each experiment are shown in the table.

Table 3.1. Experiment conditions

Exp. Number	1	2	3	4
Purpose	Chamber Comparison	Night Cooling	Daytime Cooling	Daytime Cooling
Preprocessing	Covered Al sheets	-	-	-
Date	2019/8/23	2019/8/25	2019/8/28	2019/9/14
Time	1:00 PM	2:00 AM	1:00 PM	1:00 PM
Weather	Partly Cloudy	Fair	Partly Cloudy	Fair
Temperature	26 °C	16 °C	26 °C	26 °C
Windspeed	20 km/h	13 km/h	20∼30 km/h	6 km/h
Humidity	45%	85%	40%	44%
Avg. Solar Power	4.86 W	-	5.61 W	6.03 W
ΔT	1 °C	3 °C	31 °C	36 °C
ΔV_{OC}	-	-	0.074 V	0.078 V

The purpose of experiment 1 is to check if chamber 1 and 2 have the same convection coefficient. Before experiment, two aluminum sheets with diameters of 4 *in* were covered on top of the assembly disks in chamber 1 and 2, respectively. Another two aluminum sheets with a one-inch diameter hole at center were covered on bottom

Fig. 3.1. Aligned experiment setup during outdoor test. Specifically, Avg. Solar Power indicates the average solar irradiance during the entire experiment measured by thermal sensor; ΔT is the steady-state temperature difference of chamber 1 and 2; ΔV_{OC} is the steady-state open-circuit voltage difference of solar cells in chamber 1 and 2

of the assembly disks, respectively, without blocking the light focused on solar cells. By covering four aluminum sheets, the heat transfer through thermal radiation of chamber 1 and 2 maintains equivalent. Ideally, the temperatures of the two chambers will be the same. The setup was warmed up under sunlight for 20 minutes to let the sensors reach a steady state temperature, in order to give a reliable reading. The tilt and azimuth angles of the setup was adjusted every 5 minutes to keep the focused

beam spot falling at center of the solar cells. A chair was used to stabilize the setup together with the tripod. The setup was placed on ground firmly enough to prevent any vibration caused by wind. The real-time temperatures of two chambers are shown in Fig.3.2. Both chambers went up and down at a same pace from 13:30 to 14:20, indicating an almost identical conduction and convection coefficient. The temperature dropping started from 14:11 was due to clouds. At 14:20, the four aluminum covers were taken off, as shown in the yellow area, the temperature of chamber 1 began to decrease rapidly caused by the largely increased thermal radiation from coolers, while the chamber 2 stayed almost unaffected. The temperature difference kept growing until reached its peak after 40 minutes. The largest temperature difference was around 22 °C, this does not imply the full potential of radiative cooling of the setup because the weather was cloudy. The temperature of both chambers can go higher under fair weather condition, leading to a greater temperature difference, which will be shown later.

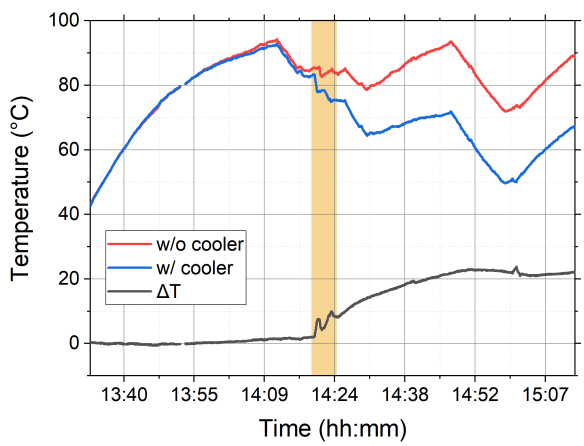

Fig. 3.2. Temperature data for experiment 1. Yellow area indicates the time of Al covers being taken off

The purpose of experiment 2 is to check the performance of the radiative cooling at night, and provide information under a different condition for more simulation data input. Two chambers were set to their normal configurations as discussed previously,

without covering any aluminum sheets. The time was chosen at 2 am during night, when the diffused sunlight was completely gone. To ensure the top cooler having a greatest view factor to clear sky, the set up was tilted at an angle of 20 °, letting the top surfaces of the cooler and aluminum disk to be parallel to horizontal plane. No further adjustment needed during the test. As shown in Fig.3.3, due to a larger thermal radiation from coolers, the temperatures of chamber 1 dropped faster than the other one at first. Then, temperatures of both chambers gradually stabilized and reached steady state at 2:57 am. The temperature of chamber 2 reached around ambient temperature at last, while chamber 1 was below ambient. This is because aluminum disk almost does not emit thermal radiation, the heat transfer of chamber 2 was dominated by conduction and convection and finally became the same temperature as ambient. On the contrary, the coolers in chamber 1 appears nearly like a blackbody within atmosphere transparency window. It can exchange heat to outer space with a much lower temperature than ambient. The larger radiation power caused by coolers led to a temperature drop of 3 °C.

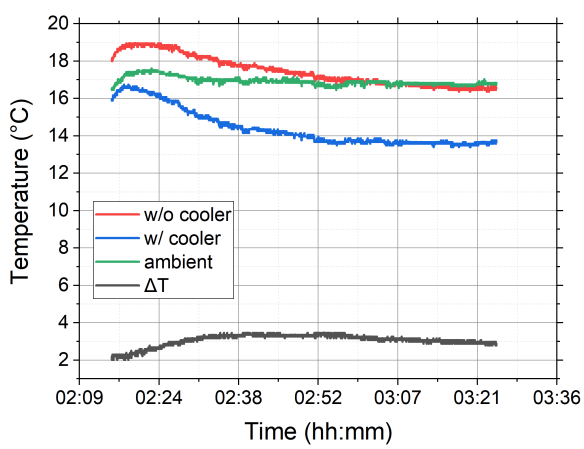

Fig. 3.3. Temperature data for experiment 2.

The last two experiments demonstrate the radiative cooling performance during day time. Experiment 3 was conducted on a cloudy day, while experiment 4 was on a sunny day. The experiments were carried out in a same way as experiment 1, but no

aluminum sheets were covered on either chamber. The setup was warmed up under sunlight for 20 minutes, and the tilt and azimuth angles of the setup were adjusted every 5 minutes to track sunlight. The temperature and open circuit voltage (V_{OC}) of solar cell were measured and logged in a laptop at a rate of 2 Hz for both chamber 1 and chamber 2. The thermal power meter in chamber 3 measured and logged the input solar irradiance at a rate of 1 Hz.

For experiment 3, the real-time solar irradiance, temperatures and V_{OC} of solar cells in both chambers are shown in Fig.3.4 and Fig.3.5. The averaged peak solar irradiance was maintained around 6.3 W during the experiment, which converts to a DNI of 1040 W/m^2. The valleys in temperature were caused by clouds blocking the sun, due to the overcast weather. The dips in both curves of V_{OC} are omitted to give a clearer look. As a result of weather condition, the temperatures did not increase monotonically. Each temperature drop during the experiment corresponds to a power valley of solar irradiance. The initial temperatures of chamber 1 and 2 were very close, at around 38 °C for chamber 1 and 40 °C for chamber 2. The V_{OC} of solar cell in chamber 1 was 0.41 V, while solar cell in chamber 2 was 0.4 V. The difference of temperature and V_{OC} were the smallest at beginning. As heated up by sunlight, temperatures of both chambers went up, inducing a V_{OC} decreasing of both cells. Obviously, the temperature of chamber 1 increased slower than chamber 2. Given the almost identical conduction and convection coefficient of the two chambers, this temperature difference is mainly a result of extra heat dissipation by radiative cooling. The V_{OC} of chamber 1 also dropped slower than chamber 2, which means theoretically a higher power output. The zigzag curve of V_{OC} was due to manually solar tracking, each jump in the curves indicates one adjustment of tilt and azimuth angles. It can also be noticed that the V_{OC} increases in chamber 1 at each jump, but decreases in chamber 2. This is likely caused by the different local absorptance of the two cells. Both chambers reached peak temperature at 14:08, and started to fluctuate with solar irradiance. The temperature drop caused by coolers was 31 °C at their peak values. This significant temperature decreasing led to a higher open

circuit voltage around 0.07 V. The temperature decrease and V_{OC} increase can be even higher in a sunny day.

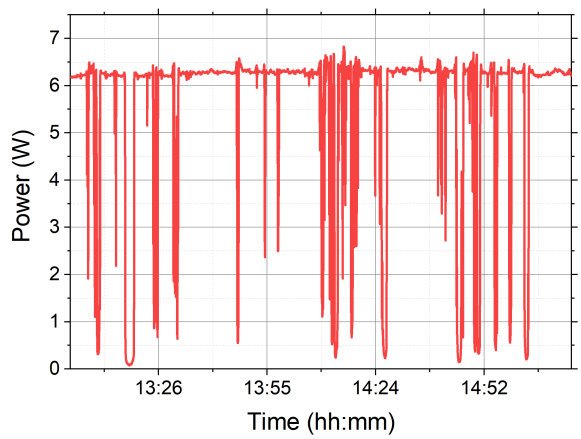

Fig. 3.4. Solar irradiance for experiment 3

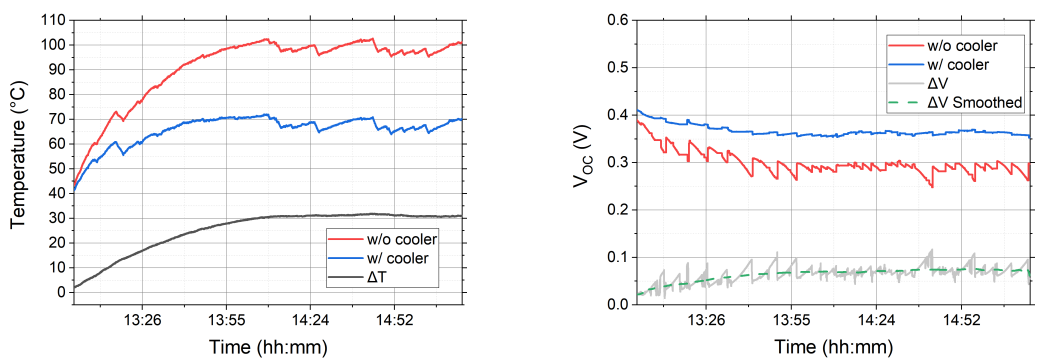

(a) Temperature

(b) Open-Circuit Voltage

Fig. 3.5. Experiment data for experiment 3. The valleys caused by clouds in open-circuit voltage curves are removed

Experiment 4 was tested on a sunny day. The results are shown in Fig.3.6 and Fig.3.7. As seen in Fig.3.6 , the solar irradiance was a lot smoother than experiment 3, which led to a steadier temperature and V_{OC} for both chambers. The average peak irradiance was around 6.1 W, corresponding to a DNI of 1019 W/m^2, which was slightly lower than previous experiment. The initial temperatures were at 49 °C for

chamber 1 and 57 °C for chamber 2, the larger temperature difference at beginning was because of a slightly longer warm-up time. Similar as former experiment, temperature of chamber 1 increased slower than the other one, and reached at a lower steady state temperature, compared with chamber 2. Both chambers reached at steady-state at roughly 14:30. The temperature drop brought by coolers was as large as 36 °C, which is even 5 °C greater than experiment 3. Consequently, the V_{OC} of solar cell in chamber 1 reduced at a lower rate, and stayed around 0.08 V higher than chamber 2.

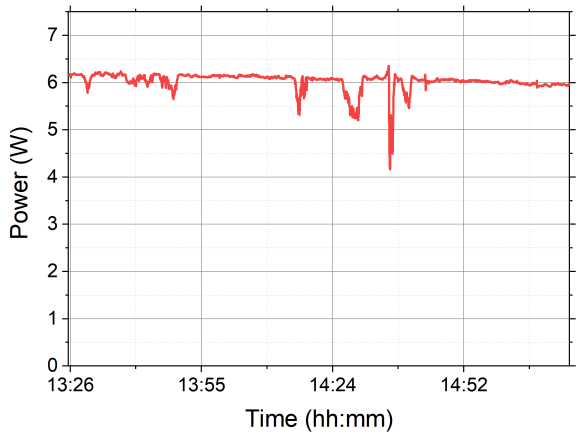

Fig. 3.6. Solar power data for experiment 4

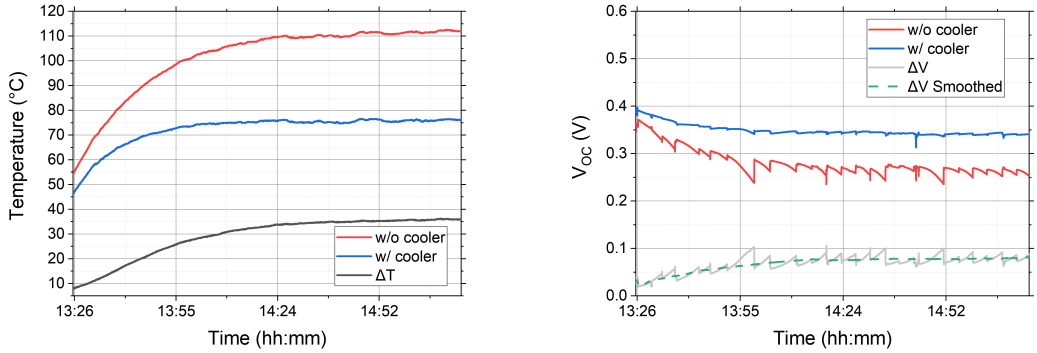

(a) Temperature

(b) Open-Circuit Voltage

Fig. 3.7. Experiment data for experiment 4.

4. SIMULATION

To have a better understanding of physics behind radiative cooling, simulations are needed to verify the experimental results. The performance details of radiative cooling need to be studied quantitatively as well. Furthermore, other potential applications of radiative cooling which are difficult to be examined by experiment can also be tested on simulation. This can be achieved by simply defining a different set of structure, inputs and boundary conditions in simulation model. The simulation software used is COMSOL Multiphysics [65]; all subsequent figures presented in this section are derived from this software. The transient heat transfer, including conduction, convection and radiation, is modeled in the software to study radiative cooling. Experiment 1 is not modeled since it is only a convection coefficient test to check if both chambers are having the same heat loss rate. Additionally, because the aluminum covers were taken off during the experiment, it is hard to be captured in simulation tool. Experiment 2, 3 and 4 are simulated with data based on real experimental conditions.

4.1 Geometry

To ensure the accuracy of simulation results, a geometry reflecting the real configuration of the setup is necessary. An identical 3D geometry as introduced before was imported to COMSOL directly to compute the transient heat transfer. However, due to the complex structure and physics process, the estimated computing time for a single experiment was more than a week, using a mid-level desktop processor. Many parameters had been refined to try to improve the efficiency, nonetheless, the computing time was still far beyond our expectations. A simplified geometry must be used to reduce the massive calculation.

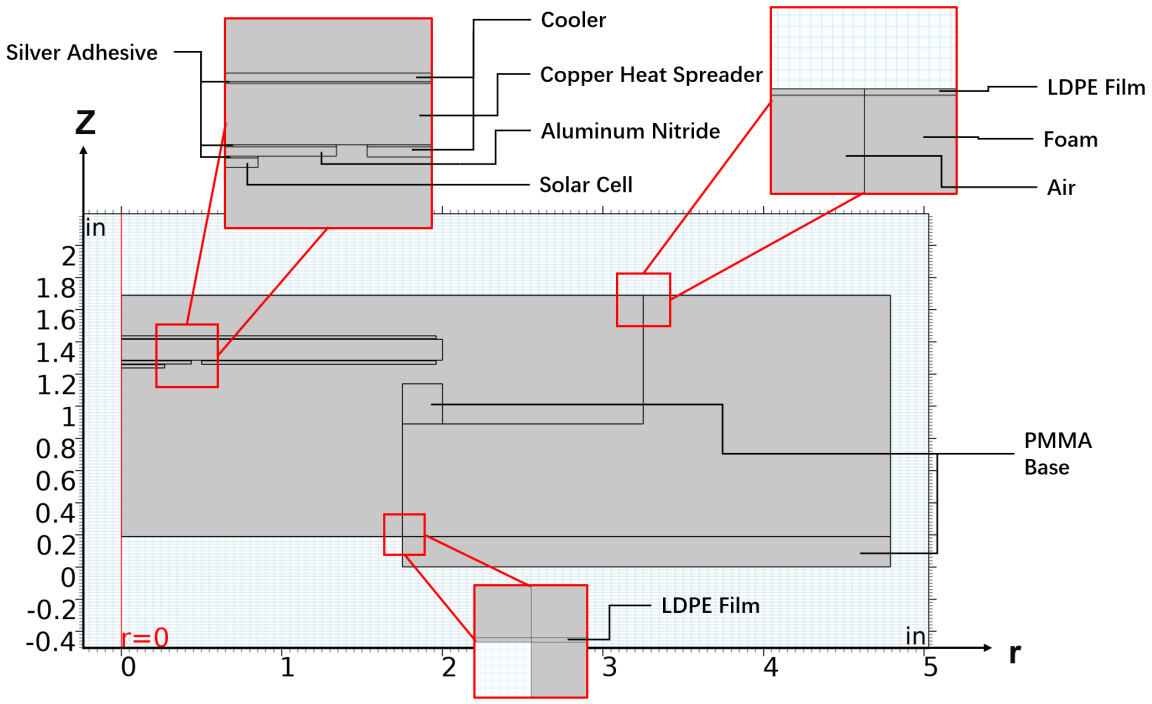

Fig. 4.1. The 2D geometry of chamber 1

To improve the efficiency, a 2D axisymmetric structure is used as an approximation of the real structure. As seen in Fig.4.1 and Fig.4.2, every component is defined as either a disk or a ring in the 2D structure, the symmetric axis is shown as the red line at r = 0. Several modifications have been made to build this structure, including the Teflon cubes, solar cell, aluminum nitride, bottom cooler and chamber housing. The four Teflon cubes cannot be defined in an axisymmetric structure as it will block the air flow inside the chamber, thus in this geometry the cooling assembly is floating in the air without direct contact with PMMA ring. The influence of missing the Teflon cubes is negligible since the total contact surface area is very small compared with the copper disk. Other minor changes are the shapes of solar cell, AlN substrate and bottom cooler. The solar cell, AlN and cooler are replaced with two disks and a ring with the equal surface areas and thickness, respectively, to keep the total conducted heat almost same. The air holes, screws and nuts in the bottom of the chamber are

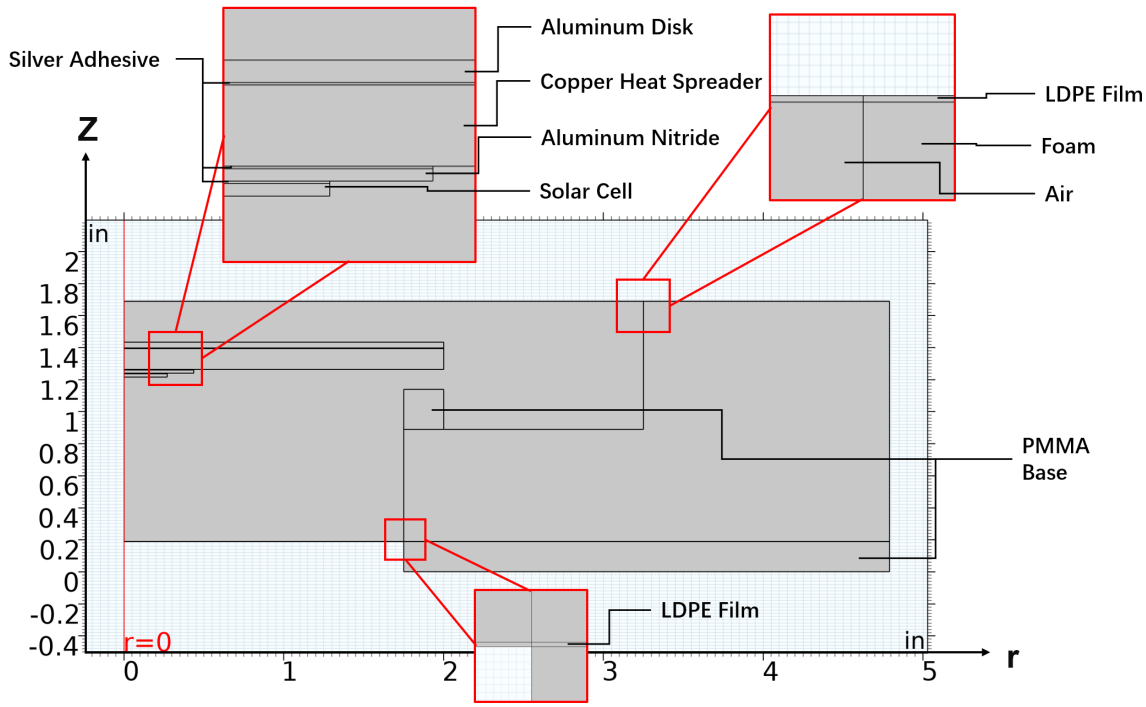

Fig. 4.2. The 2D geometry of chamber 2

also neglected, as they barely contribute to the total heat transfer and hard to be captured in a 2D geometry. The foam wall of the chamber is adjusted to a round structure, with a same averaged wall thickness as in real case. The Fresnel lens and PMMA frame elevating the chamber are neglected, since the heat has almost dissipated through the walls and thin films before conducted to them.

For both chambers. The corresponding component each domain represents are noted in Fig.4.2 and Fig.4.2. The zoomed-in figures on the up-left shows the configuration of the assembly disk in chamber 1 and 2, respectively. Specifically, the silver adhesive between aluminum disk, cooler, heat spreader, AlN and solar cell are defined as 0.1 mm thick layer. The LDPE films on top and bottom of the chambers are also defined, they can be seen in the zoomed figures on the up-right and bottom. A 3D plot showing the revolved 2D geometry is shown in Fig.4.3 as an auxiliary ref-

erence. In the result chapter, the temperature affected by each approximation will be discussed. It can be seen that these will not strongly impact the simulation result.

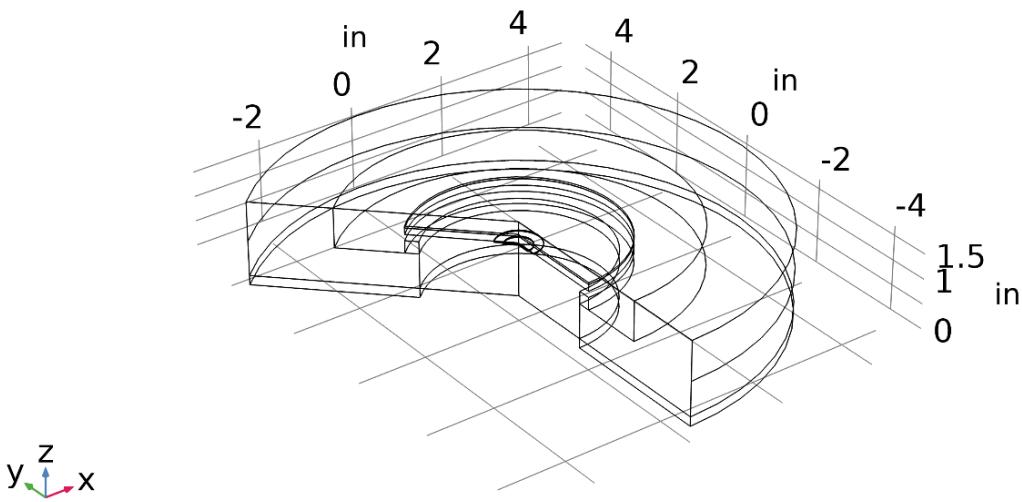

Fig. 4.3. The 3D geometry by revolving 2D geometry of chamber 2 along the axis of symmetry

4.2 Materials

After building the geometry, each domain must be assigned to a material in COMSOL with given heat capacity, density, thermal conductivity and surface emissivity as the basic parameters to solve thermal transfer equations. Specifically, for air domains, an extra data of dynamic viscosity is needed for calculating fluid dynamics. As mentioned earlier, the emissivity for each surface from 0.3 to 2.5 μm is measured by a spectrophotometer (Lambda 950, PerkinElmer), data above 2.5 μm is measured on an FTIR (Nexus 670). The data of heat capacity, density and thermal conductivity are extracted from various sources. For each purchased component, part of the data can be directly found on spec sheet provided by its manufacturer [66–72]. The data is then compared with online databases [73] to ensure it is in a reasonable range. For

the parameters not given by original manufacturers, the data is taken from a similar product made by other manufacturers [67, 68, 70] or other publications and online database [74–78]. Specifically, the data of air [74] is taken from Tsilingiris's work, under 1 atmosphere pressure, at a humidity of 45%, which reflects the real condition when the experiments were conducted. COMSOL also has a well-established built-in material database can be used as a good reference. By cross-comparison, the accuracy of the data can be guaranteed at our best. The source of data is given in Tab.4.1.

Table 4.1. Data Source for Simulation. J: Journal; D: Datasheet from manufacture; O: Online database; B: COMSOL built-in database; M: Measured with Lambda-950 and/or FTIR

Material	Heat Capacity	Thermal Conductivity	Density	Emissivity	Viscosity
Air	J [74]	J [74]	J [74]	-	J [74]
LDPE	D [66]	D [66]	D [66]	M	-
Polystyrene Foam	D [67]	D [68]	D [69]	M	-
Soda-lime Glass	D [70]	D [70]	D [70]	M	-
Aluminum 5052	O [75]	O [75]	O [75]	M	-
Copper	B	B	B	M	-
Aluminum Nitride	B	B	B	M	-
GaSb	O [76]	O [76]	O [76]	M	-
Acrylic	O [77]	O [77]	D [72]	M	-
Silver Adhesive	O [78]	D [71]	D [71]	M	-

4.3 Physics Model

Most of the physics modeling is based on solving partial differential equations (PDE). For a given problem, a set of underlying equations, material properties, and boundary conditions need to be defined and calculated. COMSOL provides a number of physics interfaces for different physics processes. Each interface is designed for solv-

ing one specific kind of physics problems. In case of radiative cooling simulation, the interfaces used are Heat Transfer, Laminar Flow and Surface-to-Surface Radiation.

A further set up in COMSOL is defining a Multiphysics Modeling, to let different physics interfaces communicate and share real-time data. Multiphysics Modeling can couple data from related physics interfaces and involve all physics processes, which requires a lot of computation power but can guarantee a reliable result.

Heat Transfer interface regards all defined geometries as solid, including any liquid and gas, such as air and water. Only conduction and convection heat transfer are considered in this physics interface. However, due to the nature of Heat Transfer interface, the convection can only be simplified by letting user to define a convection coefficient on the target surfaces, without considering real fluid dynamics. Whereas in real case, the air flow inside the chamber also affects the convection and needs to be considered. In addition, thermal radiation cannot be simulated in this interface either. Obviously, only using Heat Transfer physics interface is not enough to give a trustworthy result. Thus, two other interfaces were also used to cover almost all physics processes related to heat transfer.

Laminar Flow was used to calculate air flow within the chamber. Gravity was added to simulate the natural convection inside chamber. As air heated by the assembly disk, the density will reduce causing a driving force against gravity. Air surrounding the assembly disk will absorb heat and bring it to top, bottom LDPE films and chamber walls. This process can be computed by Laminar Flow interface, the real-time temperature data of air at different locations inside chamber is coupled from Heat Transfer.

Surface-to-Surface Radiation interface solves the last puzzle, thermal radiation. This interface calculates how much power is received and emitted on each surface by radiation. The temperature information of each surface is given by the coupled Heat Transfer interface. Emissivity of each surface in the geometry is defined by user.

4.3.1 Heat Transfer Interface

As previously discussed, the Heat Transfer interface covers the entire structure. All defined domains are included in the calculation. The thermal properties of each domain are given by defined material data. The initial values and boundary conditions are defined based on measured data.

The initial temperatures of both chambers are set to local ambient temperature as reported by weather station [79]. The boundary conditions can be split to two parts, the heat source boundaries and convection boundaries. Almost every surface of the setup is constantly absorbing direct or diffused solar irradiance from sun and sky as input heat source. On the other hand, the absorbed heat is conducted to the walls and LDPE films of the chamber and dissipated through convection, or emitted out to ambient by surfaces through thermal radiation. Since Heat Transfer interface only deals with conduction and convection, the absorbed solar irradiance on each surface is pre-calculated and defined as a boundary heat source at the corresponding surface. The emitted thermal radiation, on the contrary, depends on the surface temperature and view factor, hence it is impractical to manually calculate. Therefore, the thermal radiation power exchanges are not included in Heat Transfer interface. The heat loss through thermal radiation will be covered by Surface-to-Surface Radiation interface, which will be discussed later.

Define Heat Source Boundaries

The defined heat source for both chamber 1 and 2 are shown in Fig.4.4 and Fig.4.5. Each boundary is labeled for convenience. The heat inputs on all the boundary are caused by solar irradiance. The surfaces not tinted as blue indicate zero power input, the solar irradiance is neglected due to the low absorption or small view factor to sun and sky.

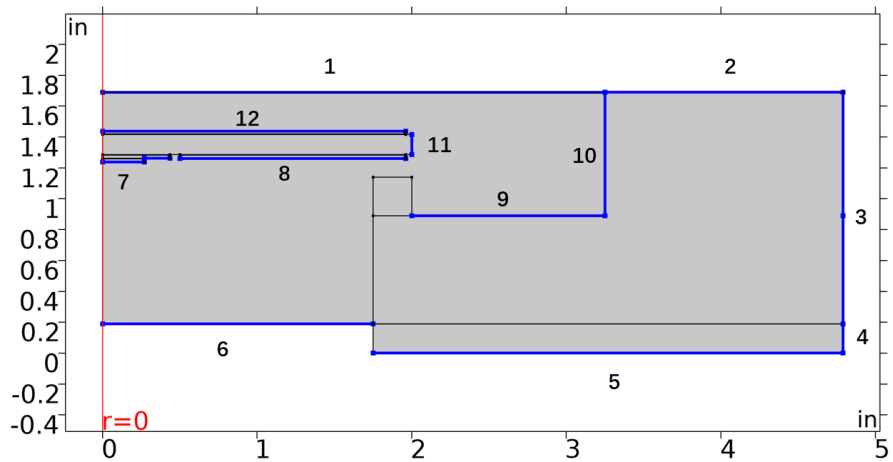

Fig. 4.4. The defined heat sources for chamber 1. Each blue line indicates one boundary heat source.

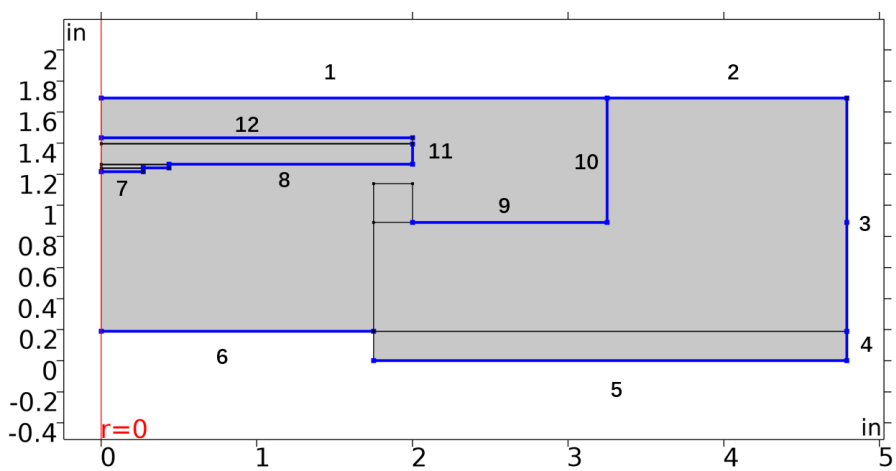

Fig. 4.5. The defined heat sources for chamber 2. Each blue line indicates one boundary heat source.

The absorbed solar irradiance P_s on each surface is calculated using Eq.4.1. Energy falls on each surface consists of three parts, direct solar irradiance, diffused solar irradiance and ground albedo, corresponding to the three terms in Eq.4.1.

$$
\begin{aligned}
P_s =& A_s \int_{-\infty}^{+\infty} d\lambda \cdot DNI\left(\lambda\right) \cdot \cos\left(\alpha\right) \cdot \varepsilon_s\left(\lambda\right) \cdot \tau_{tot}\left(\lambda\right) \cdot \rho_{tot}\left(\lambda\right) \\
&+ A_s \cdot F_s \int_{-\infty}^{+\infty} d\lambda \cdot DHI\left(\lambda\right) \cdot \varepsilon_s\left(\lambda\right) \cdot \tau_{tot}\left(\lambda\right) \cdot \rho_{tot}\left(\lambda\right) \\
&+ A_s \cdot F_g \cdot \rho_{albedo} \int_{-\infty}^{+\infty} d\lambda \cdot \left(DHI\left(\lambda\right) + DNI\left(\lambda\right)\right) \cdot \varepsilon_s\left(\lambda\right)
\end{aligned}
\tag{4.1}
$$

where ρ_{albedo} is the ground albedo, A_s is the surface area, $\tau_{tot}\left(\lambda\right)$ is the total transmittance of sunlight before it incidents on the surface, similarly, $\rho_{tot}\left(\lambda\right)$ is the total reflectance of sunlight before it incidents on the surface, $\tau_{tot}\left(\lambda\right)$ and $\rho_{tot}\left(\lambda\right)$ together account for the optical loss, F_s and F_g are the view factors from surface to sky and ground, respectively, α is incident angle of the sunlight, $DNI\left(\lambda\right)$ and $DHI\left(\lambda\right)$ are direct solar irradiance and diffuse horizontal solar irradiance of West Lafayette in August, under clear sky and 45% relative humidity. The spectrum data is extract from National Solar Radiation Database (NSRDB) but normalized according to the measured power by S314C thermal sensor. The ρ_{albedo}, $\tau_{tot}\left(\lambda\right)$, $\rho_{tot}\left(\lambda\right)$, α, F_s and F_g used for each surface are listed in Tab.4.2. The emittance of each surface is wavelength dependent, therefore is not shown in the table.

Table 4.2. Parameters for heat source

Surface	Material	A_s	τ_{tot}	ρ_{tot}	α	F_s	F_g	ρ_{albedo}
1	LDPE	0.0214	1	1	40 °	1	0	0
2	Al Sheet	0.025	1	1	40 °	1	0	0
3	Foam	0.0308	1	1	50 °	0.5	0.5	0.35
4	PMMA	0.0041	1	1	50 °	0.5	0.5	0.35
5	Al Sheet	0.0175	τ_{PMMA}	ρ_{mirror}	0 °	0.5	1	0.35
6	LDPE	-	-	-	-	-	-	-
7	GaSb	-	-	-	-	-	-	-
8	Al Coating	-	-	-	-	-	-	-
	Cooler							
9	Al Sheet	0.0133	$\tau_{LDPE} \cdot \tau_{lens}$	1	40 °	0.577	0	0
10	Foam	0.0034	$\tau_{LDPE} \cdot \tau_{lens}$	1	50 °	0.383	0	0
11	Copper	0.000356	$\tau_{LDPE} \cdot \tau_{lens}$	1	50 °	0.297	0	0
12	Al 5052	0.081	$\tau_{LDPE} \cdot \tau_{lens}$	1	40 °	0.955	0	0
	Cooler	0.078						

Here, the τ_{lens}, τ_{LDPE} and ρ_{mirror} are the wavelength dependent transmittance of Fresnel lens, LDPE film and reflectance of first-surface aluminum mirror, respectively, which are measured on Lambda 950 and FTIR as discussed before in the methodology chapter. For surfaces 6 to 8, the radiation is directly measured by the sensor therefore is not considered here. The sky view factors F_s for surfaces 9 to 12 are calculated by the software based on the defined geometry. The ground view factors F_g are assumed to be zero since the surfaces are enclosed inside the chamber. For surfaces 1 to 5, the F_s cannot be calculated directly as the tilt angle of the chamber constantly changes during the experiment. The view factors to sky for the top walls are taken as 1, and side walls are estimated to be roughly half, since the walls are approximately vertical. For side and bottom walls, namely, surface 3 to 5, the radiation from ground albedo is considered. The F_g is set to 0.5 for vertical surfaces 3 and 4, and 1 for surface 5, as it faces down to the ground during the experiment. The ground albedo is assumed to be 0.35 [80, 81], it is a mixed reflection from wood board, concrete ground and grass.

Other surfaces have almost zero view factor to the ground, hence the albedo and F_g is set to 0. The site condition is shown in Fig.4.6

Fig. 4.6. The surface albedo is a combination of reflection mostly from wood board, concrete, grass, and rock roads. The albedo of grass is typically ~ 0.26, the white concrete and rocks can be higher than 0.6. The estimated average albedo in simulation is 0.35.

For the convenience of simulation, the power on each surface is calculated first, and then normalized to the measured power by S314C thermal sensor. A ratio factor is defined by Eq.4.2, it uses measured power to divide calculated heat power.

$$Ratio\ Factor\ = \frac{P_s}{P_{sensor}} \tag{4.2}$$

In the software, input heat source power on each surface is given by multiplying a ratio factor as listed in Tab. 4.3 to the measured solar irradiance on thermal sensor. By relating the heat absorption on each surface to the measured solar irradiance, one can get the time dependent input power. This ensures the surface heat sources

can change accordingly to atmosphere conditions, such as clouds or mists, to improve simulation reliability. The factor can slightly change according to the solar irradiance, two sets of factors are used respectively for experiment 3 and 4, but only one is shown here.

All the above discussion for heat source boundaries aims at daytime experiment, namely, experiment 3 and 4. For experiment 2, because it was conducted at night, there was no solar radiation at all. Consequently, the boundary heat sources do not exist, no surface is added any heat source.

Table 4.3. Heat Source Ratio Factor, as defined in Eq.4.2

Surface	Material	Ratio Factor
1	LDPE	0.00641
2	Foam	0.50003
3	Foam	0.52427
4	PMMA	0.21782
5	Al Sheet	0.75695
6	LDPE	0.000459
7	GaSb	0.68897
8	Al Coating	0.062383
	Cooler	0.078979
9	Al Sheet	0.16545
10	Foam	0.17195
11	Copper	0.012359
12	Al 5052	0.15364
	Cooler	0.15204

Define Convection Boundaries

The defined convection boundaries for chamber 1 and 2 are shown in Fig.4.7 and Fig.4.8. Convection coefficient of each surface is calculated from a set of empirical equations[82] with given surface characteristic length, wind speed, air temperature and humidity, which are measured by local weather station [79].

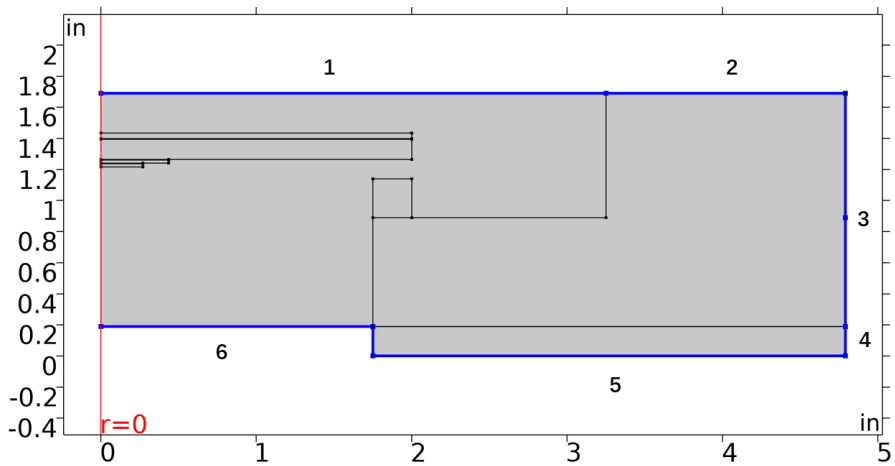

Fig. 4.7. The defined convection boundaries of chamber 1. Each blue line indicates one convection boundary.

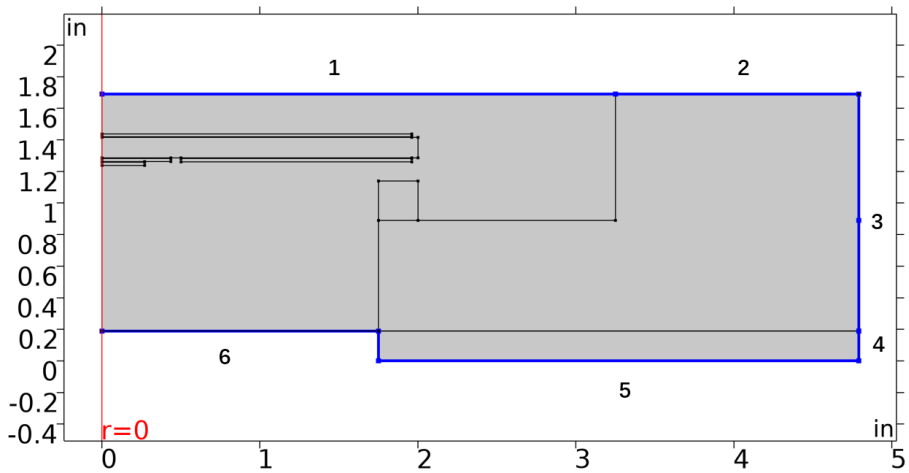

Fig. 4.8. The defined convection boundaries of chamber 2. Each blue line indicates one convection boundary.

The input convection parameters for each surface are shown in Tab.4.4. The wind speed at bottom surfaces are multiplied by a factor of 0.5 to account for the resistance from frame and adjacent chambers. The convection heat flux happens on the defined boundaries are calculated only based on the effective coefficient, the fluid flow process is not involved in order to reduce computational cost.

Table 4.4. Parameters of convection boundaries; wind speed factor is the reduction in wind-based convection associated with any intermediate layers.

Surface	Convection Type	Wind Speed Factor	Length [in]	Relative Humidity [%]
1	Forced, Horizontal Plate	1	9	45
2	Forced, Horizontal Plate	1	9	45
3	Natural, Vertical Wall	-	1.7	45
4	Natural, Vertical Wall	-	1.7	45
5	Forced, Horizontal Plate	0.5	9	45
6	Forced, Horizontal Plate	0.5	9	45

4.3.2 Laminar Flow Interface

The Laminar Flow interface calculates air flow inside chamber, shown as the tinted blue area in Fig.4.9.

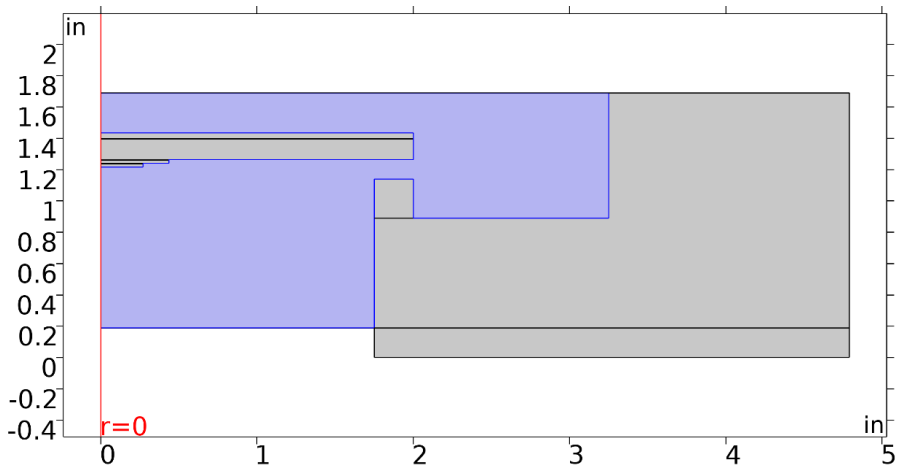

Fig. 4.9. Fluid dynamics is considered in the blue domain.

The initial values include air velocity and pressure. The initial velocity is defined as zero, since the temperature is the same everywhere at the beginning and air is stagnant. The initial pressure is set to 1 atmosphere. The boundary conditions, namely, the velocity of air in the immediate vicinity of a bounding surface, are set to be zero due to the viscosity of air.

4.3.3 Surface-to-surface Radiation Interface

The Surface-to-Surface Radiation module computes thermal radiation on defined surfaces. As shown in Fig.4.10 and Fig.4.11, the geometries are slightly modified to estimate the radiation exchange from Fresnel lens, neighboring chamber and surrounding buildings or trees, which are represented by surface 18, 15-16 and 17, respectively. They can affect the view factors of the up-facing surfaces thus need to be added. The view factors of all surfaces are considered in this module based on the defined geometry configurations, which means the interactions between the surfaces

are included. The areas where exposed to open space by default directly exchange heat with ambient through radiation. The ambient is regarded as a blackbody with a given temperature, each surface can be assigned to a unique ambient temperature to reflect the real circumstance.

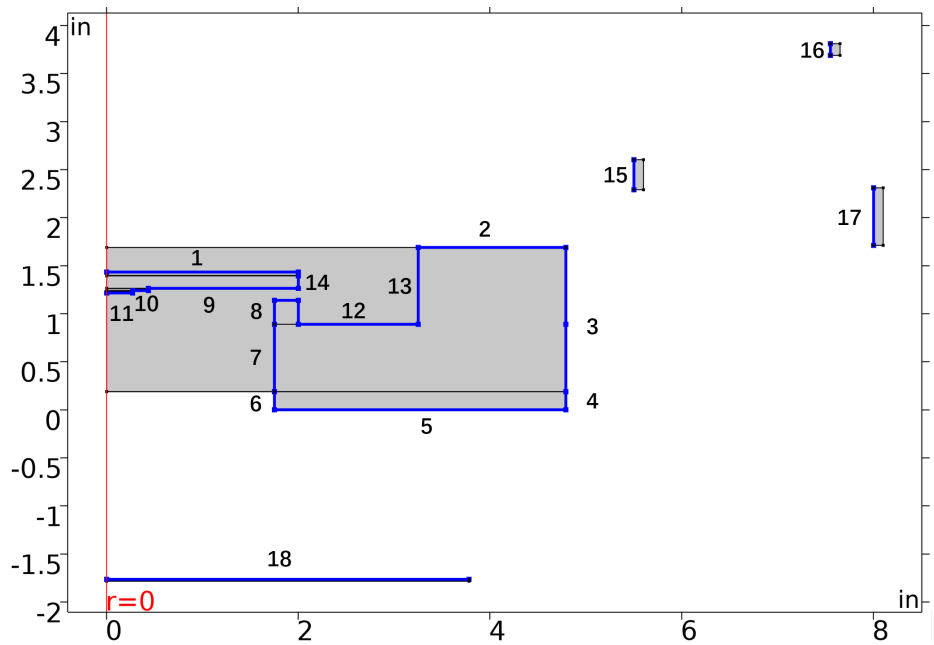

Fig. 4.10. The defined radiation surfaces of chamber 1. Each blue line indicates one radiation surface. The view factors are automatically calculated.

For surfaces 1, 12-14, the ambient temperature is defined as an effective temperature by solving $T_{sky(LDPE)}$ in Eq.4.3 [26]. The thermal radiation falls on these surfaces are caused by both LDPE film and sky emission transmitted LDPE film, there for is noted by $T_{sky(LDPE)}$.

$$\int d\lambda \cdot \left[\varepsilon_{LDPE}(\lambda) \cdot I_{BB}(\lambda, T_{LDPE}) + \bar{\varepsilon}_{sky}(\lambda) \cdot \tau_{LDPE} \cdot I_{BB}(\lambda, T_a)\right] = \int d\lambda \cdot I_{BB}\left(\lambda, T_{sky(LDPE)}\right) \tag{4.3}$$

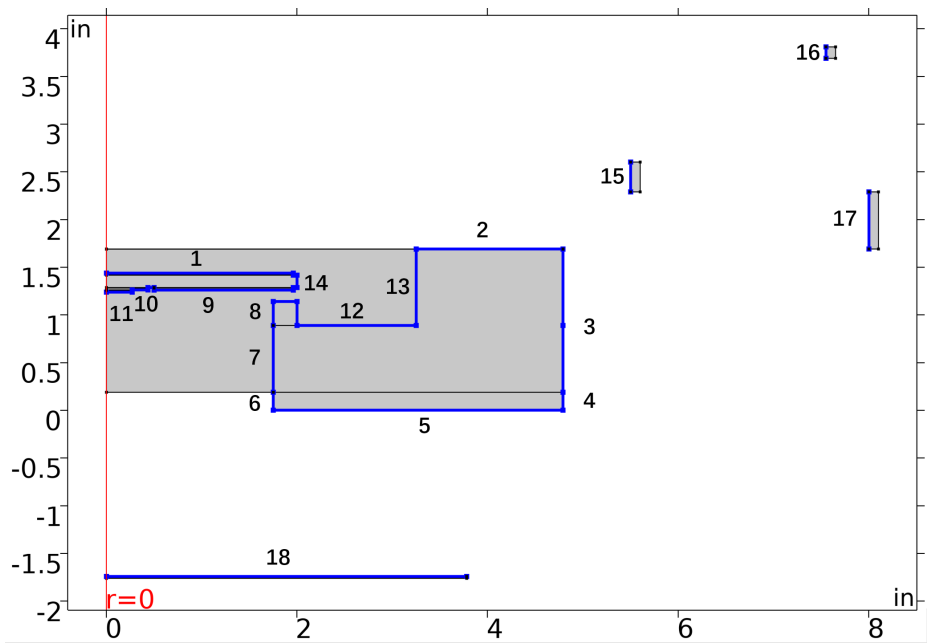

Fig. 4.11. The defined radiation surfaces of chamber 2. Each blue line indicates one radiation surface. The view factors are automatically calculated.

where $\varepsilon_{LDPE}(\lambda)$ and τ_{LDPE} are the emissivity and transmittance of LDPE film, T_{LDPE} is the steady state temperature of LDPE film, T_a is local ambient temperature, $\bar{\varepsilon}_{sky}(\lambda)$ is angular averaged sky emittance given by Eq.4.4

$$\begin{aligned} \bar{\varepsilon}_{sky}(\lambda) &= \frac{\int_{\Omega} d\Omega \cdot \varepsilon_{sky}(\lambda,\theta)}{\pi} = 2\int_0^{\frac{\pi}{2}} d\theta \cdot \varepsilon_{sky}(\lambda,\theta) \cdot \sin(\theta) \cdot \cos(\theta) \\ \varepsilon_{sky}(\lambda,\theta) &= 1 - \tau_{sky}(\lambda,0)^{\frac{1}{\cos\theta}} \end{aligned} \tag{4.4}$$

where $\varepsilon_{sky}(\lambda,\theta)$ is angular dependent sky emittance, $\tau_{sky}(\lambda,0)$ is normal sky transmittance extracted from MODTRAN mid-latitude summer sky [83], at 45% relative humidity.

The first term on the left in Eq.4.4 is the emission from LDPE, the second term is emission from sky transmitted to LDPE. Both are absorbed by the surfaces inside the chamber, which are surface 1, 12-14. Thus, a blackbody with a temperature of

$T_{sky(LDPE)}$ gives the same thermal radiation power to these surfaces, the $T_{sky(LDPE)}$ will be assigned to the software as ambient temperature for the corresponding surfaces.

For surfaces 2, 15-17, the irradiance is only from sky, thus, the effective ambient temperature is noted as T_{sky}, given by Eq.4.5. It is clear that the sky temperature T_{sky} is lower than ambient due to the small emissivity of sky, which makes radiative cooling a good cooling method for CPV.

$$\int_{-\infty}^{+\infty} d\lambda \cdot I_{BB}\left(\lambda, T_{sky}\right) = \int_{-\infty}^{+\infty} d\lambda \cdot \bar{\varepsilon}_{sky}\left(\lambda\right) \cdot I_{BB}\left(\lambda, T_a\right) \tag{4.5}$$

The ambient temperature of other surfaces is defined as T_a, which is the local ambient temperature. Again, the data is extract from weather station [79].

The emissivity of GaSb, AlN and Soda-lime glass cooler used in this module are the effective averaged emissivity calculated from Eq.4.6

$$\varepsilon_{eff}\left(T_s\right) = \frac{\int_{-\infty}^{+\infty} d\lambda \cdot \varepsilon_s\left(\lambda\right) \cdot I_{BB}\left(\lambda, T_s\right)}{\int_{-\infty}^{+\infty} d\lambda \cdot I_{BB}\left(\lambda, T_s\right)} \tag{4.6}$$

where the T_s is the surface temperature, λ is wavelength, $\varepsilon_s\left(\lambda\right)$ is the spectrum emissivity of the surface measured at room temperature, $I_{BB}\left(\lambda, T_s\right)$ is blackbody spectrum radiation at surface temperature. $\varepsilon_{eff}\left(T_s\right)$ give the temperature dependent average emissivity of the corresponding surfaces, which yields a more precise result.

Specifically, the emissivity of cooler $\varepsilon_{cooler}\left(\lambda\right)$ is the averaged emissivity of cooler over an angle θ from 0 °to 90 °, given by Eq.4.7. Here, $\varepsilon_{cooler}\left(\lambda, \theta\right)$ is measured on FTIR under different angles.

$$\varepsilon_{cooler}\left(\lambda\right) = \int_{0}^{\frac{\pi}{2}} d\theta \cdot \varepsilon_{cooler}\left(\lambda, \theta\right) \cdot \sin\left(\theta\right) \cdot \cos\left(\theta\right) \tag{4.7}$$

The emissivities of the rest of the surfaces are assumed to be independent with temperature and angle. The ambient temperature and emissivity assigned to each surface are shown in Tab.4.5.

It should be emphasized that for surfaces inside the chamber, namely, surface 1 and 7-14, part of the outgoing radiation will be reflected back by LDPE film and be re-absorbed by the surfaces inside chamber. The net going power is thus reduced. This effect can be treated as a dropping of emissivity, thus, by multiplying an average transmittance of LDPE film $\bar{\tau}_{LDPE}$ to the surface emissivity, one can account for the radiation reduction induced by LDPE film. The factor is defined as Eq.4.8.

$$\bar{\tau}_{LDPE} = \frac{\int_{-\infty}^{+\infty} d\lambda \cdot \tau_{LDPE} \cdot I_{BB}\left(\lambda, T_s\right)}{\int_{-\infty}^{+\infty} d\lambda \cdot I_{BB}\left(\lambda, T_s\right)} \tag{4.8}$$

Table 4.5. Parameters for Surface Radiation

Surface	Material	Emissivity	Ambient Temperature
1	Al 5052	$0.05 \times \bar{\tau}_{LDPE}$	$T_{sky(LDPE)}$
	Cooler	$\varepsilon_{eff(cooler)} \cdot \bar{\tau}_{LDPE}$	
2	Al Sheet	0.05	T_{sky}
3	Foam	0.9	T_a
4	PMMA	0.94	T_a
5	Al Sheet	0.05	T_a
6	PMMA	0.94	T_a
7	Foam	$0.9 \cdot \bar{\tau}_{LDPE}$	T_a
8	PMMA	$0.94 \cdot \bar{\tau}_{LDPE}$	T_a
9	Al Coated	$0.05 \times \bar{\tau}_{LDPE}$	T_a
	Cooler	$\varepsilon_{eff(cooler)} \cdot \bar{\tau}_{LDPE}$	
10	AlN	$\varepsilon_{eff(AlN)} \cdot \bar{\tau}_{LDPE}$	T_a
11	GaSb	$\varepsilon_{eff(GaSb)} \cdot \bar{\tau}_{LDPE}$	T_a
12	Al Sheet	$0.05 \times \bar{\tau}_{LDPE}$	$T_{sky(LDPE)}$
13	Foam	$0.9 \times \bar{\tau}_{LDPE}$	$T_{sky(LDPE)}$
14	Copper	$0.05 \times \bar{\tau}_{LDPE}$	$T_{sky(LDPE)}$
15	Foam	0.9	T_{sky}
16	S314C Coating	0.95	T_{sky}
17	Surroundings	1	T_{sky}

5. RESULT AND DISCUSSION

In this chapter, the simulation results are compared with experimental data. It can be seen that the simulation is capable of quantitatively evaluating the transient physics process in both chambers, the temperatures estimated by simulation show a relatively good consistency with real experiment. The cooling power of the coolers and Al disk in chamber 1 and 2 are analyzed and compared. The improvements of solar cell performance and lifetime brought by cooler temperature are also discussed. An extra simulation was carried out to test the ultimate cooling power and temperature drop using an ideal above-ambient cooler, with a zero emissivity in solar spectrum and unity emissivity elsewhere. The data can provide a better understanding of the potential for radiative cooling.

The errors caused by both experiment and simulation are quantitatively evaluated based on the accuracy datasheet of measuring devices. Other possible sources such as local wind speed, temperature, relative humidity, surface albedo, etc. which can bring uncertainties to simulation are also discussed, but finding a precise value of uncertainty can be very challenging. Therefore, the variation for these sources are not included in the simulation.

5.1 Accuracy of 2d Geometry Approximation

Considering the 2D geometry does not fully represent the original structure of the chambers, the effects on temperature caused by approximations need to be studied. Since solving the transient solution for an complicated 3D geometry can take days, it is unrealistic to check the temperature changes in this way. A more efficient method to verify the approximations is to solve a steady state solution, using an averaged constant input to replace the time dependent data, including solar irradiance, wind

speed and ambient temperature. Each data is taken the average of last 5 minutes, as the steady state conditions. This can still achieve the same goal but save a huge amount of time.

The defined 3D geometry for chamber 2 is shown in Fig.5.1. The holders and four Teflon cubes are taken off to reduce the computation, other components are defined with the size same as real configuration. The adjacent chamber and thermal sensor are simplified as two narrow walls, sit at the same position as real setup. The two walls server as radiation surfaces which block part of the view factor from chamber to sky. Similarly, the surrounding buildings and trees are replaced with a ring, the height and diameter are calculated such that the view factor from top of the chamber to the ring is roughly the same as real condition. Only chamber 2 is tested in both 2D and 3D modeling, because of its simpler configuration. The results could also be applied to predict the variations of chamber 1 due to the similar structure. A revolved 2D geometry are also shown in Fig.5.2 for comparison, the surroundings are represented by rings, which will slightly affect the view factor from cooler to sky. The solar cell and AlN base in 2D geometry are also simplified to thin disks, which have the same thickness and total volume as real case.

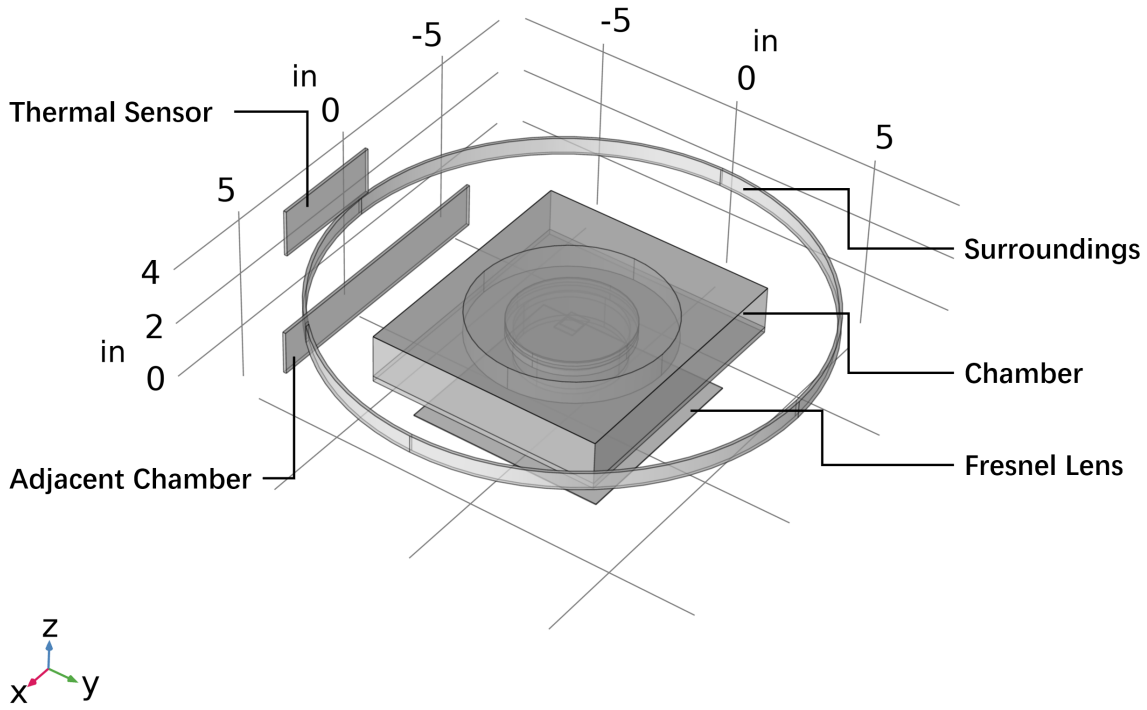

Fig. 5.1. The defined 3D geometry in COMSOL. The adjacent chamber, power sensor and surroundings are modeled as thin walls to account for the effects on radiative cooling. The chamber and components inside it are represented with real sizes.

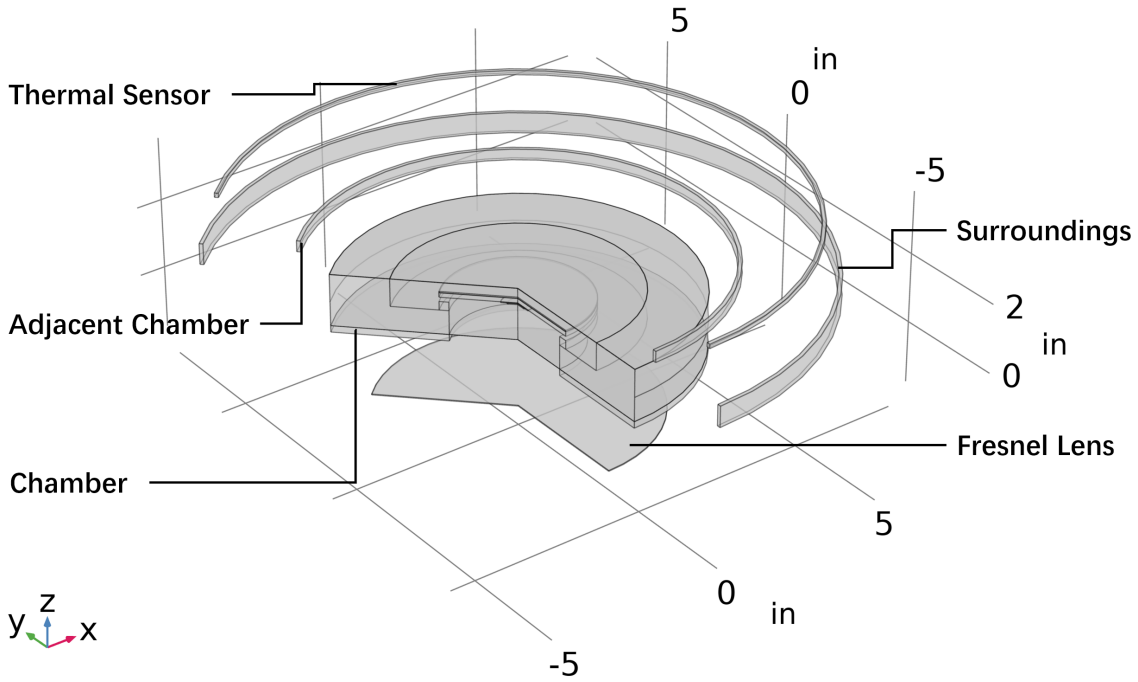

Fig. 5.2. The defined 2D geometry in COMSOL. The adjacent chamber, power sensor and surroundings are modeled as rings to account for the effects on radiative cooling. The chamber and components inside it are represented with effective disks with same thickness and volume as real size.

The steady-state solution for 2D and 3D structures of chamber 2 are shown in Fig.5.3. The temperature for each component is the averaged body temperature. As can be seen from the figure, the assembly disk exhibits a very small temperature variation from different component, indicating a good temperature uniformity, which also means heat from the cell can flow to coolers fluently. The largest temperature difference is less than 2 °C in 3D simulations between the solar cell and the aluminum disk, which are the most distant components of the assembly.

Other key parameters are listed in Tab.5.1, the net radiation and net heat flux are also averaged values of the corresponding surfaces. Net radiation of Al disk only accounts for the radiative heat transfer, the heat conduction and convection with

chamber air are not considered. Net heat flux of the chamber walls involves both convection and radiation. These values are compared because they are where changed the most from 3D to 2D structure. The side walls are rectangular in 3D structure but round in 2D, thus the net heat fluxes are specifically checked in the simulation to see if there is any discrepancy. It can also be seen from the results that most of the heat dissipation is from the top wall of the chamber, due to the convection of thin film. The side wall and bottom wall have a less contribution to the heat loss.

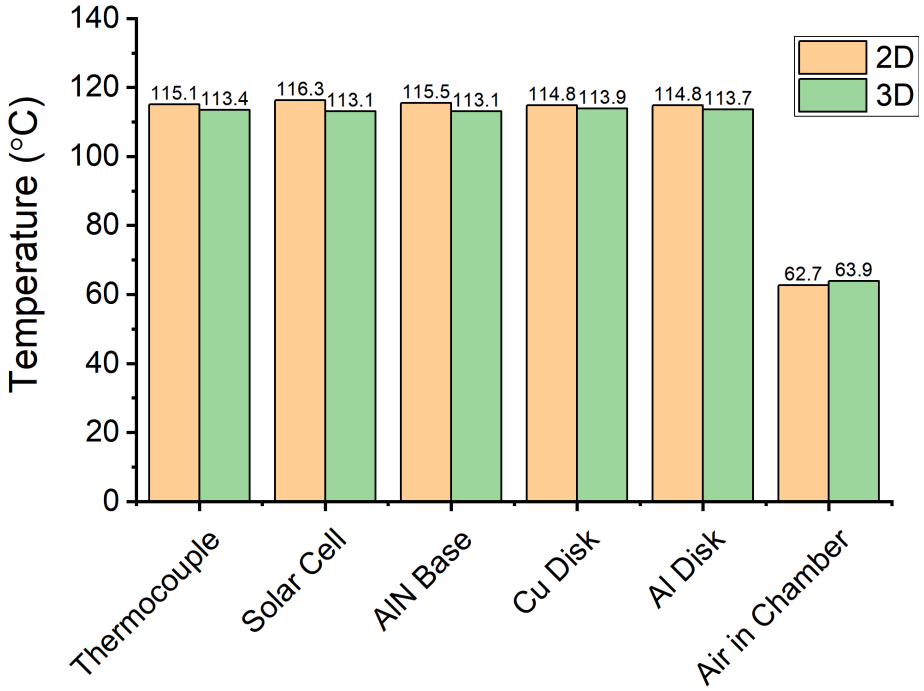

Fig. 5.3. Key steady-state temperatures for both 2D and 3D geometries. The temperature variations are well controlled. The temperature of thermocouple is taken from the mesh cell located near the real position of the thermocouple contacting point.

Table 5.1. Key steady-state solutions for both 2D and 3D geometries. The simulation results are compared side-by-side to study the variation caused by 2D geometry approximation. The largest discrepancy happens at side wall, with a 16% lower heat dissipation rate. This is due to the rectangle chamber in 3D geometry being simplified to a round chamber in 2D geometry. Nonetheless, the overall data still shows a good approximation

Solution	2D	3D
Total Heat Input $[W]$	16.51	16.51
Al (up) to Sky View Factor	0.955	0.973
Al (up) Net Radiation $[W/m^2]$	40.298	38.990
Al (down) Net Radiation $[W/m^2]$	30.302	28.550
Chamber Wall (up) Net Heat Flux $[W/m^2]$	137.290	132.649
Chamber Wall (down) Net Heat Flux $[W/m^2]$	30.686	28.119
Chamber Wall (side) Net Heat Flux $[W/m^2]$	16.675	20.031
Chamber Wall Total Net Heat Flux $[W/m^2]$	184.651	180.799

As can be seen from the result, most of the temperature differences are lower than 3 °C. The view factor from the aluminum disk to sky maintains almost the same, other data also varies in a very small range, indicating a good approximation. It should be noted that both results gave temperatures slightly higher than experimental data, this is caused by deactivating Laminar Flow module in the simulation. Therefore, the air inside chamber is considered as solid and does not have convection heat transfer. The heat exchange of the components inside chamber is thus reduced. Laminar flow was not carried out because the module is designed to calculate transient process, which makes it difficult to find the steady-state solution. The software cannot run successfully if Laminar Flow module is involved.

The other thing should be emphasized is that the results can be affected by the mesh configuration to some extent. The mesh cell properties such as aspect ratio,

skewness, orthogonality, and smoothness can affect the accuracy and computational cost. An example of auto-generated fine mesh and coarse mesh in the software is shown in Fig.5.4 and Fig.5.5.

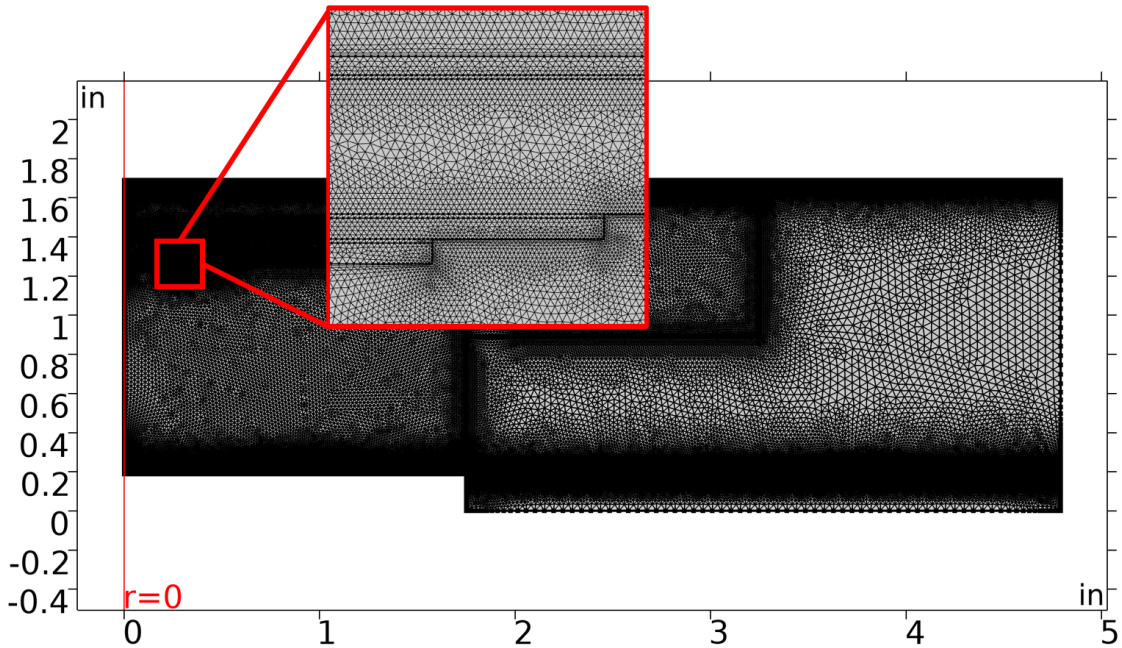

Fig. 5.4. An extremely fine mesh for chamber 1 generated in the software. The black areas are caused by the dense boundary lines, the imagine resolution is not enough to distinguish individual cells. Darker indicates a smaller mesh cell size.

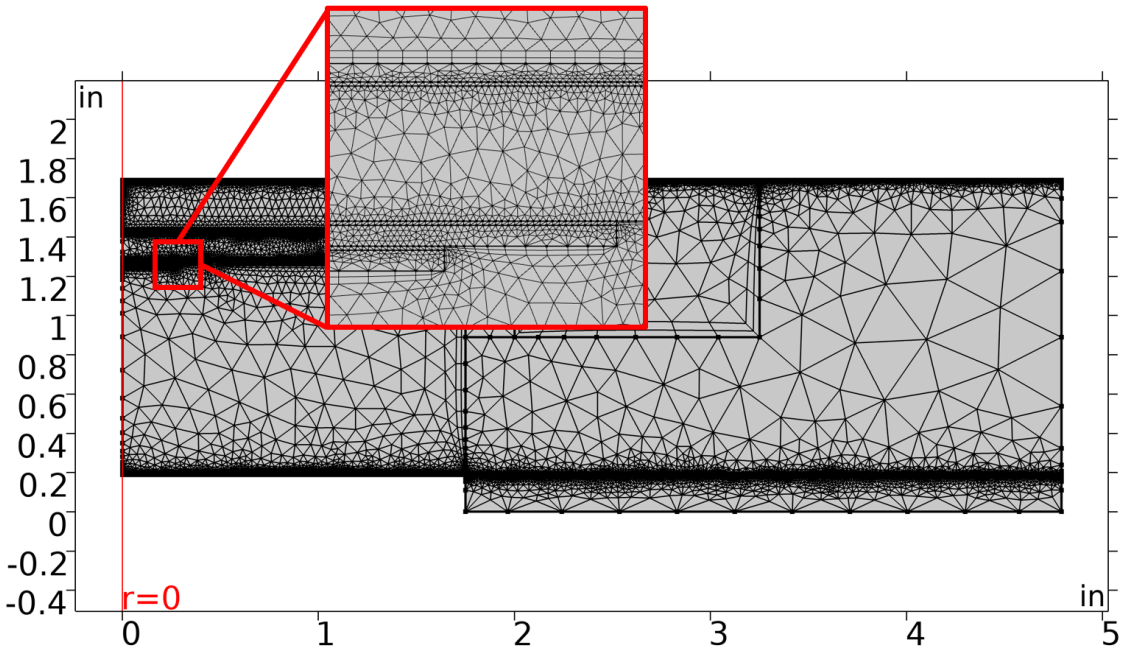

Fig. 5.5. An extremely coarse mesh for chamber 1 generated in the software. It can be seen the sizes of the mesh cells are much bigger than the first case. This can lead to a faster computation speed but a less accurate result.

Accuracy and speed are in tension. To get a better result, a finer mesh quality is usually needed, which will in turn reduce the speed. The size of the mesh depends on the accuracy requirements of the study. In this case, a relatively high quality mesh is used to ensure the precision of the result. A comparison showing the influences on temperature by meshing size is shown in Fig.5.6. The geometry, initial values, boundaries conditions and material properties are exactly the same for both cases, the only difference is mesh quality. It can be seen that as mesh becomes finer, the temperature gets higher and closer to experimental result, the largest temperature difference is around 2 °C. In the software, the size of the mesh can be further reduced to give a better estimate, however, due to the limitation of computational power, no finer mesh is used in the simulation. The simulation results already have a good match with the experiment data, and can be used to quantitatively interpret the physics of radiative cooling.

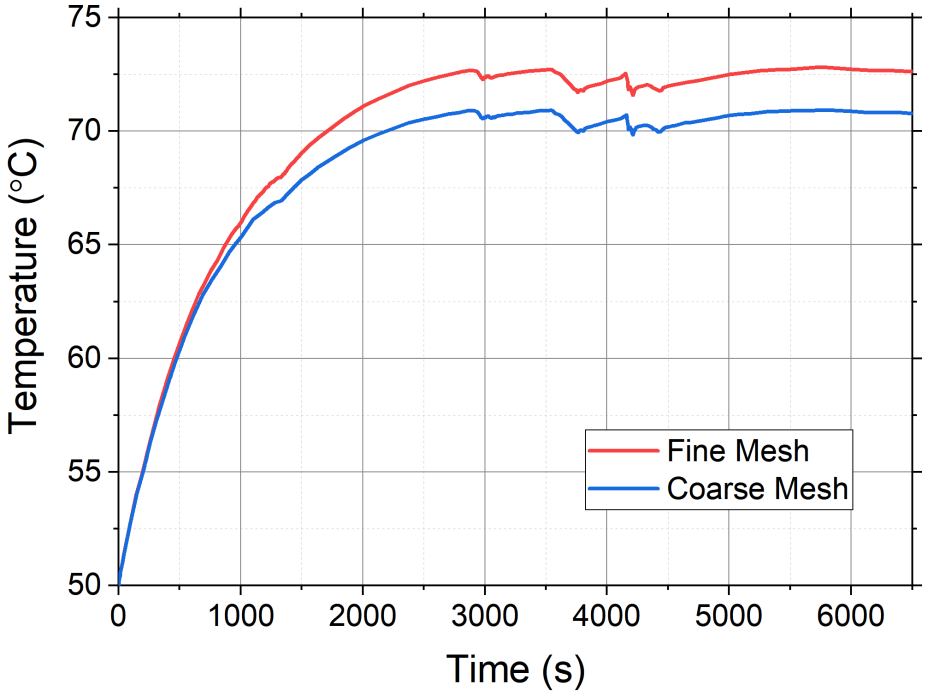

Fig. 5.6. An extremely coarse and extremely fine mesh are used to analyze the geometry. The simulated temperature of solar cell in both cases are plotted, the input data is extracted from experiment 4, on September 14th, 2019. The greatest temperature difference is roughly 2 °C.

In addition to the errors from simulation, equipment used in experiment also brings systematic errors. The accuracy of each measuring device used in the experiment is listed in Tab.5.2. Based on the datasheet from manufacturer [84–87], the combined temperature error for experiment data is around 5.74 °C. On the other hand, the error brought by S314C power sensor and PM100D meter console can be reflected in the simulation results. Thus, in the following figures in this chapter, if necessary, error bars are added for results from experiment to account for the possible range of temperature. Similarly, shaded areas are plotted for simulation results to account for the variance.

Table 5.2. Accuracy datasheet of S314C thermal sensor, PM100D meter console, DI-245 data collector and type-K thermocouple (TC)

Equipment	Accuracy
Type-K TC	± 2.2 [°C]
DI-245 (Type-K TC)	± 3.54 [°C]
DI-245 (Voltage)	$\pm 5.1 \times 10^{-4}$ [V]
S314C	± 5%
PM100D	± 1%

5.2 Experiment 2 Simulation Result

The simulation results for experiment 2 is shown is Fig.5.7 and Tab.5.3. Error bars are not added to the figure since they already show a good match. The thermal radiance of each surface listed in the table accounts for the net outgoing thermal radiation, and does not involve solar irradiance. The experiment was conducted during the night, achieved a 3 °C below ambient steady-state temperature. Based on the simulation result, the net cooling power from soda-lime glass cooler is around 22.3 W/m^2, whereas the power from aluminum disk is around 2.5 W/m^2. As discussed before in the introduction chapter, the greater radiation power is caused by the high emissivity of soda-lime glass in transmittance window. On the other hand, the aluminum disk almost does not emit thermal radiation, leading to a steady-state temperature close to ambient.

Interestingly, at steady-state, the cooler at bottom in chamber 1 keeps absorbing radiation from environment. This is because the cooler at bottom does not have access to sky, it faces objects such as Fresnel lens and ground, which has the same temperature as ambient. Consequently, due to the below-ambient temperature of the cooler, it absorbs heat from these surfaces. Whereas in chamber 2, the Al disk facing down can still have a negative net thermal radiation power even it is already ∼0.8

°C below ambient. In fact, in chamber 2, the chamber wall and PMMA ring become to the main sources for radiative cooling. The PMMA and foam have a emissivity greater than 0.9 in IR range, leading to a substantial cooling power. According to the simulation result, the temperature of the foam inside chamber is even lower than Al disk, leading to a negative radiation flux of the bottom Al.

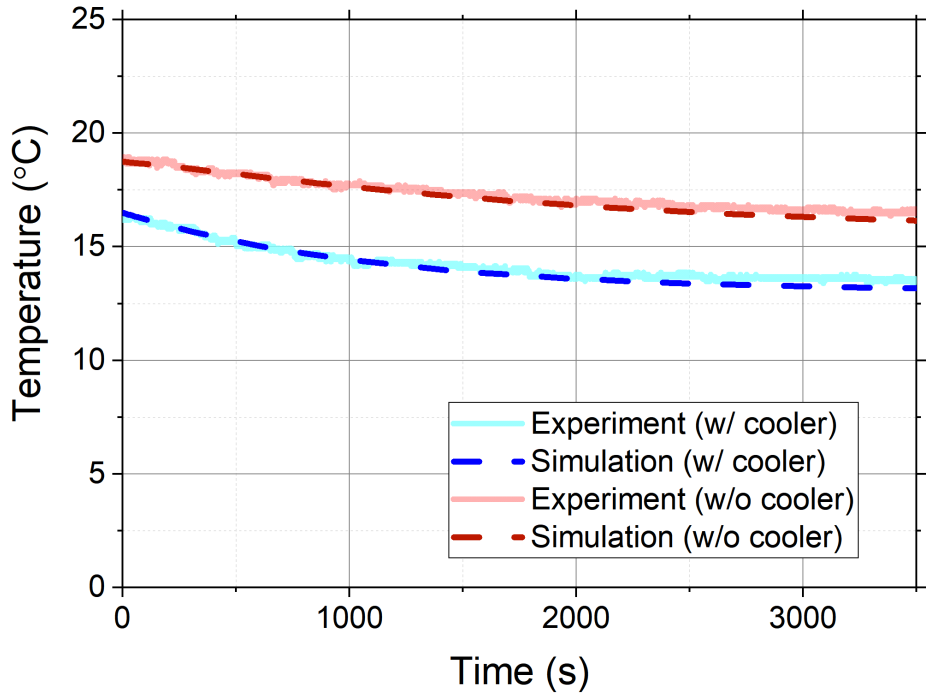

Fig. 5.7. The simulation result for experiment 2. Temperature from both experiment and simulation are shown as comparison. Error bars are not added due to the good match

Table 5.3. Simulation result for experiment 2. The positive value indicates incoming power and negative value indicates outgoing power from the surface. Cooler/Al (up) implies the up-facing cooler in chamber 1 and Al disk in chamber 2; similarly, Cooler/Al (down) implies the bottom cooler and Al coating

Steady-State Solution	Chamber 1	Chamber 2
Temperature of Solar Cell [°C]	13.180	16.153
Cooler/Al (up) Thermal Radiance [W/m^2]	-29.319	-2.485
Cooler/Al (down) Thermal Radiance [W/m^2]	7.091	-0.111
Cooler/Al Total Thermal Radiative Power [W]	-0.180	-0.02

5.3 Experiment 3 Simulation Result

The results of experiment 3 are shown in Fig.5.8. Error bars are added to indicate the uncertainty caused by Type-K thermocouple and DI245 data collector, the shaded areas account for the error caused by S314C and PM100D meter console. The experimental data and simulation results exhibit a very good match, suggests a credible analysis from the software. (The discrepancy of simulation for chamber 1 starting from 6100 s is due to the time-stepping error caused by software, which can be fixed by reducing the time step to a smaller value. The solver of the software does not calculated the data at each second, it will skip some data points where there is no huge fluctuation to save computational power. However, the cost of speed is accuracy, by skipping input data points the results can be off the track in some cases, like what is shown in Fig. 5.8. The solar power fluctuation in the last 2000 s was not captured by the solver, it still thinks the input power is the same as 6000 s, which is larger than real case. As a result of that, the calculated temperature is higher than experiment.)

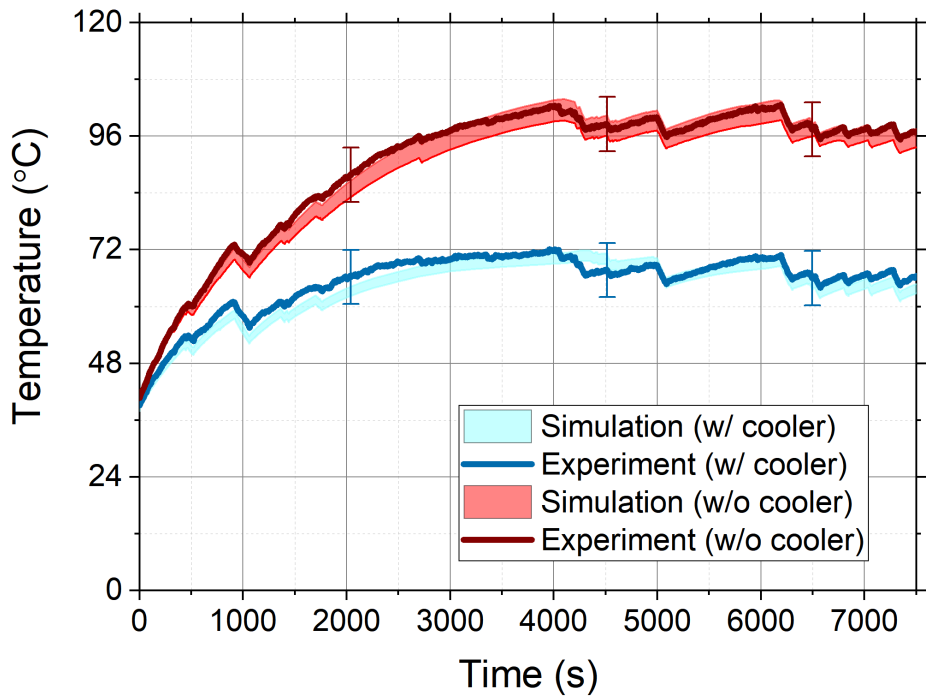

Fig. 5.8. The simulation result for experiment 3. Temperatures from both experiment and simulation are shown as comparison. Error bars account for the uncertainty caused by Type-K thermocouple and DI245 data collector, for readability, only three error bars are added to the graph. The shaded areas account for the simulation error caused by S314C and PM100D meter console.

A list of key results from simulation is shown in Tab.5.4. The thermal radiance of each surface listed in the table accounts for the net out going thermal radiation and does not involve solar irradiance. The total cooling power of the chamber wall covers the total outgoing power combined both thermal radiation and convection of the entire setup housing, again, the solar irradiance is not considered. The sum of last three terms is slightly higher than the total energy loss of the system, the reason is that part of the radiation from a surface inside the chamber can be reabsorbed by other surfaces.

The net cooling power of top soda-lime glass cooler and Al disk are $\sim$303 W/m^2 and $\sim$32 W/m^2, respectively. The power provided by cooler is almost a magnitude

higher than that from the Al disk; for the bottom cooler and Al coating, the cooling power from soda-lime cooler is still significantly higher than Al, resulting in a ∼31 °C temperature drop. Both the top and bottom cooler contribute a large amount cooling power, providing a total value of 3.572 W, whereas the Al surfaces only give a power of 0.446 W. Although the cooler facing down cannot use sky as cold heat sink and exchange heat, it is still able to dump waste heat to chamber walls, Fresnel lens and other objects with lower temperature. Obviously, when the operating temperature of CPV is substantially higher than ambient, it is still worthwhile to use radiative cooling even there is no open access to clear sky.

Table 5.4. Simulation result for experiment 3. The negative value indicates outgoing power from the surface. The data is taken at 6000 s of the simulation. Cooler/Al (up) implies the up-facing cooler in chamber 1 and Al disk in chamber 2; similarly, Cooler/Al (down) implies the bottom cooler and Al coating.

Steady-State Solution	Chamber 1	Chamber 2	Δ
Solar Cell Temperature [°C]	70.688	102.200	31.512
Cooler/Al(up) Thermal Radiance [W/m^2]	-302.954	-32.482	270.468
Cooler/Al(down) Thermal Radiance [W/m^2]	-167.115	-23.691	143.419
Cooler/Al Total Thermal Radiative Power [W]	-3.572	-0.446	3.126
Power Input on Assembly Disk	6.292	6.129	-0.163
Chamber Wall Total Cooling Power [W]	-17.090	-18.771	-1.681
Other Surfaces Total Thermal Radiative Power [W]	-3.389	-5.946	-2.557
Total Power Input [W]	22.136	22.033	-0.103

5.4 Experiment 4 Simulation Result

The results of experiment 4 are shown in Fig.5.9. Same as previous, error bars and shaded areas account for the uncertainties caused by measuring devices. The experimental data and simulation results match well, but not as good as experiment 3. The possible sources of error will be discussed in the last section of this chapter.

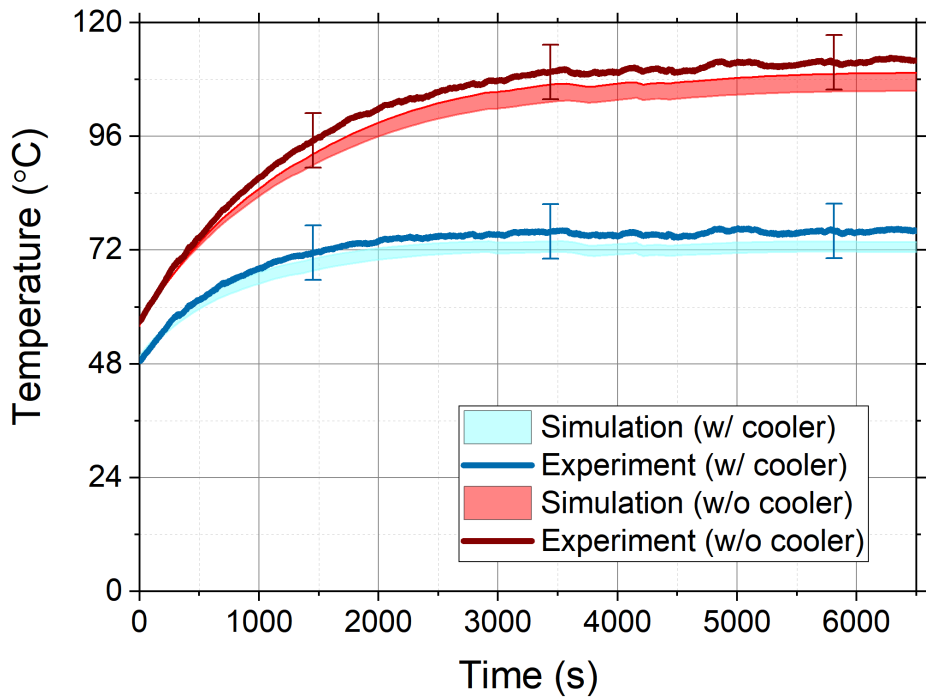

Fig. 5.9. The simulation result for experiment 4. Temperatures from both experiment and simulation are shown as comparison. Error bars account for the uncertainty caused by Type-K thermocouple and DI245 data collector, for readability, only three error bars are added to the graph. The shaded areas account for the simulation error caused by S314C and PM100D meter console.

A list of key results from simulation is shown in Tab.5.5. The results are similar as experiment 3, but having a larger difference between chamber 1 and 2. The cooling power of top soda-lime glass cooler and Al disk are ~310 W/m^2 and ~37 W/m^2, respectively, which are higher than experiment 3, due to the increased temperature.

The cooling power from cooler still overwhelms the Al disk. The temperature drop resulting from radiative cooling is as high as ∼36 °C. The total cooling power of the front and back coolers raised up to 3.642 W, meanwhile, the Al surfaces only provide 0.522 W.

Table 5.5. Simulation result for experiment 4. The negative value indicates outgoing power from the surface. The data is taken at 6500 s of the simulation. Cooler/Al (up) implies the up-facing cooler in chamber 1 and Al disk in chamber 2; similarly, Cooler/Al (down) implies the bottom cooler and Al coating

Steady-State Solution	Chamber 1	Chamber 2	Δ
Solar Cell Temperature [°C]	73.853	110.491	36.637
Cooler/Al(up) Thermal Radiance [W/m^2]	-309.513	-37.761	271.749
Cooler/Al(down) Thermal Radiance [W/m^2]	-169.565	-28.049	141.511
Cooler/Al Total Thermal Radiative Power [W]	-3.642	-0.522	3.120
Power Input on Assembly Disk	5.812	5.783	-0.029
Chamber Wall Total Cooling Power [W]	-14.495	-15.322	-0.827
Other Surfaces Total Thermal Radiative Power [W]	-3.831	-7.995	-4.164
Total Power Input [W]	20.549	20.454	-0.095

A set of 3D plots are also shown here for a more detailed information. The figure represents temperature distribution inside chamber is shown in Fig.5.10. The disk assembly has the highest temperature, with a uniform distribution. The air in close proximity to the disk also gets heated up, bringing the energy to the side walls of the chamber and LDPE films.

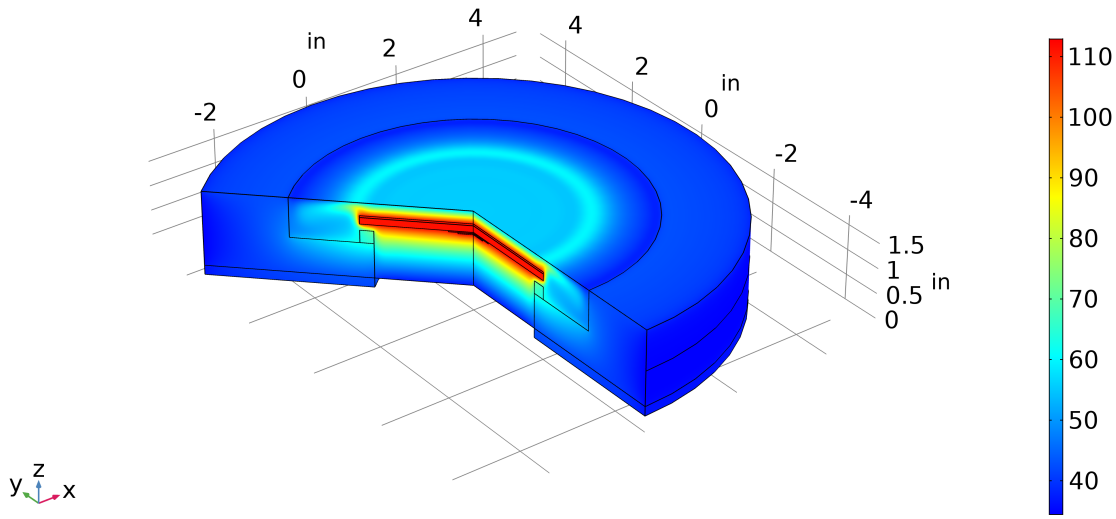

Fig. 5.10. A cross-section temperature profile of chamber 2.

Another plot in Fig.5.11 shows the flowing velocity of air inside chamber. The brighter areas indicate a greater speed. The air next to the disk circles around caused by natural convection, and dissipated heat to walls and LDPE films.

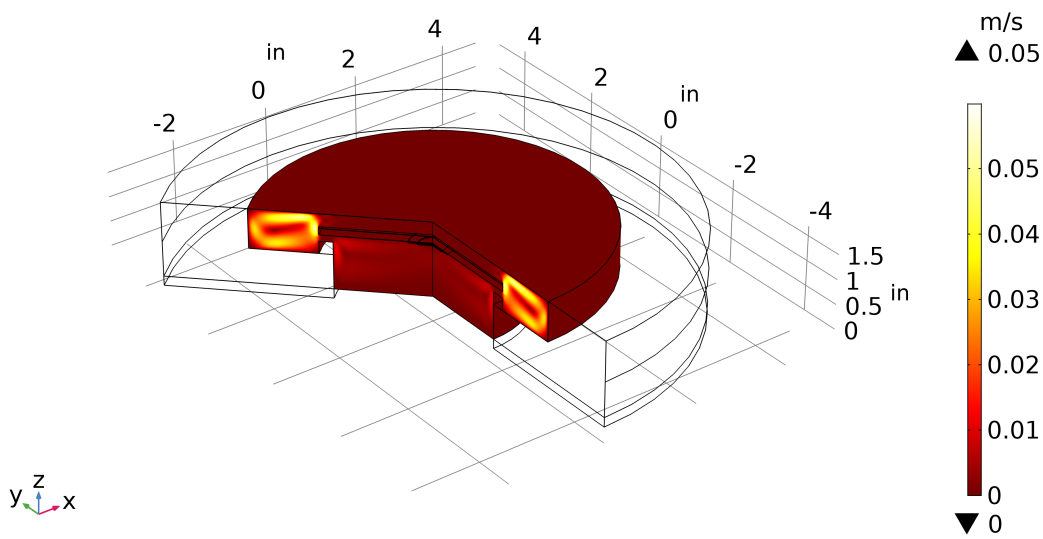

Fig. 5.11. A cross-section air velocity profile of chamber 2.

The heat flux field inside chamber is shown in Fig.5.12. Again, most of the heat is transferred to the top LDPE film by air insider chamber, due to the convection and conduction.

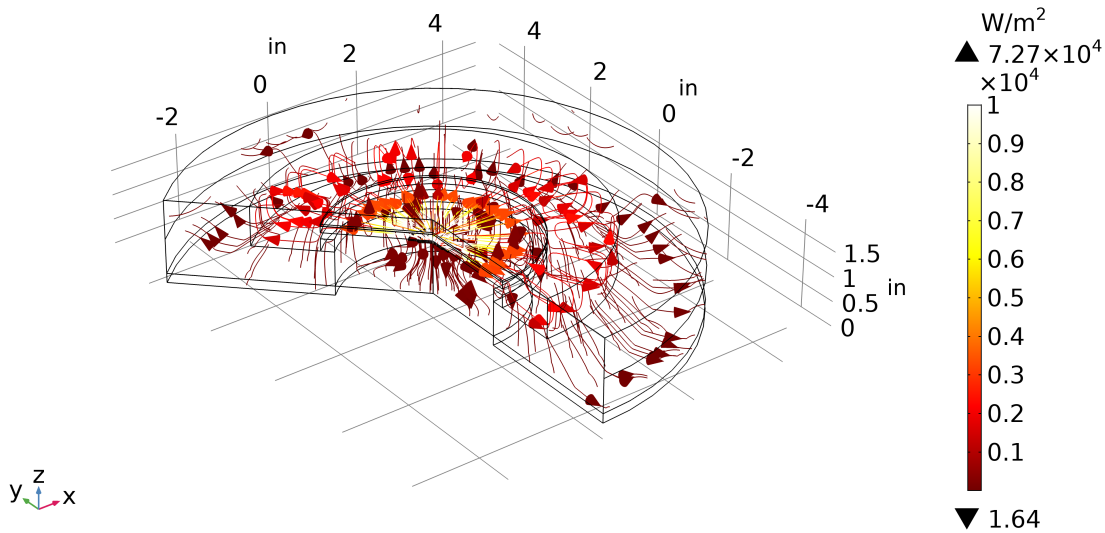

Fig. 5.12. A heat flux field profile of chamber 2. The brighter color indicates higher flux, the arrow indicates heat flow direction

5.5 Lifetime Improvement of Solar Cell

Solar cell module can degrade over time following the Arrhenius rate equation, as shown in Eq.5.1

$$k = Ae^{\frac{-E_a}{k_B T}}, \tag{5.1}$$

where A is an empirically-measured constant, E_a is the activation energy, and T is the temperature of the solar cell.

Depending on the material, type and fabrication quality of the solar cell module, the degradation rate can vary to a large extent. The activation energy E_a therefore can also change, but usually from 0.7 eV to 0.9 eV for most of the silicon solar cells [61]. The lifetime improvement can be estimated by comparing the degradation rate of

the solar cell working under temperature conditions in chamber 1 and 2, respectively. The result is shown in Fig.5.13. Although, the reported activation energy shown in the figure is from 0.49 to 0.85 eV [62–64], corresponding to a lifetime improvement ∼4 to 13 times longer, a wider range from 0.3 to 1.0 eV is calculated for reference. As can be seen, despite that the lifetime improvement can vary in a large range and hard to predicted accurately, the impact on lifetime brought by radiative cooling is significant.

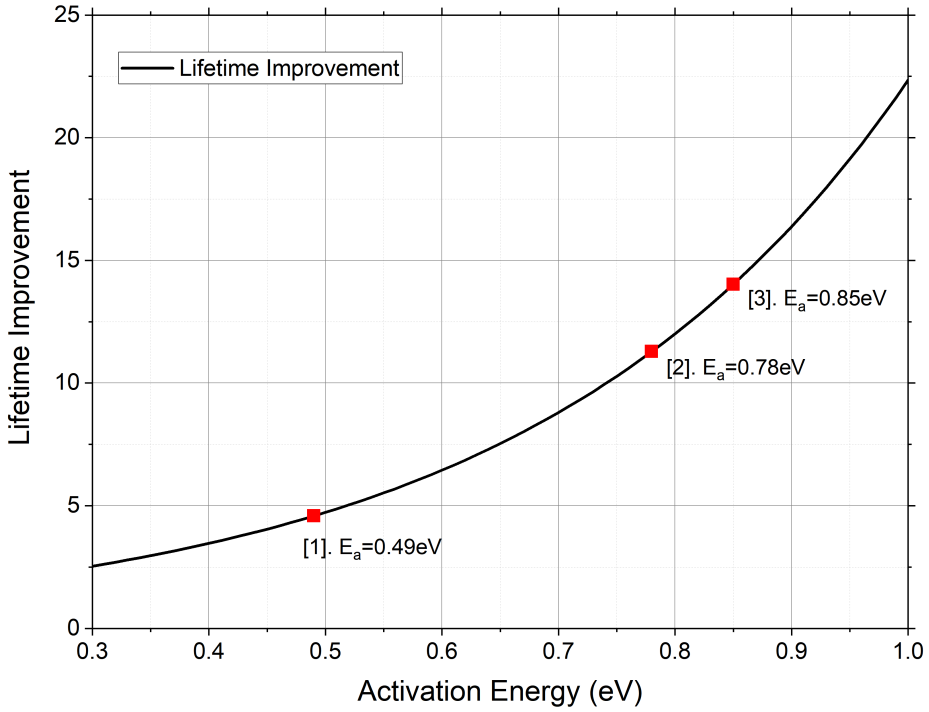

Fig. 5.13. An estimation of lifetime improvement of solar cell by applying radiative cooling. The temperatures used are 112 °C and 76 °C taken from the result of experiment 4. The three data points are activation energies taken from different references [62–64]. The range from 0.3 eV to 1 eV is covered in the figure, which can be applied to most of the solar cell types.

5.6 Ideal Emitter

Due to the reliable simulation results, it is trustworthy to use the model for case study. Here, an ideal emitter with unity IR emissivity and zero solar spectrum absorption is assumed to check the cooling performance. The weather and solar irradiance used is the same as the simulation of experiment 4. The result is compared with experimental data to estimate the potential improvement, as shown in Fig.5.14. Because of higher cooling power, the temperature dropped another ∼13 °C compared with chamber 1, yielding a total ∼ 50 °C temperature drop, compared with chamber 2. This result fully exploits the potential of radiative cooling, a well-designed cooler can significantly benefit a CPV system. The cooling power of each surface is also listed in Tab.5.6.

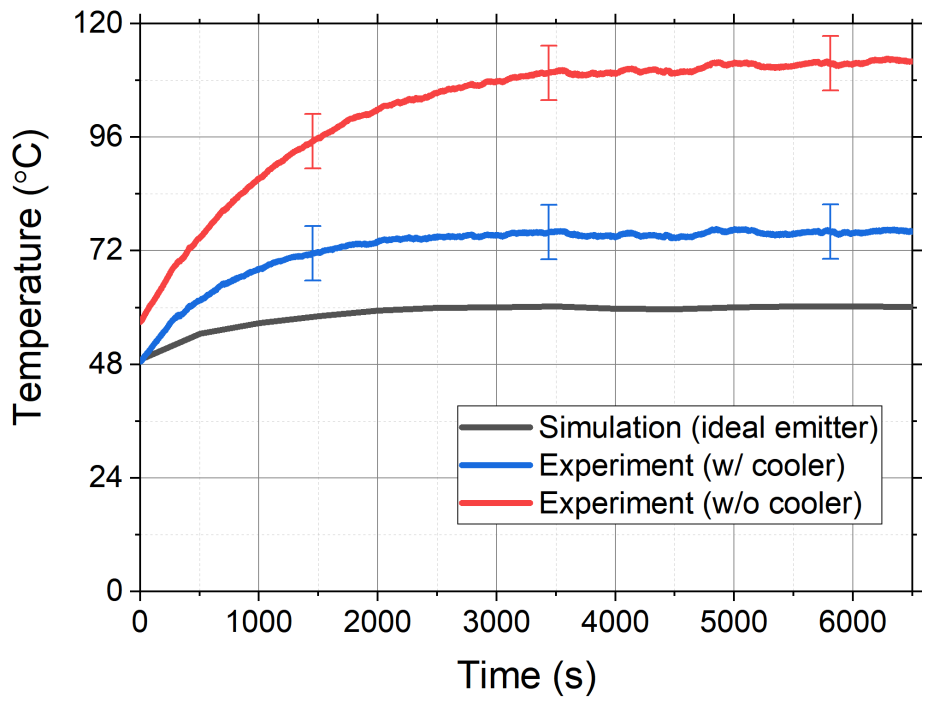

Fig. 5.14. A simulation result using an ideal above-ambient cooler. The weather data and solar irradiance is taken from experiment 4.

Table 5.6. The simulation result for ideal emitter, a further temperature drop of 12.5 °C can be achieved.

Steady-State Solution	Chamber 1	Chamber 2	Ideal Emitter
Solar Cell Temperature [°C]	73.853	110.49	61.276
Cooler/Al (up) Thermal Radiance [W/m^2]	-309.51	-37.761	-274.17
Cooler/Al (down) Thermal Radiance [W/m^2]	-169.56	-28.049	-122.91
Cooler/Al Total Thermal Radiative Power [W]	-3.642	-0.522	-3.0265
Chamber Wall Total Cooling Power [W]	-14.495	-15.322	-13.059
Other Surfaces Total Thermal Radiative Power [W]	-3.831	-7.995	-3.9709
Total Power Input [W]	20.549	20.454	19.175

5.7 Higher Concentration Factor

For practical high concentration PV systems (HCPV), the concentration factor can be much higher than the setup used in this work, which is estimated to be 39 suns. Therefore, it is worthwhile to investigate the radiative cooling performance at a higher concentration factor near real HCPV.

This can be easily tested by increasing the power source on solar cell to the corresponding value. Here in this simulation, the power is multiplied by a number of 2.5 based on the data measured from experiment 4, to represent a concentration factor of 100×. The result is shown in Fig.5.15. The cooling power of each surface is listed in Tab.5.7. As a result of higher heat load, the temperature difference boosts

to 53 °C. This is because the radiative cooling power increases to the fourth power of temperature, whereas for conduction and convection, they increase linearly. Thus, under higher temperature, radiative cooling can better perform. This also shows that radiative cooling is more resilient to temperature rise, as its cooling power can adapt to high temperature by the fast growing rate.

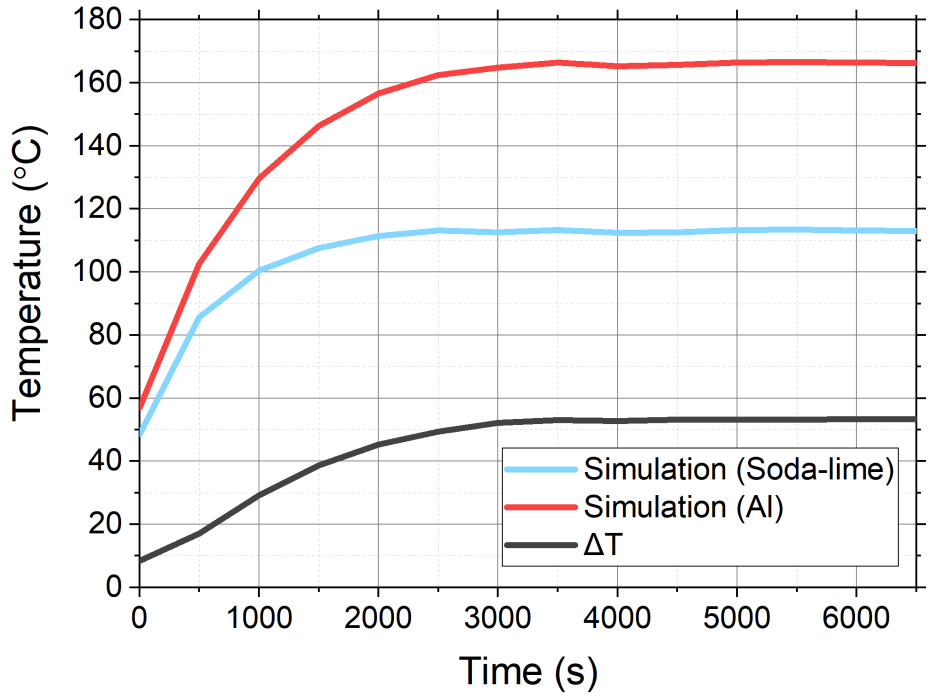

Fig. 5.15. A simulation result using 100× concentration factor. The weather data and solar irradiance is taken from experiment 4.

Table 5.7. The simulation result for the setup under 100 suns, a temperature drop of 53 °C can be achieved.

Steady-State Solution	Chamber 1	Chamber 2	Δ
Solar Cell Temperature [°C]	112.989	166.289	53.300
Cooler/Al(up) Thermal Radiance [W/m^2]	-602.988	-73.529	529.459
Cooler/Al(down) Thermal Radiance [W/m^2]	-396.690	-60.068	336.622
Cooler/Al Total Thermal Radiative Power [W]	-7.581	-1.060	6.521
Power Input on Assembly Disk	12.399	12.304	-0.095
Chamber Wall Total Cooling Power [W]	-16.298	-22.251	-5.953
Other Surfaces Total Thermal Radiative Power [W]	-4.196	-8.780	-4.584
Total Power Input [W]	27.178	27.083	-0.095

5.8 Possible Sources of Errors

The simulation result of experiment 3 matches well with experimental data, however, the simulation for experiment 4 is slightly off, but still within range of error bars. The geometry, mesh, material, physics module, etc. used in both cases are exactly the same. Only the input data of solar irradiance, wind speed and ambient temperature are changed. The errors may lie in these variables.

5.8.1 Setup Alignment

First, during the transportation of the setup, vibration may cause a slight change of relative position of each component. Thus, at the beginning of each experiment, the setup needs to be re-aligned, including the adjustment of tilt angle and height of each individual chamber; the position of Fresnel lenses and mirrors; the height and tile angle of the wood board. This can lead to a small variation of the concentration ratio for each experiment, hence, the measured solar irradiance can vary each time due to the alignment.

5.8.2 Local Weather Conditions

The extracted weather data is not able to fully reflect the local conditions, especially the wind speed. It can vary to a large extent depending on the topography. Unfortunately, the wind speed can greatly affect the convection coefficient, based on the simulation model, a raise of wind speed from 10 km/h to 20 km/h can increase the convection coefficient from 13.44 to 19.01 $W/m^2/K$, inducing a 41 % more heat exchange rate. This can lead to a power fluctuation of $\sim$5 W. In addition, the atmosphere circumstance in West Lafayette could be different from MODETRAN's data. This can lead to an uncertainty of sky temperature, which will further influence the radiative cooling power.

5.8.3 Uncaptured Power Input

During the experiment, the thermocouple probe can expose to part of the incoming solar irradiance, the radiation power is affected by the alignment quality, but usually is a very small value. However, this can still lead to a certain raise of the local temperature, the probe may have a higher temperature than the contact surface. The surface albedo is also likely to bring error to the system. As it is very hard to

measure the surface albedo of the outdoor field where the experiment conducted, the data is estimated based on online references, which can result in uncertainties.

5.8.4 Simplified Geometry

As discussed before, the geometry used in simulation is simplified and may affect the accuracy. Moreover, in real situation, the surface contacts of each component are not perfectly aligned. Air holes between surfaces can cause thermal resistance and reduce heat conduction rate, resulting in a higher steady-state temperature. Since the total outgoing power is mostly limited by the convection coefficient, the influence from contact thermal resistance is usually very small, but it still exists.

5.8.5 Material Data

Part of the material data such as thermal conductivity, heat capacity and density is extracted from publications and online databases, which may not be able reflect the real properties of the material. The thermal conductivity can affect the steady-state temperature to a certain degree. The IR emissivity of PS foam, PMMA, Al can also bring errors to the thermal radiation power, affecting the temperature.

5.8.6 Software Algorithms

It has been well illustrated that mesh size can have an impact on simulation results, the temperatures are usually higher if given a finer mesh. In order to get the results within an acceptable calculation time, the mesh size used was not the smallest. This could be the reason of a lower estimated temperature from the simulation. Similarly, the time step between each calculation can be shorter to give a more precise result.

6. SUMMARY AND FUTURE WORKS

In this work, the potential and limitations of CPV systems are first discussed. The concentrated solar illumination is the key advantage of CPV, as it can push the cell to a higher open-circuit voltage and improve the efficiency. However, the greater power input can also elevate the operating temperature of the solar cell and negatively affect efficiency and lifetime. Therefore, thermal management is needed for enhancing the overall performance of CPV.

Among the various cooling techniques, radiative cooling, as a compact and passive cooling method, is one of the most promising one for CPV, since its cooling power increases much more rapidly with temperature than most other cooling methods (e.g., conduction or convection). This means that radiative cooling has potential to offer both high total cooling power and high specific cooling power (per unit weight). Therefore, to have a better understanding of radiative cooling, the principle, materials and development of radiative cooling is then introduced.

To verify the cooling performance, a special designed CPV setup is built and tested. The structures and key parameters of the setup are discussed in detail. A soda-lime glass coated with 300 nm Al at back surface is used as raditive cooler in chamber 1 of the setup, whereas in chamber 2, an Al disk is used as a comparison. Four outdoor experiments were conducted under different weather conditions to study the effect of radiative cooling on CPV. A temperature drop of 36 °C was achieved at steady-state, leading to a 0.08 V increase of open-circuit voltage. This temperature decreasing can extend the lifetime of solar cell $\sim$ 4 to 13 times longer (5 to 14 times in total). This temperature drop is comparable to prior experiment in below-ambient cooling, but does not require a vacuum chamber to operate [33]. It also appears to be the largest reported temperature drop in atmospheric-pressure conditions.

Three individual simulations were carried out to quantitatively study the radiative cooling performance for experiment 2 to 4. The data shows a good match with experimental results, implying a reliable analysis of the physics. The cooling power of each experiment is estimated, the power provided by cooler is almost 10 times as the power emitted from Al disk.

Other two simulations were also performed to study the full potential of radiative cooling in the same CPV structure. A total temperature drop of ∼50 °C is estimated using an ideal cooler, corresponding to a ∼4 to 90 times lifetime of CPV, based on the data from [60–64], showing the possibility of further improvement using a refined cooler. Another simulation shows a greater temperature drop of ∼53 °C can be achieved using a 100 × concentration factor CPV, showing the greater performance of radiative cooling under high temperature. While of course all other things being equal, increased radiative cooler area is helpful, factors such as heat spreading, access to sky, and reduced convection that could limit the maximum performance.

Future experiments can be conducted with a near ideal above-ambient cooler to verify the performance. The structure of the setup can be further optimized to reach a higher cooling power, such as increasing the size of the cooler and heat spreader. A higher concentration factor that closer to a practical CPV can be further investigated, according to the promising result from simulation. The temperature-dependent efficiency, output power, lifetime, etc. of GaSb can be measured further. The setup is also a very good platform to test the benefits of cooling in other solar cells such as silicon-based PV or multi-junction PV. In particular, measuring the efficiency improvement of a high-performance multi-junction PV cells could be an interesting topic, as they are widely used in CPV systems.

REFERENCE

[1] *International Renewable Energy Agency (IRENA)*. URL: https://irena.org/.

[2] *Study: Levelized Cost of Electricity - Renewable Energy Technologies - Fraunhofer ISE*. Mar. 2019. URL: https://www.ise.fraunhofer.de/en/publications/studies/cost-of-electricity.html.

[3] P. T. Landsberg and G. Tonge. "Thermodynamic energy conversion efficiencies". In: *Journal of Applied Physics* 51.7 (1980). DOI: 10.1063/1.328187.

[4] William Shockley and Hans J. Queisser. "Detailed Balance Limit of Efficiency of p-n Junction Solar Cells". In: *Journal of Applied Physics* 32.3 (1961), pp. 510–519. DOI: 10.1063/1.1736034.

[5] Martin A. Green, Yoshihiro Hishikawa, Ewan D. Dunlop, Dean H. Levi, Jochen Hohl-Ebinger, and Anita W.Y. Ho-Baillie. "Solar cell efficiency tables (version 52)". In: *Progress in Photovoltaics: Research and Applications* 26.7 (July 2018), pp. 427–436. ISSN: 10627995. DOI: 10.1002/pip.3040.

[6] *Best Research-Cell Efficiency Chart*. URL: https://www.nrel.gov/pv/cell-efficiency.html.

[7] A De Vos. "Detailed balance limit of the efficiency of tandem solar cells". In: *Journal of Physics D: Applied Physics* 13.5 (1980), pp. 839–846. DOI: 10.1088/0022-3727/13/5/018.

[8] Prrez-Higueras Pedro and Fernnndez Eduardo F. *High concentrator photovoltaics: fundamentals, engineering and power plants*. Springer, 2016.

[9] G. Bunea, Wilson, and Ceuster. URL: https://www.pveducation.org/pvcdrom/solar-cell-operation/effect-of-light-intensity.

[10] *5.2. Light concentration effect on PV performance and efficiency.* URL: https://www.e-education.psu.edu/eme812/node/538.

[11] Swapnil Dubey, Jatin Narotam Sarvaiya, and Bharath Seshadri. "Temperature Dependent Photovoltaic (PV) Efficiency and Its Effect on PV Production in the World – A Review". In: *Energy Procedia* 33 (2013), pp. 311–321. DOI: 10.1016/j.egypro.2013.05.072.

[12] G. Bunea, Wilson, and Ceuster. URL: https://www.pveducation.org/pvcdrom/solar-cell-operation/effect-of-temperature.

[13] Xingshu Sun, Timothy J. Silverman, Zhiguang Zhou, Mohammad Ryyan Khan, Peter Bermel, and Muhammad Ashraful Alam. "Optics-Based Approach to Thermal Management of Photovoltaics: Selective-Spectral and Radiative Cooling". In: *IEEE Journal of Photovoltaics* 7.2 (2017), pp. 566–574. DOI: 10.1109/jphotov.2016.2646062.

[14] Yu Han, Steffen Meyer, Yasmina Dkhissi, Karl Weber, Jennifer M. Pringle, Udo Bach, Leone Spiccia, and Yi-Bing Cheng. "Degradation observations of encapsulated planar CH3NH3PbI3 perovskite solar cells at high temperatures and humidity". In: *Journal of Materials Chemistry A* 3.15 (2015), pp. 8139–8147. DOI: 10.1039/c5ta00358j.

[15] P. Espinet-González, C. Algora, N. Núñez, V. Orlando, M. Vázquez, J. Bautista, and K. Araki. "Temperature accelerated life test on commercial concentrator III-V triple-junction solar cells and reliability analysis as a function of the operating temperature". In: *Progress in Photovoltaics: Research and Applications* 23.5 (Dec. 2014), pp. 559–569. DOI: 10.1002/pip.2461.

[16] John R. Howell and Robert Siegel. *Thermal radiation heat transfer*. Taylor et Francis, 2002.

[17] Sundaram Anandan and Velraj Ramalingam. "Thermal management of electronics: A review of literature". In: *Thermal Science* 12.2 (2008), pp. 5–26. DOI: 10.2298/tsci0802005a.

[18] L.a. Florio and A. Harnoy. "Combination technique for improving natural convection cooling in electronics". In: *International Journal of Thermal Sciences* 46.1 (2007), pp. 76–92. DOI: 10.1016/j.ijthermalsci.2006.03.007.

[19] Karam M. Al-Obaidi, Mazran Ismail, and Abdul Malek Abdul Rahman. "Passive cooling techniques through reflective and radiative roofs in tropical houses in Southeast Asia: A literature review". In: *Frontiers of Architectural Research* 3.3 (2014), pp. 283–297. DOI: 10.1016/j.foar.2014.06.002.

[20] Dengfeng Du, Jo Darkwa, and Georgios Kokogiannakis. "Thermal management systems for Photovoltaics (PV) installations: A critical review". In: *Solar Energy* 97 (2013), pp. 238–254. DOI: 10.1016/j.solener.2013.08.018.

[21] Stephen Blundell and Katherine M. Blundell. *Concepts in thermal physics*. Oxford University Press, 2018.

[22] D. J. Fixsen. "The Temperature Of The Cosmic Microwave Background". In: *The Astrophysical Journal* 707.2 (2009), pp. 916–920. DOI: 10.1088/0004-637x/707/2/916.

[23] *IR Transmission Spectra*. Oct. 2012. URL: http://www.gemini.edu/sciops/telescopes-and-sites/observing-condition-constraints/ir-transmission-spectra#Mid-IR.

[24] Iryna E. Khodasevych, Liping Wang, Arnan Mitchell, and Gary Rosengarten. "Micro- and Nanostructured Surfaces for Selective Solar Absorption". In: *Advanced Optical Materials* 3.7 (May 2015), pp. 852–881. DOI: 10.1002/adom.201500063.

[25] Zhen Chen, Linxiao Zhu, Aaswath Raman, and Shanhui Fan. "Radiative cooling to deep sub-freezing temperatures through a 24-h day–night cycle". In: *Nature Communications* 7.1 (2016). DOI: 10.1038/ncomms13729.

[26] C. G. Granqvist and A. Hjortsberg. "Radiative cooling to low temperatures: General considerations and application to selectively emitting SiO films". In: *Journal of Applied Physics* 52.6 (1981), pp. 4205–4220. DOI: 10.1063/1.329270.

[27] Md. Muntasir Hossain and Min Gu. "Radiative Cooling: Principles, Progress, and Potentials". In: *Advanced Science* 3.7 (Apr. 2016), p. 1500360. DOI: 10.1002/advs.201500360.

[28] Eden Rephaeli, Aaswath Raman, and Shanhui Fan. "Ultrabroadband Photonic Structures To Achieve High-Performance Daytime Radiative Cooling". In: *Nano Letters* 13.4 (Nov. 2013), pp. 1457–1461. DOI: 10.1021/nl4004283.

[29] Mehdi N. Bahadori. "Passive Cooling Systems in Iranian Architecture". In: *Scientific American* 238.2 (1978), pp. 144–154. DOI: 10.1038/scientificamerican0278-144.

[30] M. Mahdavinejad and Kavan Javanrudi. "Assessment of Ancient Fridges: A Sustainable Method to Storage Ice in Hot-Arid Climates". In: *Asian Culture and History* 4.2 (Jan. 2012). DOI: 10.5539/ach.v4n2p133.

[31] T. S. Eriksson and C. G. Granqvist. "Radiative cooling computed for model atmospheres". In: *Applied Optics* 21.23 (Jan. 1982), p. 4381. DOI: 10.1364/ao.21.004381.

[32] Mehdi Zeyghami, D. Yogi Goswami, and Elias Stefanakos. "A review of clear sky radiative cooling developments and applications in renewable power systems and passive building cooling". In: *Solar Energy Materials and Solar Cells* 178 (2018), pp. 115–128. DOI: 10.1016/j.solmat.2018.01.015.

[33] Xingshu Sun, Yubo Sun, Zhiguang Zhou, Muhammad Ashraful Alam, and Peter Bermel. "Radiative sky cooling: fundamental physics, materials, structures, and applications". In: *Nanophotonics* 6.5 (2017), pp. 997–1015. DOI: 10.1515/nanoph-2017-0020.

[34] S. Catalanotti, V. Cuomo, G. Piro, D. Ruggi, V. Silvestrini, and G. Troise. "The radiative cooling of selective surfaces". In: *Solar Energy* 17.2 (May 1975), pp. 83–89. ISSN: 0038092X. DOI: 10.1016/0038-092X(75)90062-6.

[35] B. Bartoli, S. Catalanotti, B. Coluzzi, V. Cuomo, V. Silvestrini, and G. Troise. "Nocturnal and diurnal performances of selective radiators". In: *Applied Energy* 3.4 (1977), pp. 267–286. DOI: 10.1016/0306-2619(77)90015-0.

[36] C.g. Granqvist, A. Hjortsberg, and T.s. Eriksson. "Radiative cooling to low temperatures with selectivity IR-emitting surfaces". In: *Thin Solid Films* 90.2 (1982), pp. 187–190. DOI: 10.1016/0040-6090(82)90648-4.

[37] C. G. Granqvist and A. Hjortsberg. "Surfaces for radiative cooling: Silicon monoxide films on aluminum". In: *Applied Physics Letters* 36.2 (1980), pp. 139–141. DOI: 10.1063/1.91406.

[38] T.s. Eriksson, S.-J. Jiang, and C.g. Granqvist. "Surface coatings for radiative cooling applications: Silicon dioxide and silicon nitride made by reactive rf-sputtering". In: *Solar Energy Materials* 12.5 (1985), pp. 319–325. DOI: 10.1016/0165-1633(85)90001-2.

[39] Deda M. Diatezua, Paul A. Thiry, Alain Dereux, and Roland Caudano. "Silicon oxynitride multilayers as spectrally selective material for passive radiative cooling applications". In: *Solar Energy Materials and Solar Cells* 40.3 (1996), pp. 253–259. DOI: 10.1016/0927-0248(95)00092-5.

[40] A. Hjortsberg and C. G. Granqvist. "Radiative cooling with selectively emitting ethylene gas". In: *Applied Physics Letters* 39.6 (Sept. 1981), pp. 507–509. ISSN: 0003-6951, 1077-3118. DOI: 10.1063/1.92783.

[41] E.m. Lushiku, T.s. Eriksson, A. Hjortsberg, and C.g. Granqvist. "Radiative cooling to low temperatures with selectively infrared-emitting gases". In: *Solar Wind Technology* 1.2 (1984), pp. 115–121. DOI: 10.1016/0741-983x(84)90013-4.

[42] T.s. Eriksson, E.m. Lushiku, and C.g. Granqvist. "Materials for radiative cooling to low temperature". In: *Solar Energy Materials* 11.3 (1984), pp. 149–161. DOI: 10.1016/0165-1633(84)90067-4.

[43] B.a. Kimball. "Cooling performance and efficiency of night sky radiators". In: *Solar Energy* 34.1 (1985), pp. 19–33. DOI: 10.1016/0038-092x(85)90089-1.

[44] B. Orel, M.klanjšek Gunde, and A. Krainer. "Radiative cooling efficiency of white pigmented paints". In: *Solar Energy* 50.6 (1993), pp. 477–482. DOI: 10.1016/0038-092x(93)90108-z.

[45] Torbjörn M.j. Nilsson, Gunnar A. Niklasson, and Claes G. Granqvist. "A solar reflecting material for radiative cooling applications: ZnS pigmented polyethylene". In: *Solar Energy Materials and Solar Cells* 28.2 (1992), pp. 175–193. DOI: 10.1016/0927-0248(92)90010-m.

[46] Torbjörn M.j. Nilsson and Gunnar A. Niklasson. "Radiative cooling during the day: simulations and experiments on pigmented polyethylene cover foils". In: *Solar Energy Materials and Solar Cells* 37.1 (1995), pp. 93–118. DOI: 10.1016/0927-0248(94)00200-2.

[47] Y. X. Yeng, M. Ghebrebrhan, P. Bermel, W. R. Chan, J. D. Joannopoulos, M. Soljacic, and I. Celanovic. "Enabling high-temperature nanophotonics for energy applications". In: *Proceedings of the National Academy of Sciences* 109.7 (2012), pp. 2280–2285. DOI: 10.1073/pnas.1120149109.

[48] Aaswath P. Raman, Marc Abou Anoma, Linxiao Zhu, Eden Rephaeli, and Shanhui Fan. "Passive radiative cooling below ambient air temperature under direct sunlight". In: *Nature* 515.7528 (2014), pp. 540–544. DOI: 10.1038/nature13883.

[49] Linxiao Zhu, Aaswath Raman, Ken Xingze Wang, Marc Abou Anoma, and Shanhui Fan. "Radiative cooling of solar cells". In: *Optica* 1.1 (2014), p. 32. DOI: 10.1364/optica.1.000032.

[50] Linxiao Zhu, Aaswath P. Raman, and Shanhui Fan. "Radiative cooling of solar absorbers using a transparent photonic crystal thermal blackbody". In: *Conference on Lasers and Electro-Optics* (2016). DOI: 10.1364/cleo_qels.2016.fth3b.5.

[51] Chengjun Zou, Guanghui Ren, Md Muntasir Hossain, Shruti Nirantar, Withawat Withayachumnankul, Taimur Ahmed, Madhu Bhaskaran, Sharath Sriram, Min Gu, and Christophe Fumeaux. "Metal-Loaded Dielectric Resonator Metasurfaces for Radiative Cooling". In: *Advanced Optical Materials* 5.20 (Nov. 2017), p. 1700460. DOI: 10.1002/adom.201700460.

[52] Yao Zhai, Yaoguang Ma, Sabrina N. David, Dongliang Zhao, Runnan Lou, Gang Tan, Ronggui Yang, and Xiaobo Yin. "Scalable-manufactured randomized glass-polymer hybrid metamaterial for daytime radiative cooling". In: *Science* 355.6329 (Sept. 2017), pp. 1062–1066. DOI: 10.1126/science.aai7899.

[53] Jun-Long Kou, Zoila Jurado, Zhen Chen, Shanhui Fan, and Austin J. Minnich. "Daytime Radiative Cooling Using Near-Black Infrared Emitters". In: *ACS Photonics* 4.3 (2017), pp. 626–630. DOI: 10.1021/acsphotonics.6b00991.

[54] A. R. Gentle and G. B. Smith. "Radiative Heat Pumping from the Earth Using Surface Phonon Resonant Nanoparticles". In: *Nano Letters* 10.2 (Oct. 2010), pp. 373–379. DOI: 10.1021/nl903271d.

[55] Zhifeng Huang and Xiulin Ruan. "Nanoparticle embedded double-layer coating for daytime radiative cooling". In: *International Journal of Heat and Mass Transfer* 104 (2017), pp. 890–896. DOI: 10.1016/j.ijheatmasstransfer.2016.08.009.

[56] Hua Bao, Chen Yan, Boxiang Wang, Xing Fang, C.y. Zhao, and Xiulin Ruan. "Double-layer nanoparticle-based coatings for efficient terrestrial radiative cooling". In: *Solar Energy Materials and Solar Cells* 168 (2017), pp. 78–84. DOI: 10.1016/j.solmat.2017.04.020.

[57] Wei Li, Yu Shi, Kaifeng Chen, Linxiao Zhu, and Shanhui Fan. "A Comprehensive Photonic Approach for Solar Cell Cooling". In: *ACS Photonics* 4.4 (2017), pp. 774–782. DOI: 10.1021/acsphotonics.7b00089.

[58] Zhiguang Zhou, Yubo Sun, Xingshu Sun, Muhammad Ashraful Alam, Peter Bermel, and Xin Jin. "Radiative cooling for concentrating photovoltaic systems". In: *Thermal Radiation Management for Energy Applications* (June 2017). DOI: 10.1117/12.2273916.

[59] Zhiguang Zhou, Ze Wang, and Peter Bermel. "Radiative cooling for low-bandgap photovoltaics under concentrated sunlight". In: *Optics Express* 27.8 (2019). DOI: 10.1364/oe.27.00a404.

[60] Ababacar Ndiaye, Abdérafi Charki, Abdessamad Kobi, Cheikh M.f. Kébé, Pape A. Ndiaye, and Vincent Sambou. "Degradations of silicon photovoltaic modules: A literature review". In: *Solar Energy* 96 (2013), pp. 140–151. DOI: 10.1016/j.solener.2013.07.005.

[61] Wei Luo et al. "Potential-induced degradation in photovoltaic modules: a critical review". In: *Energy Environmental Science* 10.1 (2017), pp. 43–68. DOI: 10.1039/c6ee02271e.

[62] N. C. Park, W. W. Oh, and D. H. Kim. "Effect of Temperature and Humidity on the Degradation Rate of Multicrystalline Silicon Photovoltaic Module". In: *International Journal of Photoenergy* 2013 (2013), pp. 1–9. DOI: 10.1155/2013/925280.

[63] Stephan Hoffmann and Michael Koehl. "Effect of humidity and temperature on the potential-induced degradation". In: *Progress in Photovoltaics: Research and Applications* 22.2 (2012), pp. 173–179. DOI: 10.1002/pip.2238.

[64] Peter Hacke, Sergiu Spataru, Kent Terwilliger, Greg Perrin, Stephen Glick, Sarah Kurtz, and John Wohlgemuth. "Accelerated testing and modeling of potential-induced degradation as a function of temperature and relative humid-

ity". In: *2015 IEEE 42nd Photovoltaic Specialist Conference (PVSC)* (2015). DOI: 10.1109/pvsc.2015.7355627.

[65] *Introduction to COMSOL Multiphysics: version 4.2*. COMSOL BV, 2011.

[66] *Catalog Item*. URL: https://www.goodfellowusa.com/catalog/GFCat4J.php?ewd_token=Biv7CGGoUu5dx5cmLhBXfafuJMfGGk&n=iAJ351OTlqOfTIHPvMp1EQKZ2ps0K9.

[67] Bruno Lourdes. *ANALYSIS OF POLYSTYRENE RECYCLING PROCESS THROUGH D-LIMONENE*. URL: https://www.academia.edu/36400126/AN%C3%81LISE_AMBIENTAL_DO_PROCESSO_DE_RECICLAGEM_DE_POLIESTIRENO_ATRAV%C3%89S_DO_D-LIMONENO_ENVIRONMENTAL_ANALYSIS_OF_POLYSTYRENE_RECYCLING_PROCESS_THROUGH_D-LIMONENE.

[68] *Extruded Polystyrene Foam Datasheet*. URL: https://www.diversifoam.com/pdf.

[69] *Carr Polystyrene Foam Data Sheet*. URL: https://www.mcmaster.com/9255k2.

[70] *Abrisa Technologies Soda-lime Datasheet*. URL: https://abrisatechnologies.com/specs/.

[71] *Silver Adhesive Data Sheet*. URL: https://www.aremco.com/conductive-compounds/.

[72] *Carr PMMA Data sheet*. URL: https://www.mcmaster.com/8581k35.

[73] *Online Materials Information Resource*. URL: http://www.matweb.com/index.aspx.

[74] P.t. Tsilingiris. "Thermophysical and transport properties of humid air at temperature range between 0 and 100C". In: *Energy Conversion and Management* 49.5 (2008), pp. 1098–1110. DOI: 10.1016/j.enconman.2007.09.015.

[75] *MatWeb Al 5052 datasheet*. URL: http://www.matweb.com/search/DataSheet.aspx?MatGUID=96d768abc51e4157a1b8f95856c49028.

[76] *MatWeb GaSb datasheet*. URL: http://www.matweb.com/search/DataSheet.aspx?MatGUID=0d3a6a7d04b54354a84fed633bf26d64.

[77] *MatWeb PMMA datasheet*. URL: http://www.matweb.com/search/DataSheet.aspx?MatGUID=632572aeef2a4224b5ac8fbd4f1b6f77.

[78] *MatWeb silver paste datasheet*. URL: http://www.matweb.com/search/DataSheet.aspx?MatGUID=63cbd043a31f4f739ddb7632c1443d33.

[79] *West Lafayette, IN History*. URL: https://www.wunderground.com/history/daily/us/in/west-lafayette/KLAF/date/2019-8-28.

[80] Aniceto Zaragoza and Csar Bartolom. "Albedo Effect and Energy Efficiency of Cities". In: *Sustainable Development - Energy, Engineering and Technologies - Manufacturing and Environment* (2012). DOI: 10.5772/29536.

[81] *The National Concrete Overlay Explorer*. URL: http://overlays.acpa.org/Downloads/RT/RT3.05.pdf.

[82] Theodore L. Bergman, Adrienne S. Lavine, Frank P. Incropera, and David P. DeWitt. *Fundamentals of heat and mass transfer*. John Wiley Sons, Inc., 2011.

[83] *MODETRAN*. URL: http://climatemodels.uchicago.edu/modtran/.

[84] *PM100D Compact Power and Energy Meter Console, Digital 4" LCD*. URL: https://www.thorlabs.com/thorproduct.cfm?partnumber=PM100D.

[85] *DI-245 4-channel USB Voltage and Thermocouple Data Acquisition*. URL: https://www.dataq.com/products/di-245/.

[86] Thermometrics. *Type K Thermocouple*. URL: https://www.thermometricscorp.com/thertypk.html.

[87] *S314C Thermal Power Sensor Head, Surface Absorber, 0.25 - 11 m, 40 W, Ø25 mm*. URL: https://www.thorlabs.com/thorproduct.cfm?partnumber=S314C.

VITA

Ze Wang

2028 Delray Drive, West Lafayette, IN
(M) +1 765 775 9313 (E) wang3617@purdue.edu

Educational Background

Zhejiang University 09/2011-12/2015

- BEng Information Engineering

Purdue University 09/2017-present

- MS Electrical and Computer Engineering

Research Experience

Purdue University

Selective Emitter Design and Fabrication for Solar Cell 01/2018-present

- Conducted research on solar cell efficiency, thin film technology, rare-earth selective emitter
- Developed algorithms and built a software for solving multi-layer thin film optical prosperities
- Building a Sm^{3+} doped YAG selective emitter with e-beam coated Rh back surface reflector
- Over 200 hours cleanroom experience

Radiative cooling for low-bandgap photovoltaics under concentrated sunlight 05/2019-present

- Designed and built CPV radiative cooling demonstration setups
- Out-door experiments and simulations are conducted to study the performance of radiative cooling, achieved a temperature drop of 36 °C and open-circuit voltage increase of 0. 08 V for GaSb solar cell
- Published a paper and peer-reviewed multiple manuscripts published on high-impactor journals

Zhejiang University

Digital Focimeter Design 12/2014-06/2015

- Created a digital auto focimeter and with range from 10mm to 500mm and inaccuracy of 2%
- Capable of accurate automatic focus, edge detect, line detect and image optimize

System Design Based on 8051 Microcontroller 03/2014-06/2014

- Created an Electronic keyboard by using 8051 microcontroller to control RAM, LCD screen, speaker and keyboard
- Capable of playing, forward, rewind, pause, stop and recording tunes, show menu and lyrics on LCD screen

Work Experience

Institute of Remote Sensing & Digital Earth, Chinese Academy of Science

Digital Simulation & Analysis Software for Optical Remote Sensing System 12/2015- 05/2017

- Led a 5-member team to develop algorithms for a remote sensing satellite simulation software, designed the modulation transfer function of optical system and CCD sensor of a satellite based on wave optics and semiconductor physics

Skills

Computer: C, Matlab；COMSOL; SolidWorks; Photoshop, Lightroom, Illustrator; Optsystem, Altium Designer;

Language: Mandarin (first language), English (fluent)